Challenge Journal of STRUCTURAL MECHANICS

Vol.6 No.4 (2020)

Mindlin's theory buckling building codes compressive strength dynamic analysis dynamic response earthquake finite element analysis finite element method mechanical properties nonlinear analysis optimization prefabrication pushover analysis reinforced concrete seismic analysis seismic design seismic isolation shallow foundations steel silo temperature effects thick plate wind

ISSN 2149-8024

TULPAR ACADEMIC PUBLISHING

Challenge Journal of Structural Mechanics

E-mail: *cjsmec@challengejournal.com*

Web page: *cjsmec.challengejournal.com*

TULPAR Academic Publishing
www.tulparpublishing.com

Challenge Journal of Structural Mechanics

CONTENTS

TULPAR ACADEMIC PUBLISHING

Challenge Journal of Structural Mechanics

Research Article

Structural behavior of shear connectors embedded in different types of concrete

Adil Hadi Wardi [a], Gokhan Tunc [b,*], Khalil Ibraheem [c]

[a] *Ministry of Construction, Housing, Municipalities and Public Works, Anbar, Iraq*
[b] *Department of Civil Engineering, Atılım University, 06830 Ankara, Turkey*
[c] *Department of Civil Engineering, University of Anbar, Ramadi, Iraq*

ABSTRACT

Push-out tests are used to determine shear connectors' properties where two small reinforced concrete walls are attached to the top and bottom flanges of an I-section through four shear studs located on both its flanges. In this study, the structural behavior of shear connectors was examined by testing a total of 36 push-out specimens. In these specimens, various test parameters were used. The types of shear connectors and their strengths, their connection types, and the strength of the concrete in which they were embedded were all investigated. Headed, L-shaped, and C-shaped studs were selected in this experimental study to represent different types of shear connectors. These shear connectors were assumed to be either ordinary or high strength steel-embedded in three different types of concrete: ordinary, high strength, and reactive powder concretes. In these tests, the shear connectors were connected through welding or epoxy bonding. The objective of this study was to investigate the structural behaviors of these different types of shear connectors by focusing on their shear force capacities and slip values. The test results indicate that the reactive powder concrete increased the mechanical properties of concrete as the concrete age increased. The specimens with C-shaped studs made of high-strength steel with welded studs embedded in normal weight, high strength and reactive powder concretes, generated the maximum shear resistance values.

ARTICLE INFO

Article history:
Received 11 March 2020
Revised 13 May 2020
Accepted 17 June 2020

Keywords:
Push-out test
Shear connectors
Reactive powder concrete
High strength concrete

1. Introduction

In recent years, composite materials have been frequently used in structures instead of traditional raw materials to attain better mechanical properties that resist various types of loadings subjected to short and long time periods. The goal of using composite material is to increase the overall strength of structural members, thereby achieving more economical cross sections. Therefore, it is important to understand the structural behavior of composite materials and their behaviors. One such material could be a shear connector that works as an interface between a steel and a reinforced concrete member to transfer shear loads resulting from either wind or earthquakes.

Shear connectors were selected as the main focus of this study. The main objective of our research was to investigate the structural behavior of different types of shear connectors embedded in different types of concrete. For this purpose, high strength concrete (HSC), reactive powder concrete (RPC), and no-fine aggregate concrete (NFC) were selected, along with normal weight concrete (NWC), which was used as a reference. Headed studs, L-shaped and channel type shear connectors, assumed to be either welded or epoxy bonded, were also included as an additional parameter in the testing stage.

A total of 36 push-out test specimens were prepared as part of an MS thesis conducted jointly at Atilim University, Ankara, Turkey and the University of Anbar, Ramadi, Iraq, since they have been frequently used in

* *Corresponding author*. Tel.: +90-312-586-8355 ; Fax: +90-312-586-8091 ; E-mail address: gokhan.tunc@atilim.edu.tr (G. Tunc)
ISSN: 2149-8024 / DOI: https://doi.org/10.20528/cjsmec.2020.04.001

these types of experiments to assess the interfacial shear strength developed at a composite interface (Wardi, 2019). This interfacial behavior is generally recognized by a load-slip curve that is obtained from experimental push-out tests, even though the tests are generally expensive and time consuming. In this experimental study, the mechanical properties of different types of concrete were also investigated, including their compressive strengths, splitting tensile strengths, modulus of ruptures, moduli of elasticities, and densities.

2. Literature Review

In this section, brief information will be provided regarding the shear studs in various types of concrete.

2.1. Composite behavior of shear studs

Many theories take equilibrium and compatibility equations into account to derive relationships for the composite action of a beam. The earliest theory for composite beams is adopted in 1951 that was based on elastic analysis and linear materials for concrete, steel, and shear stud connectors (Newmark et al., 1951). According to the study, the axial force that was developed between the interface of a steel beam and a composite slab was obtained. In 1968, Adekola derived equations using a finite difference approach that represented the uplift forces and axial forces on a composite beam of steel and concrete (Adekola, 1968).

In the past 20 years, there have been other studies conducted in this area. In 2005, a new model was proposed to explain the performance of multilayer composite slab using partial interaction theory subjected to static loading (Aziz, 2005). Differential equations were derived by applying equilibrium and compatibility equations. Linear and nonlinear analyses of concrete, steel plates, and shear stud connectors were used in simulations taking slip and uplift into account. The unknown variables such as slip, deflection, stresses, and strains were solved at each incremental loading. The push-out test specimens were tested to determine the load-slip relationship, maximum load capacity, and maximum slip value. Validation and verifications to evaluate the actual behavior of a multilayered composite slab were checked with respect to the experimental results.

In 2017, a comprehensive literature review study was conducted to evaluate the shear strength of headed studs in a slab with a steel deck cut on the flange and headed studs in a solid slab (Hirama et al., 2017). For this purpose, headed stud diameter, slab type, and failure modes were investigated specifically for studs with diameters of more than 25 mm. Based on the study, it was found that the shear strength of headed studs with a diameter of more than 25 mm in solid slab decreased gradually with the increasing diameter in both failure modes (headed stud and concrete failures).

The influence of specimen configuration, zirconia surface treatment, and bonding area were evaluated on the push-out bond strength to Y-TZP (yttrium-stabilized tetragonal zirconia poly-crystal) ceramics using a finite element analysis (FEA) method (Wandscher et al., 2018). Based on the study, it was found that the adhesion increased significantly by surface treatment, except for 'resin cement macro-test'. The FEA method proved that the stresses were more homogeneously distributed at the interface of micro-specimens.

In 2018, the push-out tests of large perfobond connectors, which are commonly used in composite and hybrid bridges, were conducted (Di et al., 2018). For this purpose, 13 groups of 39 push-out specimens were tested to verify the mechanical properties of large connectors. The large sized connectors with their better capacity served as an excellent alternative to the connectors with smaller sizes. The study indicated that the large sized connectors helped to reduce the number of connections, and thus helped the flow of coarse aggregate concrete. The results also showed that the bearing capacity would be improved by increasing the geometrical size of the hole under a high level of concrete dowel confinement. Finally, an empirical formulation to predict the shear capacity was proposed taking multiple influencing factors into account.

2.2. High strength concrete (HSC)

The term "high strength" depends on many parameters, such as the availability of good quality local materials and construction practices. Some of the research conducted in this area is as follows:

In 2017, a total of 280 concrete specimens in 28 different test groups was produced. In this study, the properties of HSC containing silica fume and nano-silica that were both affected by different amounts of polypropylene (PP) and macro-polymeric (MP) fibers were investigated (Fallah and Nematzadeh, 2017). Based on the test results, it was observed that the mechanical properties of high-strength concrete improved by incorporating macro-polymeric fibers into the concrete mixture. The physico-mechanical properties of the HSC were adversely affected when high volume fractions of polypropylene fibers in the concrete mixture was used.

In 2017, a total of twenty-four push-out specimens were investigated to examine the structural behavior of perfobond strip connectors (PBL) for steel-concrete joint of hybrid girders with ultra-high performance concrete (He et al., 2017). In this study, an analytical model for PBL and ultra-high performance concrete was developed, and appropriate parameters from test data were obtained. These parameters were used in the hybrid girders' steel-concrete joints to predict the ultimate resistant-capacity of PBL.

The effectiveness of steel fiber inclusion on the structural performance of HSC columns was examined by conducting a test on a total of 7 specimens with and without steel fiber (Bae et al., 2018). In this study, all test specimens were subjected to axial and reversed cyclic lateral loads. The test results indicated that the steel fiber inclusion not only significantly increased the structural performance of columns, but also increased the shear strength and energy dissipation capacity of the

columns. Based on the test results, a new equation was proposed to estimate the strength of steel fiber reinforced high strength concrete columns.

2.3. Reactive powder concrete (RPC)

Reactive Powder Concrete (RPC) is a developing composite material that produces high strength (both compressive and flexural) and lower permeability compared to High Performance Concrete (HPC). In this section, the most recent literature review on RPC is presented, including laboratory investigations of both RPC and HPC.

In 2013, the behavior of T and rectangular sectioned beams under shear were investigated (Al-Shafi'i, 2013). The beams were subjected to four point loads. The tests focused on recording cracked load, ultimate shear, mid-deflection and crack width. The researcher concluded that increasing the percentage of steel fiber to 2%, increased the cracked load by 60% compared to that of the T section constructed from normal concrete.

Experimental and theoretical works of T-sectioned beam under flexural loading were also investigated (Ismael, 2013). For this purpose, a total of fifteen beams were tested using parameters like steel fiber, silica fume, tensile strength, and geometric cross-section. Crack loads, strength capacity, maximum deflection, and failure modes were the main parameters studied by the author. By using block stress distribution, the author derived an equation to determine the bending moment capacity. The tests result indicated that increasing the RP increased the capacity of the loading.

In another study, I-sectioned beams were examined using both experimental and theoretical works (Hmeed, 2014). The main parameters of the testing were the concrete type and longitudinal steel ratio. The author noted that the behavior of beams under flexure was depended on the type of concrete used in their flanges. The change in concrete type at the top and bottom flanges made changes in the deflection and crack loading by around hundred percent. The test results focused on crack load, load capacity, mid-deflection, and failure modes. According to the tests, the results indicated an increase in the ratio of RPC caused a rise in the load capacity but a decrease in the deflections.

3. Mechanical Properties of Different Types of Concrete

The properties of different types of concrete used in this study are described in detail in the following sections. The details of each concrete testing has not been included since the focus of this article was on the structural behavior of shear studs. However, the results of the concrete tests have been included for the benefit of other researchers conducting studies in this area (for more information please refer to Wardi (2019)).

3.1. Compressive strength

The compressive strengths of different types of concrete are given in Fig. 1 and Table 1. A total of 60 cube specimens with dimensions of 150 mm by 150 mm by 150 mm were tested.

Based on the test results, the concrete compressive strengths at 28 days were 27 MPa for the normal or ordinary weight concrete (NWC or OWC), 85 MPa for the HSC, 120 MPa for the RPC, and 20 MPa for the no fine concrete (NFC).

3.2. Splitting tensile strength

The splitting tensile strength values of different types of concrete are given in Fig. 2 and Table 2. A total of 40 specimens with dimensions of 400 mm by 100 mm by 100 mm were tested.

Based on the values given in Fig. 2 and Table 2, as expected the maximum value of the splitting tensile strength at 28 days was 14 MPa and obtained for the RPC while the minimum one was 2.0 MPa for the NFC. The same value for the reference concrete, NWC (OWC), was 3.1 MPa.

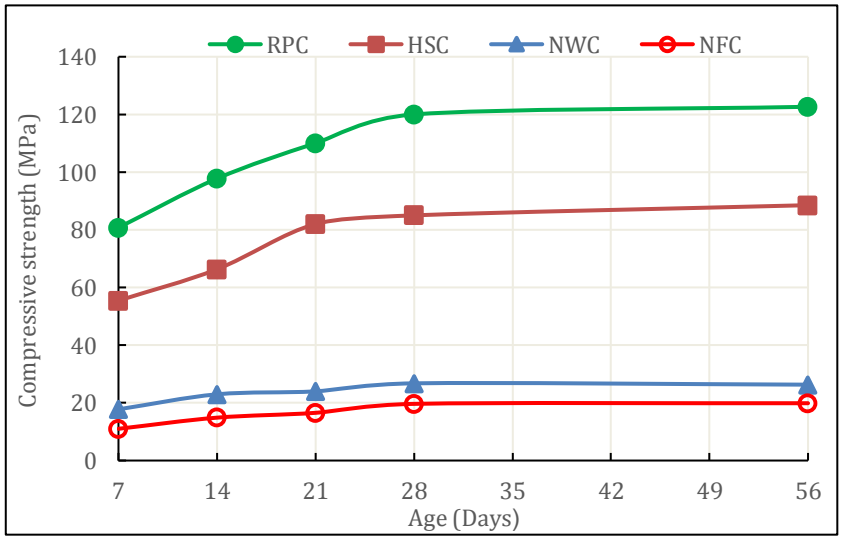

Fig. 1. Compressive strength of different types of concrete.

Table 1. Compressive strength as a function of time.

Type of concrete	Age (days)	Compressive strength (MPa)	Change in compressive strength with respect to reference mix (%)
M1 (NWC or OWC) Reference	7	17.8	0
	14	23.0	0
	21	24.0	0
	28	26.8	0
	56	26.3	0
M2 (HSC)	7	55.4	212
	14	66.3	189
	21	82.0	242
	28	85.0	218
	56	88.5	237
M3 (RPC)	7	80.8	355
	14	97.8	326
	21	110.0	359
	28	120.0	348
	56	122.7	366
M4 (NFC)	7	11.0	-38
	14	14.9	-35
	21	16.5	-31
	28	19.7	-27
	56	19.9	-25

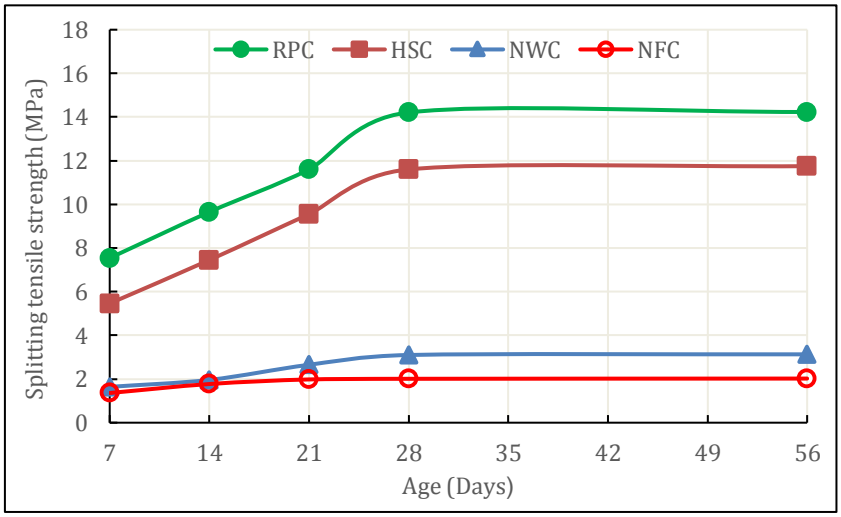

Fig. 2. Splitting tensile strength of different types of concrete.

Table 2. Splitting tensile strength as a function of time.

Type of concrete	Age (days)	Splitting tensile strength (MPa)	Change in splitting tensile strength with respect to reference mix (%)
M1 (NWC or OWC) Reference	7	1.6	0
	14	2.0	0
	21	2.7	0
	28	3.1	0
	56	3.3	0
M2 (HSC)	7	5.5	233
	14	7.5	280
	21	9.6	260
	28	11.6	274
	56	11.8	275
M3 (RPC)	7	7.5	360
	14	9.7	392
	21	11.6	338
	28	14.2	358
	56	14.2	355
M4 (NFC)	7	1.4	-17
	14	1.8	-10
	21	2.0	-25
	28	2.0	-35
	56	2.0	-36

3.3. Modulus of rupture (flexural strength)

The moduli of rupture values of different types of concrete are given in Fig. 3 and Table 3.

Based on the results listed in Table 3 and Fig. 3, the modulus of rupture strength at 28 days was 3.4 MPa for the reference concrete, NWC (OWC), while the same value was 11.9 MPa for the HSC, 16 for the RPC, and 2.6 MPa for the NFC.

3.4. Static modulus of elasticity

The static moduli of elasticities of different types of concrete are given in Fig. 4 and Table 4.

According to the test results, the values of the static modulus of elasticity at 28 days were 24.7 GPa for the NWC (OWC), 33.2 GPa for the HSC, 43.4 GPa for the RPC, and 20.9 GPa for the NFC.

3.5. Push–out tests

Push-out test specimen was produced according to the requirements of Eurocode 4 (EN 1994 - Eurocode 4, 1994). The shear connectors' properties were determined experimentally through simple push-out tests where two small slabs were linked to the flanges of an IPE 100 section by four studs on each side (Fig. 5). The slabs were bedded onto the lower part of a compression-testing machine, and the load was applied gradually to the top end of the steel section. A load-slip curve and then the stiffness of shear connectors were obtained.

The push-out segments were fabricated according to the dimensions of the studs as shown in Fig. 6. Then, they were cast and cured in water for 28 days. A hydraulic testing machine with a capacity of 2,000 kN was used to test the push-out segments at the Construction Laboratory of the Engineering Syndicate of Iraq Branch of Al-Anbar (see Fig. 7).

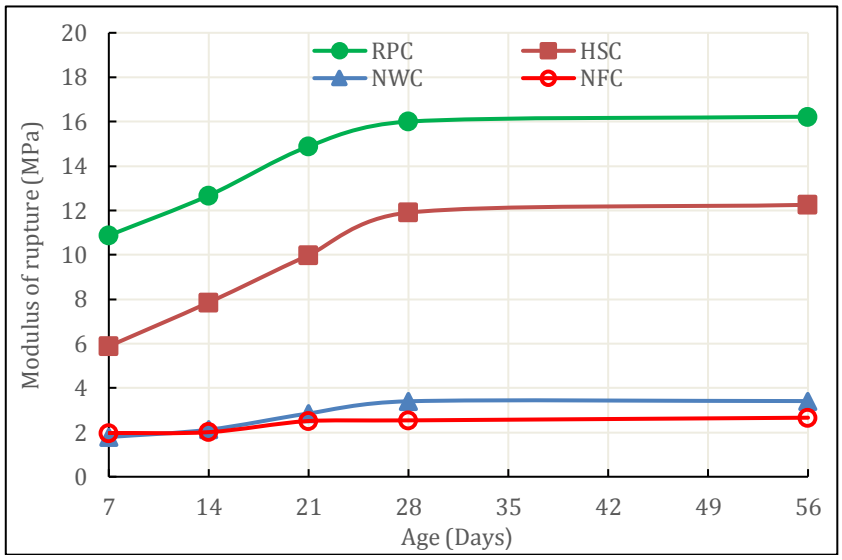

Fig. 3. Modulus of rupture of different types of concrete.

Table 3. Modulus of rupture as a function of time.

Type of concrete	Age (days)	Modulus of rupture (MPa)	Change in modulus of rupture with respect to reference mix (%)
M1 (NWC or OWC) Reference	7	1.8	0
	14	2.1	0
	21	2.9	0
	28	3.4	0
	56	3.4	0
M2 (HSC)	7	5.9	229
	14	7.9	270
	21	10.0	250
	28	11.9	250
	56	12.3	259
M3 (RPC)	7	10.9	507
	14	12.7	498
	21	14.9	422
	28	16.0	371
	56	16.2	376
M4 (NFC)	7	1.9	10
	14	2.0	-5
	21	2.5	-12
	28	2.6	-25
	56	2.7	-22

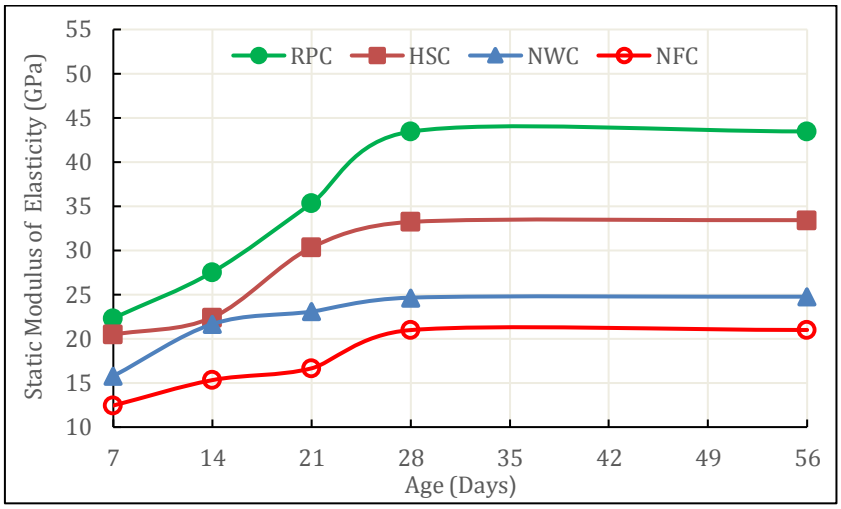

Fig. 4. Static modulus of elasticity of different types of concrete.

Table 4. Static modulus of elasticity for different types of concrete with time.

Type of concrete	Age (days)	Static modulus of elasticity (GPa)	Change in static modulus of elasticity with respect to reference mix (%)
M1 (NWC or OWC) Reference	7	15.8	0
	14	21.7	0
	21	23.1	0
	28	24.7	0
	56	24.8	0
M2 (HSC)	7	20.5	30
	14	22.4	4
	21	30.3	32
	28	33.2	35
	56	33.4	35
M3 (RPC)	7	22.3	42
	14	27.5	27
	21	35.3	53
	28	43.4	76
	56	43.5	76
M4 (NFC)	7	12.4	-21
	14	15.3	-29
	21	16.7	-28
	28	20.9	-15
	56	21.0	-15

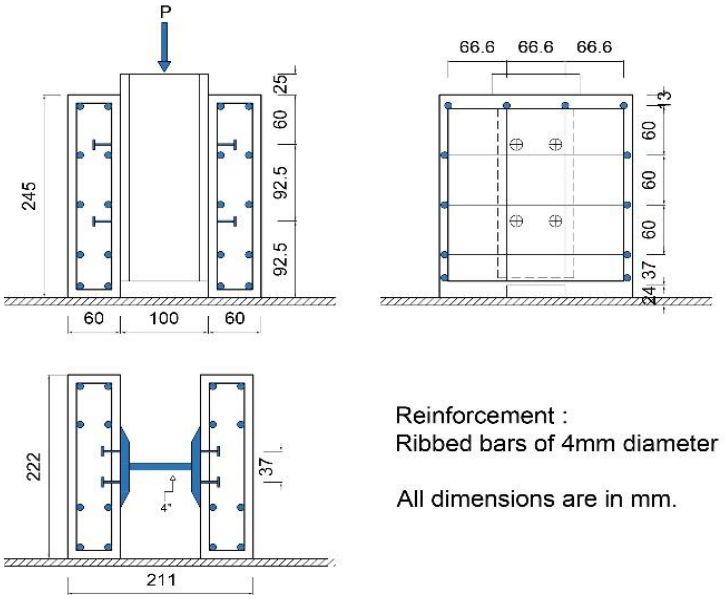

Fig. 5. Shear connectors for push-out tests.

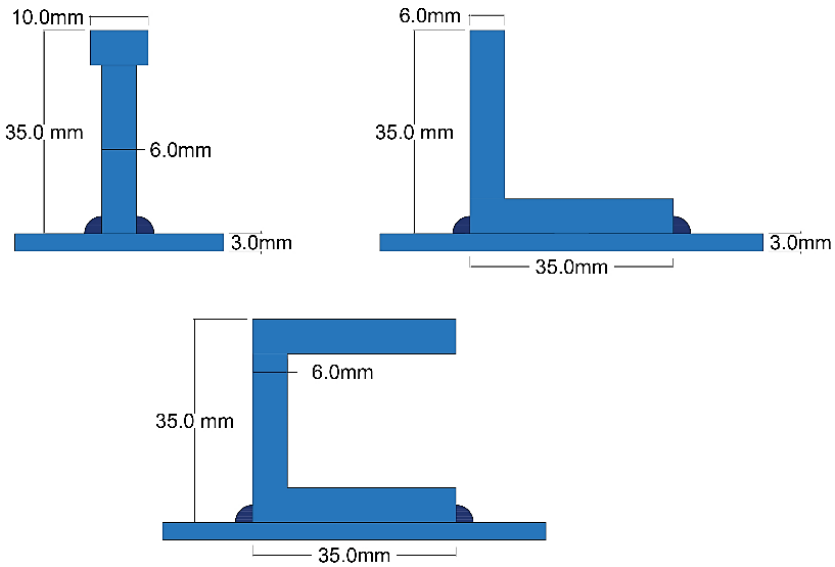

Fig. 6. Dimensions of shear connectors for push-out tests.

Fig. 7. Fabrication, casting, and testing of push-out specimens.

4. Test Results

The test results of push-out specimens are studied in three groups: (a) effect of shear stiffness, (b) effect of concrete type, and (c) effect of bond type. Because of the very poor test results that the no-fine aggregate concrete type (NFC) generated, the NFC is decided not to be further studied. Therefore, the behavior of shear studs will be studied for the following three different concrete types, NWC, HSC, and RPC.

4.1. Effect of shear stiffness

The variation in the shear stiffness of connectors is studied for each concrete type. The details of the test results are provided in the next subsections.

4.1.1. Normal (ordinary) weight concrete

The test results of different types of connectors in normal (ordinary) weight concrete are illustrated in Figs. 8, 9, and 10 based on the values given in Table 5.

In Table 5, a four-digit label is used for different specimens. The first letter in the label represents the type of concrete. The second letter is used to define the type of different shear connectors. The third letter indicates the type of steel for the shear connectors, and the fourth letter is used to describe the type of connectors. For example, a label OHOW is used for the welded headed shear connector made of ordinary steel, which is embedded in an ordinary strength concrete.

According to the test results, the specimen OCHW resisted the largest shear force with a value of 876 kN, with a percentage of difference around 12% when compared to the shear value obtained from the specimen labeled OHHW. The lowest shear value was obtained in the specimen OLOE with a value of 248 kN.

4.1.2. High strength concrete

The test results for high strength concrete and different types of connectors are shown in Table 6 and Figs. 11, 12, and 13. The label notation was very similar to those that were used for the studs in normal weight concrete. The only difference was in the first digit, instead of normal strength concrete (N) a high strength concrete (H) was used.

According to the test results, the specimen HCHW had the largest shear capacity of 966 kN with a difference of approximately 1.3% when compared to the shear value of the specimen HHHW. The minimum shear capacity

was obtained in the specimen, HLOE, with a value of 411 kN. As illustrated in Fig. 13, the shear capacity of HCHE was slightly larger than that of HCOW. When the results of other C-shaped specimens with the same connection details were compared, a somewhat similar trend was also observed. In other words, the shear capacities of epoxy bonded high strength C-shaped steel connectors were almost always very close to those of welded ordinary C-shaped steel connectors. However, in this particular case, as stated before, the shear capacity of HCHE was slightly larger. This increase was primarily attributed to the presence of high strength concrete and its interaction with the increased surface area of bonding around the shear connectors.

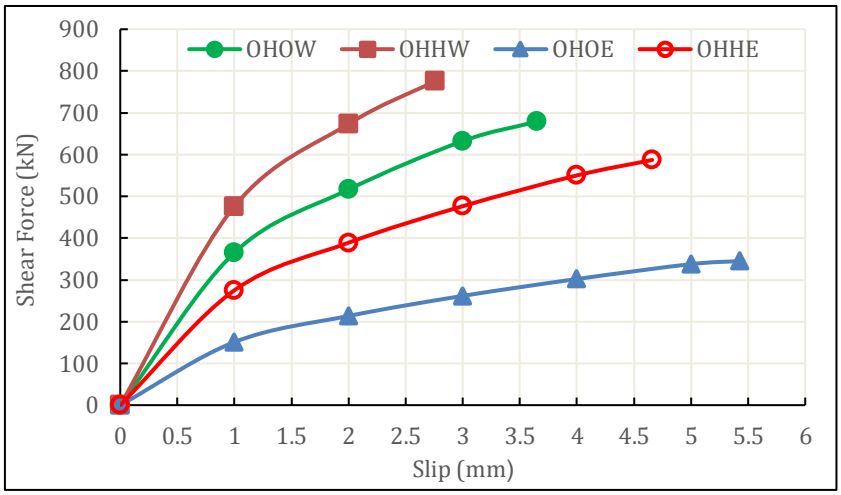

Fig. 8. Headed stud shear connectors with different types of steel properties and bonds in ordinary weight concrete.

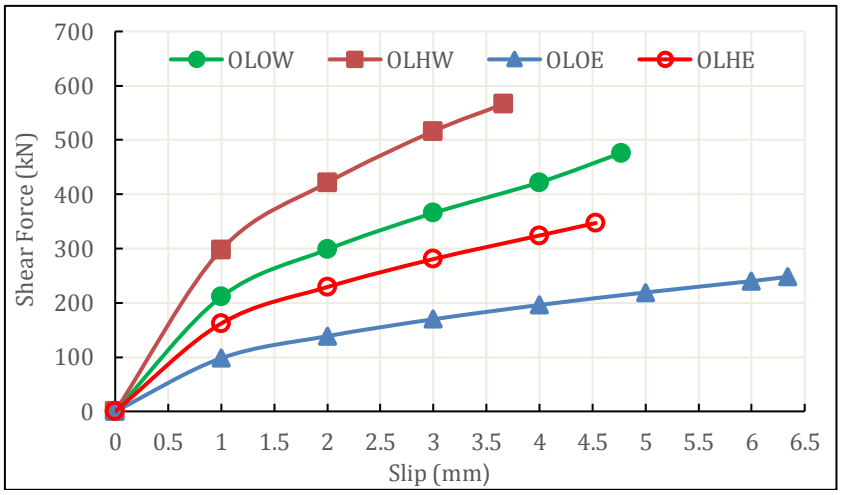

Fig. 9. L- shaped shear connectors with different types of steel properties and bonds in ordinary weight concrete.

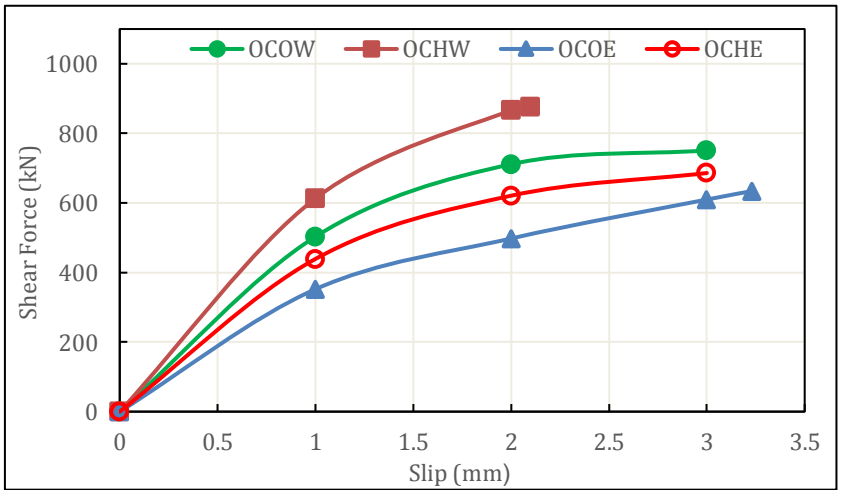

Fig. 10. C- shaped shear connectors with different types of steel properties and bonds in ordinary weight concrete.

Table 5. Test results of push-out test specimens in normal weight concrete.

Label	Type of shear connector	Type of steel strength	Type of bond	Ultimate shear force (kN)	Max. slip (mm)	Shear stiffness (kN/mm)	Difference (%)	Concrete crack width (mm)
OHOW	Headed stud (H)	Ordinary (O)	Welding (W)	679	3.65	93.0	0	0.10
OHHW	Headed stud (H)	High (H)	Welding (W)	776	2.76	140.7	0	0.04
OHOE	Headed stud (H)	Ordinary (O)	Epoxy (E)	345	5.43	31.8	0	0.32
OHHE	Headed stud (H)	High (H)	Epoxy (E)	587	4.66	63.0	0	0.19
OLOW	L- shaped (L)	Ordinary (O)	Welding (W)	476	4.77	49.9	-30	0.11
OLHW	L- shaped (L)	High (H)	Welding (W)	566	3.66	77.3	-27	0.09
OLOE	L- shaped (L)	Ordinary (O)	Epoxy (E)	248	6.34	19.6	-28	0.39
OLHE	L- shaped (L)	High (H)	Epoxy (E)	347	4.53	38.3	-41	0.22
OCOW	Channel (C)	Ordinary (O)	Welding (W)	751	2.99	125.6	11	0.08
OCHW	Channel (C)	High (H)	Welding (W)	876	2.09	209.6	13	0.03
OCOE	Channel (C)	Ordinary (O)	Epoxy (E)	634	3.23	98.1	84	0.11
OCHE	Channel (C)	High (H)	Epoxy (E)	686	3.01	114.0	17	0.09

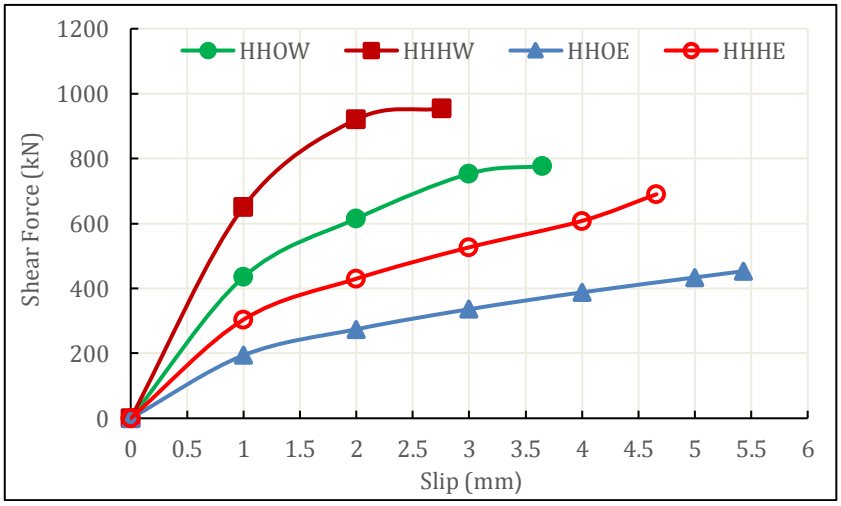

Fig. 11. Headed stud shear connector with different types of steel properties and bonds in high strength concrete.

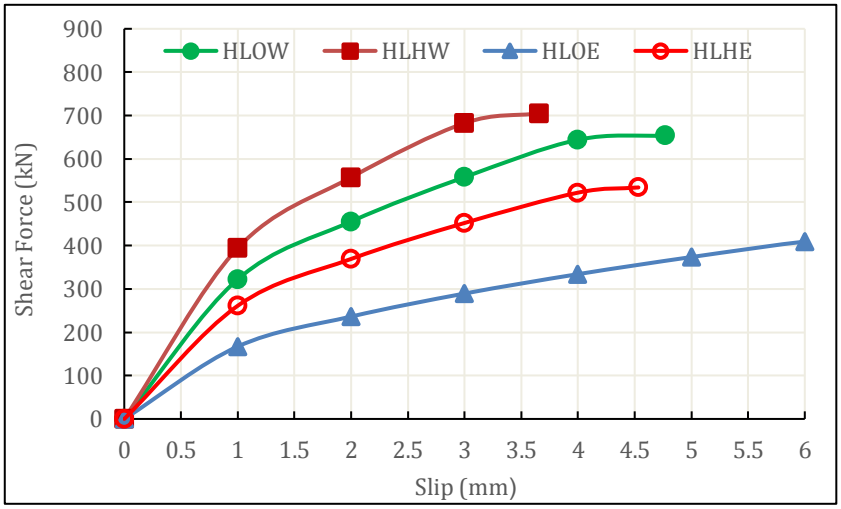

Fig. 12. L- shaped stud shear connector with different types of steel properties and bonds in high strength concrete.

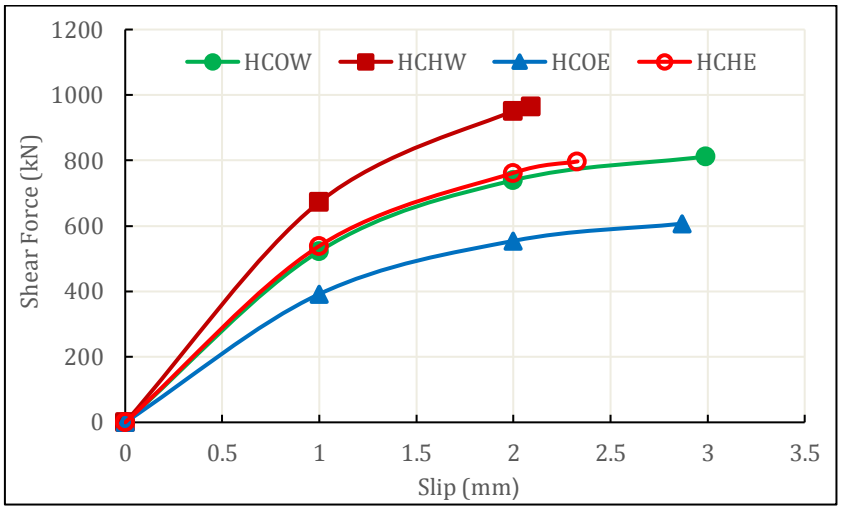

Fig. 13. C- shaped stud shear connector with different types of steel properties and bonds in high strength concrete.

Table 6. Test results of push-out test specimens in high strength concrete.

Label	Type of shear connector	Type of steel strength	Type of bond	Ultimate shear force (kN)	Max. slip (mm)	Shear stiffness (kN/mm)	Difference (%)	Concrete crack width (mm)
HHOW	Headed stud (H)	Ordinary (O)	Welding (W)	777	3.65	106.4	0	0.07
HHHW	Headed stud (H)	High (H)	Welding (W)	954	2.76	172.8	0	0.03
HHOE	Headed stud (H)	Ordinary (O)	Epoxy (E)	453	5.43	41.7	0	0.21
HHHE	Headed stud (H)	High (H)	Epoxy (E)	690	4.66	74.0	0	0.12
HLOW	L- shaped (L)	Ordinary (O)	Welding (W)	654	4.77	68.6	-16	0.09
HLHW	L- shaped (L)	High (H)	Welding (W)	705	3.66	96.3	-26	0.07
HLOE	L- shaped (L)	Ordinary (O)	Epoxy (E)	411	6.34	32.4	-9	0.31
HLHE	L- shaped (L)	High (H)	Epoxy (E)	534	4.33	61.7	-23	0.21
HCOW	Channel (C)	Ordinary (O)	Welding (W)	812	2.99	135.8	5	0.07
HCHW	Channel (C)	High (H)	Welding (W)	966	2.09	231.1	1	0.03
HCOE	Channel (C)	Ordinary (O)	Epoxy (E)	607	2.87	105.7	34	0.09
HCHE	Channel (C)	High (H)	Epoxy (E)	797	2.33	171.0	16	0.08

4.1.3. Reactive powder concrete

The test results of reactive powder concrete are listed in Table 7, and displayed in Figs. 14, 15, and 16. The label notation of the specimens in reactive powder concrete is very similar to those in normal and high strength concretes. The only difference is the first letter, R, which, in this case, represents the reactive powder concrete.

Based on the test results, the specimen RCHW generated the largest shear force value of 1,215 kN, with a difference of 10% compared to the shear value of the specimen RHHW. The minimum shear capacity was obtained in the specimen RLOE with a value of 601 kN.

The test results indicated that the specimens with L-shaped shear connectors were more susceptible to concrete related failures because of a very high stress concentration within a smaller area of concrete, which caused maximum concrete crack width. In these specimens, the failure was caused by the crushing of the concrete contained below the L-shaped connectors. In general, the welding bond was better and gave higher shear force values with less slip values.

4.2. Effect of concrete type

The variation in the shear stiffness of connectors is studied for each concrete type. The details of the test results are provided in the next subsections.

The load-slip curves of different concrete types are plotted in Figs. 17, 18, and 19. In Fig. 17, it appears that the specimen with the headed stud shear connectors which exhibited the least shear force resistance was the OHOE, and the strongest one with the maximum shear force resistance was the RHHW. Based on the

test results, it was observed that the increase in the shear force value of RHHW with the same characteristics of shear connectors and bonds, was around 16% and 42% with respect to the shear force resistance values of HHHW and OHHW, respectively (see Fig. 17).

As illustrated in Fig. 17, among the other headed stud shear connectors, the load-slip curve of the RHHW, which displayed a fracture type of failure, came to an abrupt end at the shear force value of 1,103 kN corresponding to a slip value of 2.06 mm. However, the specimens which displayed concrete failures such as the OHOE specimen exhibited a gradual drop in the load-slip curve extending to a 5.43 mm of slip value at a shear force value of 345 kN.

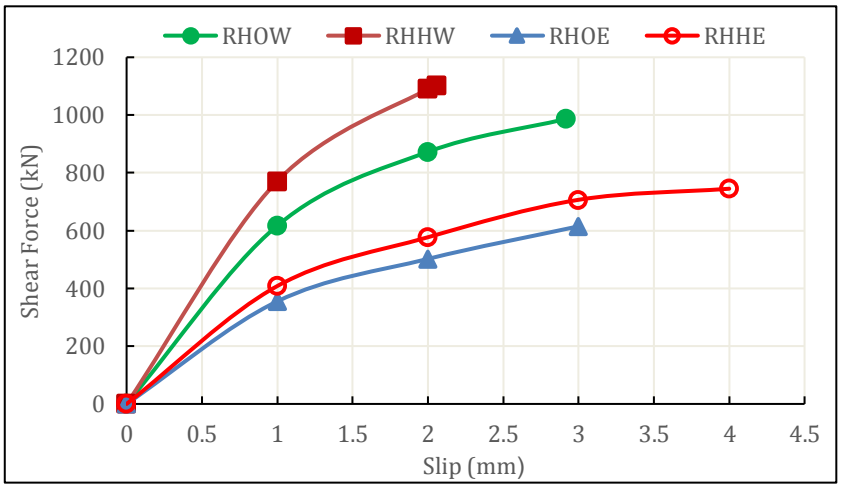

Fig. 14. Headed stud shear connector with different types of steel properties and bonds for reactive powder concrete.

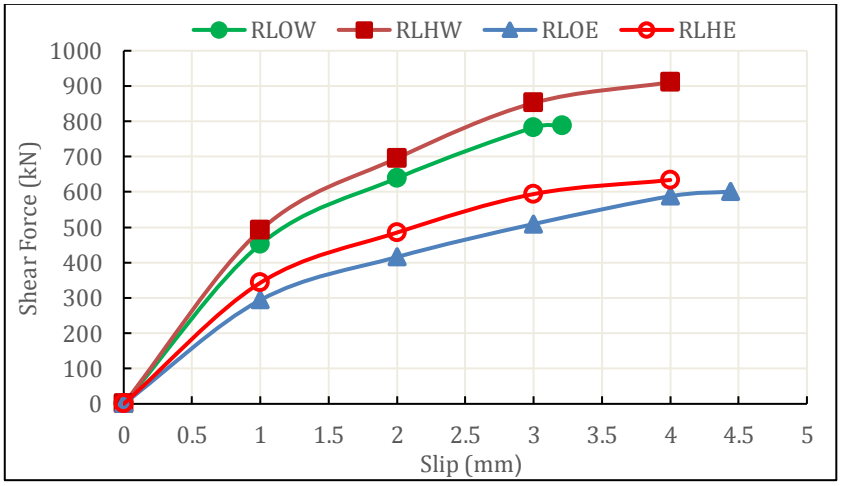

Fig. 15. L- shaped shear connector with different types of steel properties and bonds for reactive powder concrete.

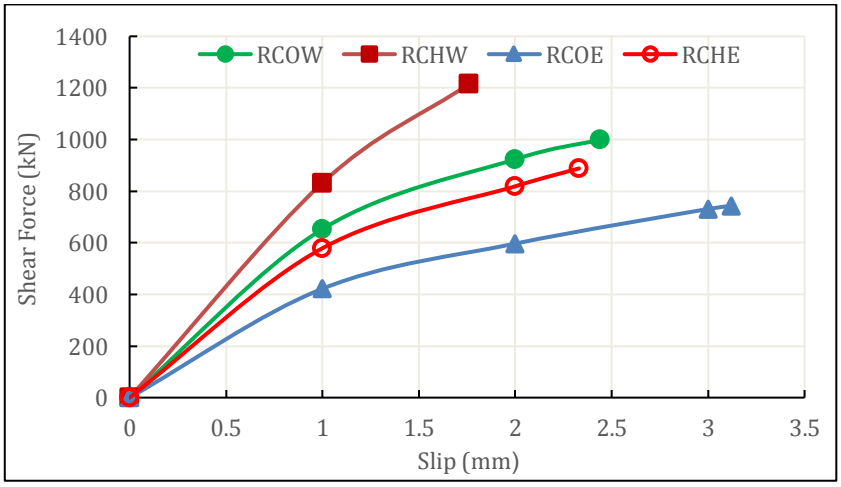

Fig. 16. C- shaped shear connector with different types of steel properties and bonds for reactive powder concrete.

Table 7. Test results for push-out test in reactive powder concrete.

Label	Type of shear connector	Type of steel strength	Type of bond	Ultimate shear force (kN)	Max. slip (mm)	Shear stiffness (kN/mm)	Difference (%)	Concrete crack width (mm)
RHOW	Headed stud (H)	Ordinary (O)	Welding (W)	987	2.92	169.0	0	0.05
RHHW	Headed stud (H)	High (H)	Welding (W)	1103	2.06	267.7	0	0.02
RHOE	Headed stud (H)	Ordinary (O)	Epoxy (E)	665	3.11	106.9	0	0.18
RHHE	Headed stud (H)	High (H)	Epoxy (E)	745	4.00	93.1	0	0.10
RLOW	L- shaped (L)	Ordinary (O)	Welding (W)	788	3.21	122.7	-20	0.08
RLHW	L- shaped (L)	High (H)	Welding (W)	911	3.99	114.2	-17	0.05
RLOE	L- shaped (L)	Ordinary (O)	Epoxy (E)	601	4.44	67.7	-10	0.21
RLHE	L- shaped (L)	High (H)	Epoxy (E)	634	4.00	79.3	-15	0.11
RCOW	Channel (C)	Ordinary (O)	Welding (W)	999	2.44	204.7	1	0.05
RCHW	Channel (C)	High (H)	Welding (W)	1215	1.76	345.2	10	0.02
RCOE	Channel (C)	Ordinary (O)	Epoxy (E)	743	3.12	119.1	12	0.06
RCHE	Channel (C)	High (H)	Epoxy (E)	888	2.33	190.6	19	0.04

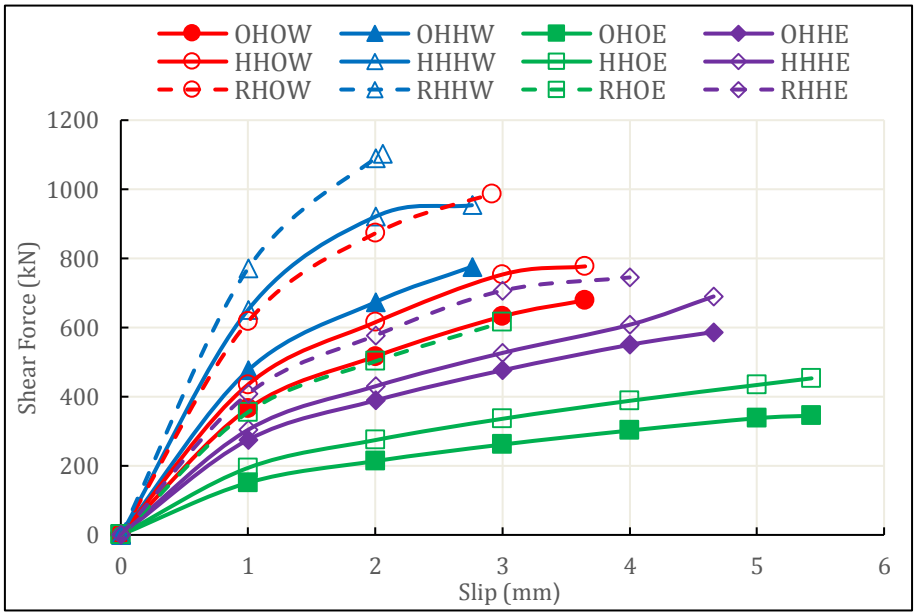

Fig. 17. Load slip curves of headed stud shear connectors with different types of concrete and bonds.

In Fig. 18, it appears that the weaker specimen with the minimum shear force resistance was the OLOE, where epoxy was used for bonding. The strongest specimen with the maximum shear force was the RLHW, where the welding was used for bonding purposes. Based on the test results, it was observed that the increase in the shear force value for the RLHW was around 29% and 61% when its shear force resistance was compared to the HLHW and the OLHW, respectively. As shown in Fig. 18, the load-slip curve of the RLHW with a fracture type of failure came to an end at a much shorter slip value (approximately 4 mm at a shear force value of 911 kN) while those related with the concrete failure types such as the OLOE exhibited a gradual drop at a much longer slip value (approximately 6.34 mm at a shear force value of 248 kN).

Based on the results plotted in Fig. 19, it appears that the weaker specimens with the minimum shear force values was the OCOE and HCOE, while the strongest one with the maximum shear force value was the RCHW. The increase in the shear force value of the RCHW was around 26% and 39% with respect to the shear force values of the HCHW and the OCHW, respectively.

Once again, the load-slip curve of the RCHW, where fracture type of failure occurred, came to an abrupt end at the slip value of 1.76 mm under 1,215 kN of shear

force. However, the specimens with concrete types of failures, such as the OCOE and HCOE exhibited a longer slip curve reaching maximum slip values of 3.23 mm and 2.87 mm at the shear force values of 634 kN and 607 kN, respectively.

Based on the overall test results extracted from the three previous figures (Figs. 17, 18 and 19), the reactive powder concrete, RPC, generated the maximum shear forces due to the increase in the compressive strength of concrete as compared to the OPC and HPC.

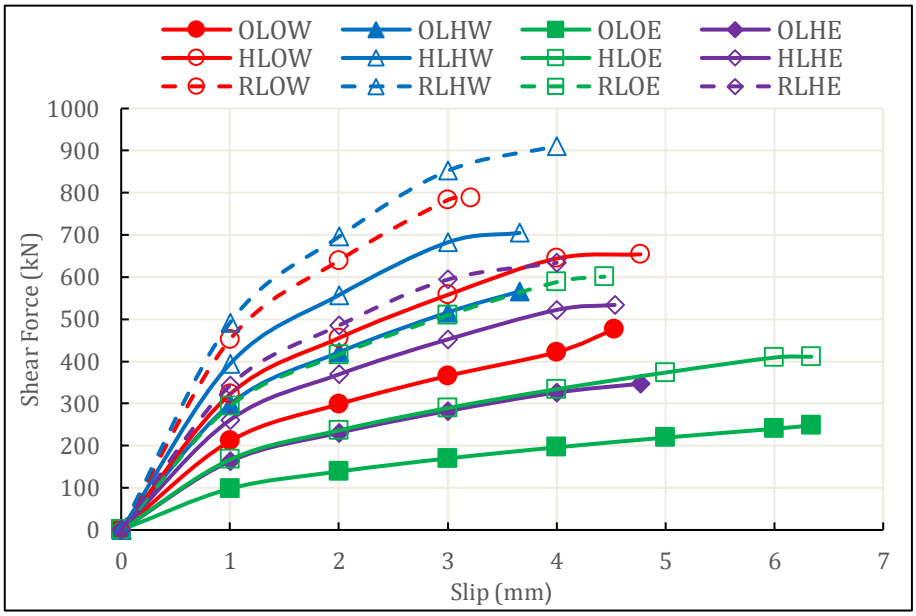

Fig. 18. Load slip curves of L-shaped shear connectors with different types of concrete and bonds.

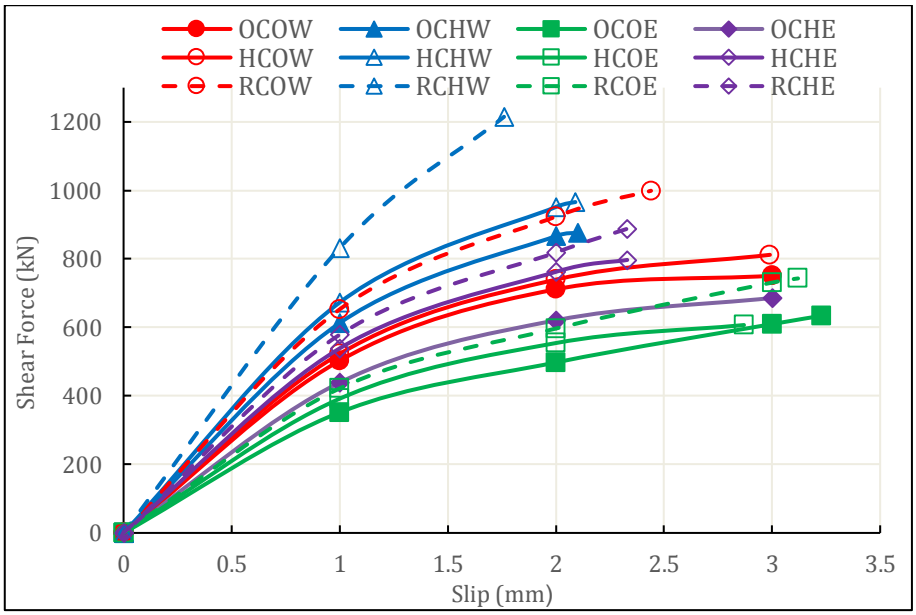

Fig. 19. Load slip curve of C-shaped shear connectors with different types of concrete and bonds.

4.3. Effect of bond type

The variation in the shear stiffness of connectors is studied for each concrete type. The details of the test results are provided in the next subsections.

The load-slip curves of shear studs in different types of concrete with varying bond types are presented in Figs. 20, 21, and 22. Based on the data illustrated in Fig. 20, it appears that the specimen with the minimum shear force capacity was the OLOE and the one with the maximum shear capacity was the OCHW. According to the test results, it was observed that the increase in the shear force capacity of the OCHW was around 17%, 38%, and 28% when the results were compared to those of the OCOW, OCOE, OCHE, respectively.

Based on the results plotted in Fig. 21, it appears that the specimen that generated the minimum shear force was the HLOE while the one that generated the maximum shear force was the HCHW. Based on the test results, it was observed that the increase in the shear force

value for specimen HCHW was around 19%, 59%, and 21% when the results were compared to those obtained from the HCOW, HCOE, HCHE, respectively.

Fig. 22 illustrates the load slip curves of shear studs in reactive powder concrete type (RPC) with different types of bonds. Based on the data plotted in Fig. 22, it appears that the specimen that generated the largest shear force was the RCHW and the one that generated the smallest shear force was the RLOE. It was observed that the increase in the shear force value of the RCHW was around 22%, 64%, and 37% when the results were compared to those of the RCOW, RCOE, RCHE, respectively.

Based on the overall results that are extracted from the three previous figures (Figs. 20, 21, and 22), it can be concluded that the C-shaped shear connectors resisted higher shear forces due to the increase in the surface contact area associated with the concrete. The load-slip curves of shear studs in the OCHW, HCHW, and RCHW exhibited fracture types of failures, and the testing came to an abrupt end whereas those related to the concrete failure, the OLOE, HLOE, and RLOE, exhibited a gradual drop with larger slip values.

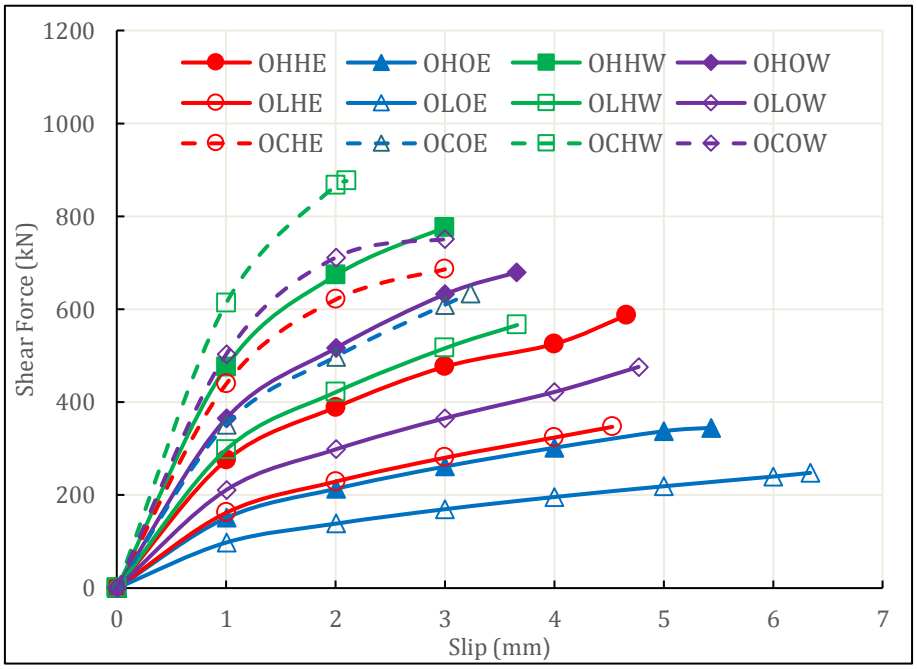

Fig. 20. Load slip curve of shear studs in an ordinary concrete type with different types of bonds.

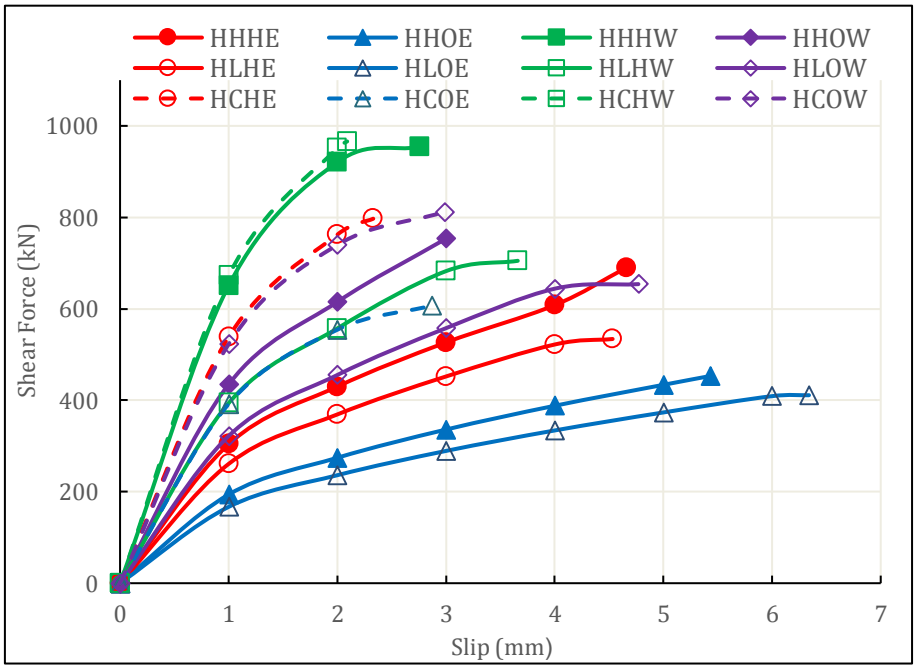

Fig. 21. Load slip curve of shear studs in high strength concrete with different types of bonds.

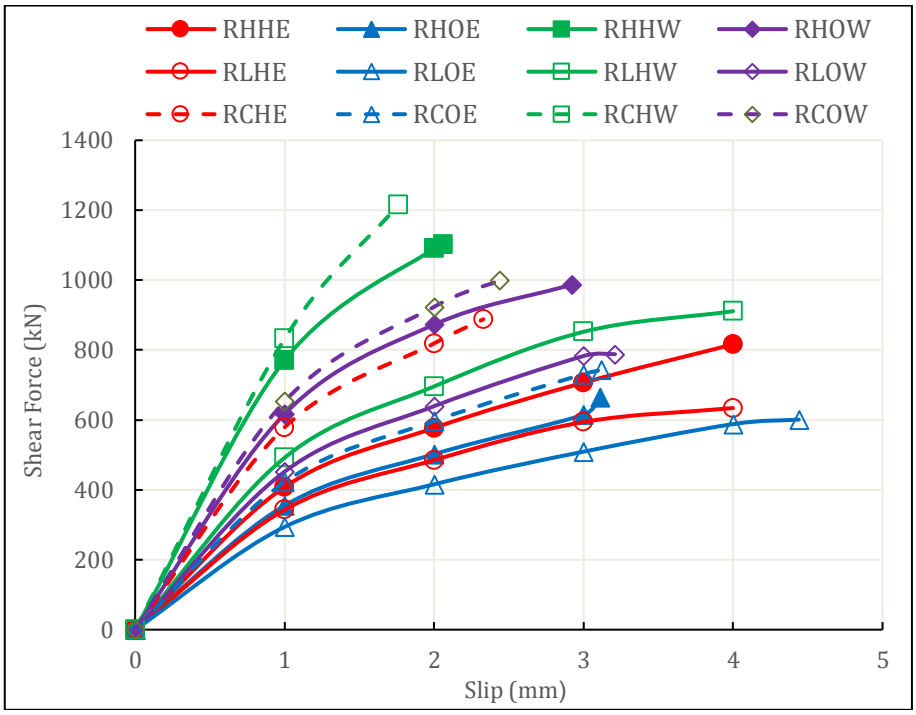

Fig. 22. Load slip curve of shear studs in reactive powder concrete with different types of bonds.

5. Conclusions

The test results are investigated in two separate groups. In the first group, the mechanical properties of different types of concrete were examined. In the second group, the test data from the push-out specimens were studied. The findings of this study can be applied to real world scenarios. Although a great deal of further research must be completed in this field, this study attempted to fill the gap by exploring the structural behaviours of various shaped shear connectors with welded and epoxy bonded connections in different types of concrete.

Mechanical Properties of Concrete:

- The compressive strength of concrete increases with age. The RPC and HSC generated the best compressive strength values by an increase of 348% and 218%, respectively, when their results were compared to that of normal concrete at 28 days.
- The splitting tensile and flexural strength values of concrete increased when the RPC and the HSC were used. The RPC and HSC generated higher strength values compared to that of normal concrete. The increase in the splitting tensile strength of the RPC and the HSC at 28 days with respect to that of normal concrete was 358% and 274%, respectively, while in the flexural strength case, the increase was 371% and 250%, respectively. For the NFC, the maximum splitting tensile and flexural strengths were 2.0 MPa and 2.7 MPa.
- The values of Static Modulus of Elasticity increased in the RPC and HSC. The RPC and HSC generated 76% and 35% more modulus of elasticity compared to that of normal concrete at 28 days.

Push-out Specimens:

In this group, the maximum shear forces were compared to those from the headed stud case since the headed stud shear connectors were commonly used in practice.

- OCHW generated the best shear force value of 876 kN with a percentage of difference of 87% when the result was compared to the force of OHHW.
- HCHW produced the best shear force value of 966 kN with a percentage of difference of 1.3% when the result was compared to the shear force value generated in HHHW.
- RCHW resisted the largest shear force value of 1215 kN, with a percentage of difference of 10% when the result was compared to that of RHHW.

Based on the test results, the reactive powder concrete generated the largest shear force values for all shear stud types. Below, a more in-depth comparison is presented:

- The increase in the shear force value of headed studs welded in RHHW was around 16% and 42% when the result was compared to those of HHHW and OHHW, respectively. If epoxy is used instead of welding, then the increase in the same specimens with epoxy became 8% and 27%, respectively.
- The increase in the shear force value of L-shaped studs welded in RLHW was around 29% and 61% when the results were compared to those of HLHW and OLHW, respectively. If epoxy is used, then the increase in the same specimens became 19% and 83%, respectively.
- The increase in the shear force value of C-shaped studs welded in RCHW was around 25% and 39% when the results were compared to those of HCHW

and OCHW, respectively. If epoxy is used, then the increase in these specimens with epoxy was 11% and 30%, respectively.

The shear resistance of welded and epoxy bonded shear studs were also compared to each other. Below list includes the detailed comparisons among the specimens:

- The increase in the shear force value of OCHW was around 28%, 17% and 38% when the result was compared to those of OCHE, OCOW, and OCOE, respectively.
- The increase in shear force value for HCHW was around 21%, 19% and 59% when the shear force was compared to those of HCHE, HCOW, and HCOE, respectively.
- The increase in the shear force value of RCHW was around 37%, 22% and 64% when the shear force value was compared to those generated in RCHE, RCOW, and RCOE, respectively.

Acknowledgements

We would like to acknowledge the assistance of Osamah Mahmood Hussein during the testing phase of this study.

References

Adekola AO (1968). Partial interaction between elastically connected elements of a composite beam. *International Journal of Solids and Structures*, 4(11), 1125-1135.

Al-Shafi'i NTH (2013). Shear Behavior of Reactive Powder Concrete T-beams. *Ph.D. thesis*, Department of Civil Engineering, University of Al-Mustansiriya, Baghdad, Iraq.

Aziz KI (2005). Behavior of Multi-layer Composite Beams with Partial Interaction. *Ph.D. thesis*, Department of Civil Engineering, University of Technology, Baghdad, Iraq.

Bae BI, Chung JH, Choi HK, Jung HS, Choi CS (2018). Experimental study on the cyclic behavior of steel fiber reinforced high strength concrete columns and evaluation of shear strength. *Engineering Structures*, 157, 250-267.

Di J, Zou Y, Zhou X, Qin F, Peng X (2018). Push-out test of large perfobond connectors in steel–concrete joints of hybrid bridges. *Journal of Constructional Steel Research*, 150, 415-429.

EN 1994 - Eurocode 4 (1994). Design of composite steel and concrete structures. European Committee for Standardization, Brussels, Belgium.

Fallah S, Nematzadeh M (2017). Mechanical properties and durability of high-strength concrete containing macro-polymeric and polypropylene fibers with nano-silica and silica fume. *Construction and Building Materials*, 132, 170-187.

He S, Fang Z, Mosallam AS (2017). Push-out tests for perfobond strip connectors with UHPC grout in the joints of steel-concrete hybrid bridge girders. *Engineering Structures*, 135, 177-190.

Hirama C, Ishikawa T, Hisagi A (2017). Special Issue: Proceedings of Eurosteel 2017. *In: Jönnsso J, editor. Shear strength of headed stud push-out tests: comprehensive literature review focusing on slab type, failure mode, and large-diameter headed stud*. Wiley Online Library , 2013-2022.

Hmeed YM (2014). Behavior of reinforced concrete I-beams containing reactive powder concrete. *Ph.D. thesis*, Department of Civil Engineering, University of Al-Mustansiriya, Baghdad, Iraq.

Ismael MA (2013). Flexural Behavior of Reactive Powder Concrete Tee Beams. *Ph.D. Dissertation*, Department of Civil Engineering, University of Al-Mustansiriya, Baghdad, Iraq.

Newmark, NM, Siess, CP, Viest IM (1951). Tests and analysis of composite beams with incomplete interaction. *Proceedings of the Society for Experimental Stress Analysis*, 9(1), 75-92.

Wandscher VF, Marchionatti AME, Otani A, Bergoli CD, Cesar PF, Valandro LF (2018). Effects of bonding area size, surface treatment and specimen configuration on the push out test for assessing bonding and stress distribution to Y-TZP. *International Journal of Adhesion and Adhesives*, 85, 315-321.

Wardi AHW (2019). Behavior of High Strength Shear Connectors Embedded in Concrete. *M.Sc. thesis*, Department of Civil Engineering, Atılım University, Ankara, Turkey.

Challenge Journal of Structural Mechanics

Research Article

Numerical investigation of sloshing with baffles having different elasticities

Abdullah Demir [a,*], Ali Ersin Dinçer [b]

[a] *Department of Civil Engineering, Erzurum Technical University, 25050 Erzurum, Turkey*
[b] *Department of Civil Engineering, Abdullah Gül University, 38080 Kayseri, Turkey*

ABSTRACT

Liquid tanks are indispensable members of civil engineering structures like liquid petroleum gas storage tanks and aerospace structures. Fluids can act unpredictably under earthquake excitation or dynamic loads. Loads applied to tank changes during motion and there can be deformations at the tank or even at the structure where the tank is placed. This is called sloshing and many researchers study the behavior of it. In this research, behavior of baffles having different elastic modulus is investigated by a fluid-structure interaction (FSI) method. The numerical method is a fully coupled FSI method proposed by the authors, recently. The method, which is verified by many problems, uses smoothed particle hydrodynamics (SPH) for fluid domain, finite element method (FEM) for structural domain and contact mechanics for coupling of these two domains. In analysis, a tank and a baffle having constant initial geometry are excited by harmonic motions. Elasticity of baffle is changed to investigate the effect on sloshing. Results show that tip displacement of baffle has linear relation with its elasticity for higher rigidities. In contrast, tip displacement of baffle has constant tip displacement for lower rigidities.

ARTICLE INFO

Article history:
Received 17 June 2020
Revised 27 July 2020
Accepted 21 August 2020

Keywords:
Fluid-structure interaction
Smoothed particle hydrodynamics
Baffle
Sloshing

1. Introduction

Sloshing is a phenomenon causing high pressure on the walls of the liquid tanks. Dynamic movements of liquid causes sloshing. While only hydrostatic pressures are observed in a stationary liquid tank, higher pressures occur in a moving tank. Although the liquid tank differs in shape or usage area (Marsh et al., 2011), sloshing is a condition for all. Tanks may be in the shape of prismatic (Liu and Lin, 2009), cylindrical (Hasheminejad and Mohammadi, 2011) or silo (Maleki and Ziyaeifar, 2008) and contain water, oil or liquefied fuels. Liquid tanks existing in many areas from water tanks on the building roofs to spacecrafts containing liquid fuel are exposed to different excitations under the effect of sloshing.

In order to reduce the increasing loads during sloshing, researchers used different tank shapes or placed baffles inside the tank. Using baffles in the liquid tanks, which basically limit the movement area of the liquid, has been the subject of many studies. Baffles were placed in different parts of the tanks in different sizes and their effects on sloshing were investigated. While ring-shaped (Gavrilyuk et al., 2006; Modaressi-Tehrani et al., 2007) or floating (Koh et al., 2013; Lishi et al., 2013) baffles are placed in cylindrical and silo tanks, plate-shaped baffles (Akyildiz, 2012) are used in rectangular tanks in different positions. The baffles change the flow direction of the liquid or in other words, limit the flow area of the liquid, so the force on the walls of the tank is reduced.

Baffles were mostly designed as rigid plates in the literature (Biswal et al., 2006). Since the baffles and liquid tanks are assumed to be rigid bodies, the computational area is only the liquid area. Various fluid models to analyze the sloshing effects proposed in the literature. The examples of the proposed models may be finite element model (FEM) (Biswal et al., 2006), volume of fluid (VOF) (Jung et al., 2012), variational boundary element method (VBM) (Gedikli and Ergüven, 2003), smoothed particle

* *Corresponding author*. Tel.: 444-5-388 ; Fax: +90-442-230-0036 ; E-mail address: abdullah.demir@erzurum.edu.tr (A. Demir)
ISSN: 2149-8024 / DOI: https://doi.org/10.20528/cjsmec.2020.04.002

hydrodynamics (SPH) (Cao et al., 2014; Chen et al., 2013; Demir et al., 2019; Dinçer et al.,2019; Serván-Camas et al., 2016), moving particle semi-implicit method (MPS) (Demir and Dinçer, 2017) and consistent particle method (CPM) (Koh et al., 2013). In recent years, the use of particle-based methods in fluid modelling has increased, the most popular of these methods may be SPH.

There are few studies in the literature where baffles are considered as elastic structures. In one of these studies (Bermúdez et al., 2003), the baffle was placed in the middle of a rectangular tank as a thin steel plate. The interaction between the structure and the liquid was investigated by the added mass method. In a similar study (Hernández and Santamarina, 2012), steel plates were placed on the walls of the rectangular tank. In the literature, there are studies (Hwang et al., 2015; Hwang et al., 2016; Madhumitha et al., 2017) in which the structures having considerably small modulus of elasticity were used as baffles. In these studies, the sloshing effect was investigated under rotational motions.

In this study, elastic baffles are focused on. The behavior of the elastic baffle placed in the middle of a rectangular tank partially filled with water and its effect on sloshing are observed. In the simulations, the baffles with different modulus of elasticities are used. Thus, the effect of the modulus of elasticity of the baffle on sloshing is investigated.

The analyses are carried out with the SPH-FEM based fluid-structure coupling method which was recently introduced to the literature by the authors and whose verification has been completed with many models (Demir et al., 2019; Dinçer, 2019; Dinçer et al., 2019; Dinçer et al., 2017). In this method, SPH and FEM are used for the simulation of the fluid and solid domains of the problem, respectively. The interaction of fluid and solid parts is satisfied with contact mechanics. In the next part of the study, the equations of the SPH method used in the analysis of the fluid part are given, then the equations of the finite element method used in the analysis of the structural part are defined. Then, contact mechanics are explained. After that, simulation setup is defined, results are presented and conclusions are drawn.

2. Numerical Methods

2.1. Smoothed particle hydrodynamics (SPH)

SPH is a particle-based method. The differential equations of the particle motion are converted to ordinary differential equations using the kernel function. The change in density, ρ_i, velocity, V_i, and position, r_i of ith particle with respect to time can be expressed as:

$$\frac{d\rho_i}{dt} = \sum_{j=1}^{N} m_j V_{ij}.W_{ij} \tag{1}$$

$$\frac{dV_i}{dt} = \sum_{j=1}^{N}\left(\frac{P_i}{{\rho_i}^2}+\frac{P_j}{{\rho_j}^2}+\pi_{ij}\right).\nabla W_{ij} + f_b + \Delta\kappa \tag{2}$$

$$\frac{dr_i}{dt} = V_i + 0.05\sum_{j=1}^{N} m_j\left(\frac{V_{ij}}{\rho_i}\right)W_{ij} \tag{3}$$

where, i and j are the neighboring particles, m is the mass, V_{ij} is the velocity difference between two neighboring particles, f_b is the body forces including the gravitational acceleration, $\Delta\kappa$ is the contact force applied from the solid body, W_{ij} is the kernel function and ∇W_{ij} is the gradient of kernel. In the study a cubic spline kernel is used.

$$W_{ij} = W(|r_{ij}|, h) \tag{4}$$

where, h is the smoothing length and taken as 1.33 times the initial particle spacing. According to Eq. (3), a stabilizer is added to the velocity of the particles to lower the velocity difference of two neighboring particles. In addition, an artificial viscosity, π_{ij}, is used in Eq. (2) to lower the numerical oscillations. The equation of the artificial viscosity,

$$\pi_{ij} = \frac{\varphi{\mu_{ij}}^2 - \phi\mu_{ij}c_{ij}}{\rho_{ij}} \tag{5}$$

$$\mu_{ij} = \frac{h\boldsymbol{V}_{ij}.\boldsymbol{r}_{ij}}{{\boldsymbol{r}_{ij}}^2+0.001h^2} \tag{6}$$

where, φ and ϕ are the empirical constants and taken as 0.2 and 1, respectively, c is the speed of sound and r_{ij} is the position difference between two neighboring particles.

In order to find the pressure, P, the fluid can be assumed slightly compressible and the equation of state can be used. According to the equation of state, the pressures depend on the initial pressure, P_0, and initial density, ρ_0 are shown in Eq. (7).

$$P = P_0\left[\left(\frac{\rho}{\rho_0}\right)^7 - 1\right] \tag{7}$$

Leap-frog algorithm is used for discretization of time. The maximum time step size is calculated from Courant-Friedrichs-Lewy (CFL) condition (Anderson, 1995; Hirsch, 2007). In the modeling of fixed walls, mirror particles are used to provide the sliding boundary condition. The boundary between the elastic baffle and fluid field is satisfied by the contact mechanics described in the following sections.

2.2. Finite element method (FEM)

The well-known equation of motion can be defined as:

$$M\ddot{u} + C\dot{u} + Ku = F \tag{8}$$

where, M is the mass, C is the damping, K is the stiffness matrix, u is the displacement, $\dot{u}$ is the velocity and $\ddot{u}$ is the accelearation.

$M = \int_V \rho N^T N dV$

$C = \int_V \mu N^T N dV$

$K = \int_V {B_L}^T E B_L dV + \int_V {B_{NL}}^T S B_{NL} dV$

$F = \int_V N^T f dV$

where, ρ is the density, μ is a constant, E constitutive matrix, S is the second Piola Kirchoff stress tensor and f

is the body force vector. Time discretization is satisfied with Wilson-θ method (Wilson et al., 1972) and given as:

$$\hat{K}u^{t+1} = \hat{F} \tag{9}$$

where the stiffness matrix $\hat{K}$ and, the force vector, $\hat{F}$, can be calculated as:

$$\hat{K} = \frac{6}{(\theta\Delta t)^2}M + \frac{3}{\theta\Delta t}C + K$$

$$\hat{F} = \left(3M + \frac{\theta\Delta t}{2}C\right)\ddot{u}^t + \left(\frac{6}{\theta\Delta t}M + 3C\right)\dot{u}^t + \theta F$$

where, Δt is the time step and θ is a constant and suggested to take as 1.42. Therefore, the velocity and the acceleration vectors are obtained as:

$$\ddot{u}^{t+1} = \left(1 - \frac{3}{\theta}\right)\ddot{u}^t - \left(\frac{6}{\theta^2\Delta t}\right)\dot{u}^t + \left(\frac{6}{\theta^3\Delta t^2}\right)u^{t+1}$$

$$\dot{u}^{t+1} = \left(\Delta t - \frac{3\Delta t}{2\theta}\right)\ddot{u}^t + \left(1 - \frac{3}{\theta^2}\right)\dot{u}^t + \left(\frac{3}{\theta^3\Delta t}\right)u^{t+1}$$

2.3. Coupling method

A node to line contact potential can be defined as (Bathe and Chaudhary, 1985; Dinçer et al., 2019):

$$\Pi_{inv} = \left(\kappa_{inv}^{t+\Delta t} + \Delta\kappa_{inv}\right)^T\left[(\Delta u_{inv} + O_{inv}) - (1-\eta)\Delta u_F - \eta\Delta u_S\right] \tag{10}$$

where, inv is the invader node, $\kappa_{inv}^{t+\Delta t}$ is the contact force at $t + \Delta t$, $\Delta\kappa_{inv}$ is the incremental contact force, Δu_{inv} is the incremental displacement of the invading particle, O_{inv} is the invasion amount, Δu_F and Δu_S are the incremental displacements of the first and second nodes of the line element, respectively. η is a parameter defining the position from the first node of the line element.

$$\eta = \frac{n^T}{l}\left[(P_{inv}^{t+\Delta t} - O_{inv}^{t+\Delta t}) - P_F^{t+\Delta t}\right] \tag{11}$$

where, n is the unit normal vector of the line element, l is the length of the line element, $P_{inv}^{t+\Delta t}$ ve $P_F^{t+\Delta t}$, are the positions of the SPH particle and node at $t + \Delta t$, respectively.

A new potential Π_{new} is obtained by subtracting the contact potentials obtained from the summation of each invading particle from the existing potential, Π. By combining the new potential with Eq. (10), incremental finite element equations including the contact potentials are obtained.

$$\begin{bmatrix} K_{solid}^{t+\Delta t} & K_c^{t+\Delta t} \\ (K_c^{t+\Delta t})^T & 0 \end{bmatrix}\begin{bmatrix} \Delta U \\ \Delta\kappa_{inv} \end{bmatrix} = \begin{bmatrix} R^{t+\Delta t} \\ 0 \end{bmatrix} - \begin{bmatrix} F^{t+\Delta t} \\ 0 \end{bmatrix} + \begin{bmatrix} R_c^{t+\Delta t} \\ O_{inv}^{t+\Delta t} \end{bmatrix} \tag{12}$$

where, $K_{solid}^{t+\Delta t}$, $K_c^{t+\Delta t}$ are the stiffness matrices of the structure and contact, respectively, ΔU is the incremental displacement vector, $R^{t+\Delta t}$ is the total applied external force vector, $F^{t+\Delta t}$ is the equivalent nodal force vector, $R_c^{t+\Delta t}$ is the contact force vector element.

At this stage, the mass participation of the invading particles should be added to the set of equations shown in Eq. (12) so that they can be solved together with the structure. In order to ensure this participation, in the Newmark method (Newmark, 1959), the α and β coefficients are used by taking 0.5 and 0.25 respectively. In other words, the mass matrix of invading particles $M_{inv}^{t+\Delta t}$ should be multiplied by 2 / (Δt^2) before putting it into Eq. (12). A more detailed derivation of the contact potential of the node to line (Dinçer et al., 2019) or line to line (Bathe and Chaudhary, 1985) can be followed from previous studies.

3. Numerical Setup and Results

Reducing the sloshing effect in tanks may be possible by increasing the performance of the baffles. For this purpose, the researchers previously placed the baffles in different parts of the tanks in different shapes and sizes. In this study, the effect of modulus of elasticity of baffles are observed. As seen in Fig. 1, numerical simulations are carried out with a plate-shaped baffle placed in the middle-bottom of a rectangular tank. The length of fluid tank is 30 cm and it is partly filled with water having a depth of 10 cm. The thickness and the height of the elastic baffle are 3 mm and 8 cm, respectively.

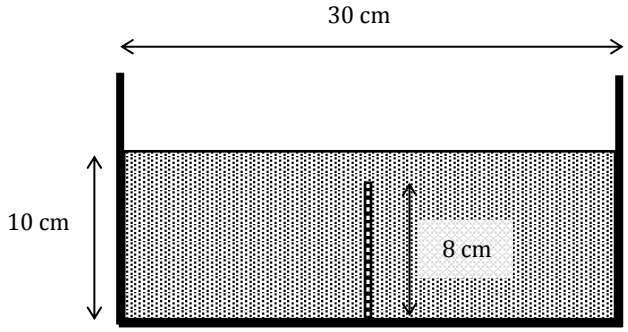

Fig. 1. Numerical setup.

The walls of the tank are assumed rigid. The modulus of elasticities of the baffle are taken between 1.0x10^6 Pa and 1.0x10^{11} Pa and for this study 7 different modulus of elasticities are used within this range. In the simulations, the Poisson's ratio is taken as 0.3. The ground motion used in the analyses is harmonic, has an amplitude of 10 mm and a frequency of 2.4 Hz, and is given in Fig. 2. A single harmonic motion is selected to limit the context of this research in which the harmonic motion is selected depending on achieving clear and visible motion of baffle and free surfaces.

In the numerical model, the rigid walls of the tank are simulated with the mirror particle method as stated in the SPH section of the article. Finite element method is used for the model of elastic structure. In this model, 200 four-point quadrilateral finite elements are used. The mesh size is found to be sufficient for the mesh independency. For the fluid part, the distance between the particles is chosen as 1.5 mm and therefore, 10546 SPH particles are used. The time step is calculated from CFL condition and found as 0.016 ms.

The tip displacements of baffles for the different modulus of elasticity values are given in Fig. 3. The

ranges of vertical axis of figures are changed in proportion to the increase in modulus of elasticity. Modulus values are naturally existing values. The baffle is first assumed to be a steel and decreased up to a numerically logical minimum value so that the convergence is always satisfied.

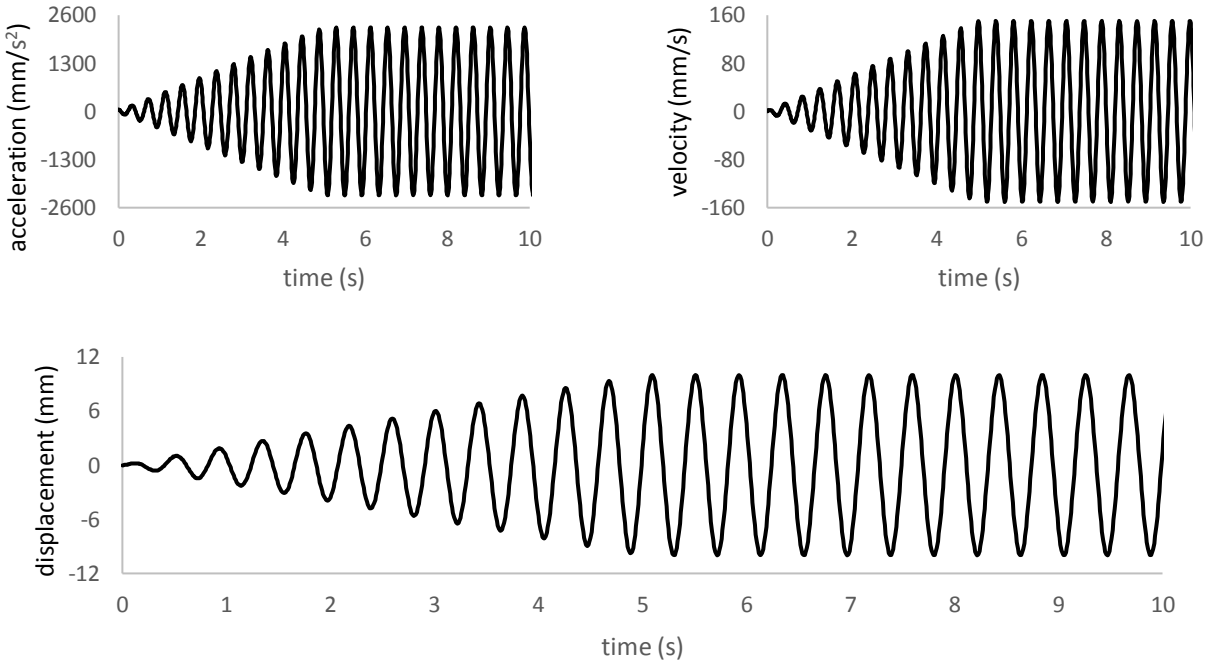

Fig. 2. The acceleration, velocity and displacement of applied ground motion.

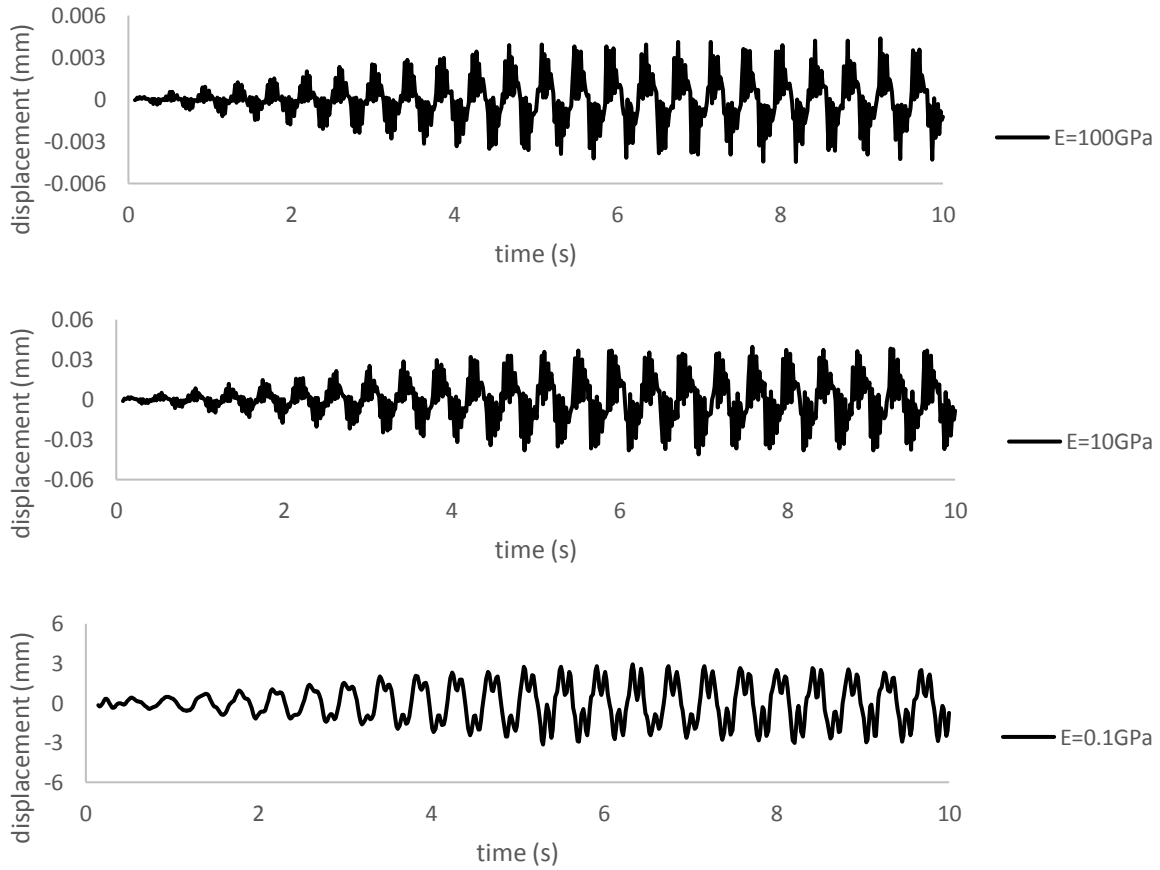

Fig. 3. (continued).

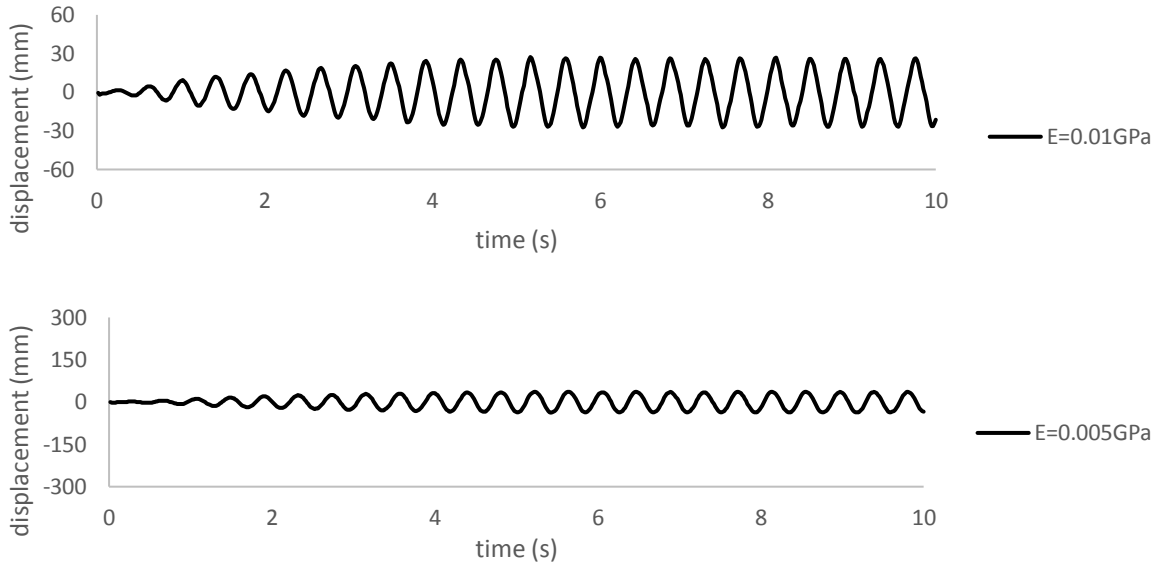

Fig. 3. The tip displacements of baffle for different modulus of elasticities.

As seen in Fig. 3, the proposed method is successful to obtain solutions for baffle with a wide range of elastic modules. For values of modulus of elasticity above 1.0 GPa, tip displacements are observed below 1mm. The oscillations are unclear or consists sound for the baffles having higher elastic modulus, because their tip displacements are very small. Consequently, in the baffles having modulus of elasticity below 1.0 GPa, the sound disappeared and oscillation/harmonic motion becomes dominant. The baffle with an elastic modulus of 0.01 GPa displaces at an amplitude greater than the harmonic ground motion, whose amplitude is 10 mm.

It can be seen in Fig. 3 that the modulus of elasticity is in a linear relationship with the tip displacement of the baffle. This relationship can also be observed in Fig. 4, which shows the maximum tip displacements of baffles in different modulus of elasticities drawn in logarithmic scale. However, this linear relationship lasts up to the baffle having the modulus of elasticity of 0.01 GPa, where the maximum tip displacement is 27 mm, then linearity is replaced by a fixed maximum tip displacement. The maximum tip displacement observed in the simulations is 36 mm.

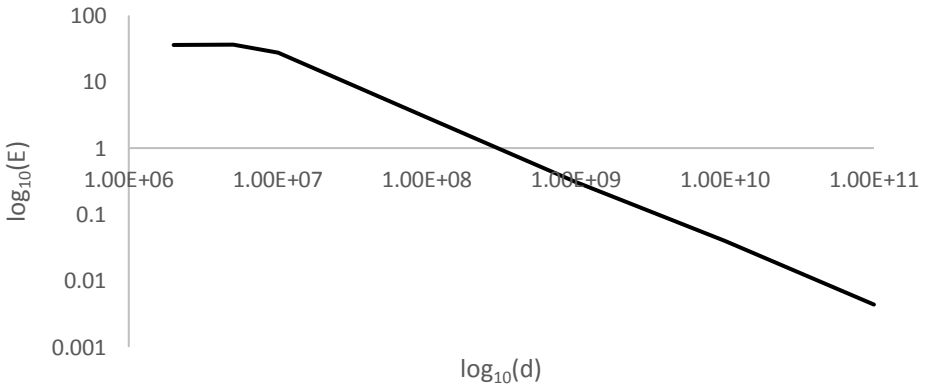

Fig. 4. Modulus of elasticity vs tip displacement.

The maximum tip displacement of the baffle having linear relationship with elasticity, which is the linear part of Fig. 4, is obtained where the harmonic motion passes approximately from the starting point which can be seen in Fig. 5. On the other hand, when the linearity is impaired, that is, the elasticity falls below 0.01 GPa, the maximum tip displacement of baffle shifts towards the instants when the harmonic motion reaches the opposite directional maximum displacement which can also be clearly seen in Fig. 5.

In modulus of elasticity values in which linearity is impaired, tip displacement of the baffles tends to remain constant. The reason can be described by the period shift shown in Fig. 5. The period shift can also be explained with the change in water free-surfaces for the baffles having different modulus of elasticities given in Fig. 6. In addition, the water free-surfaces are stagnant for the baffles with lower modulus of elasticities since they displace in harmony with the water.

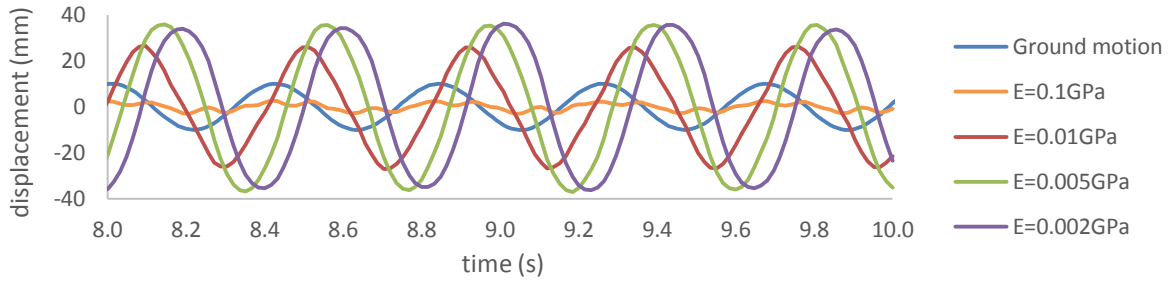

Fig. 5. The comparison of the tip displacement and harmonic ground motion.

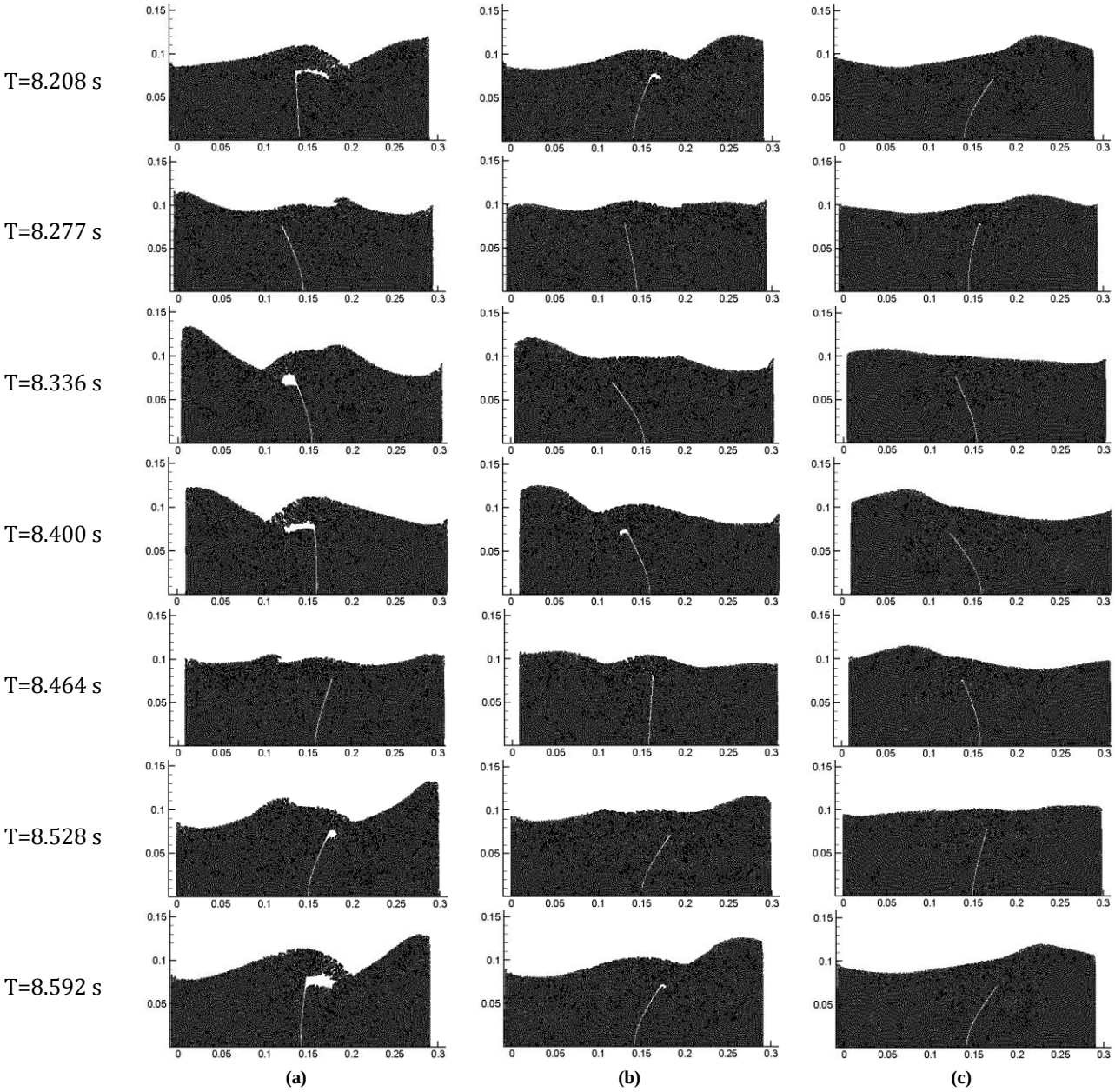

Fig. 6. Water free-surface profiles for the baffle having the modulus of elasticity of (a) 0.01 GPa; (b) 0.05 GPa; (c) 0.002 GPa.

4. Conclusions

In the study, the effect of baffles having different modulus of elasticities on sloshing is observed. The fluid-structure interaction method developed in the previous studies of the authors and validated for different problems is used for the analyzes in this study. In the simulations, the relationship between modulus of elasticity and tip displacement of baffle is determined. This relation is linear for higher elasticities and constant for lower elasticities. It is found that in the case where the modulus of elasticity of the baffle is sufficiently reduced, almost constant

tip displacement is observed because the baffle cannot resist the motion of water. In contrast, in the case where the modulus of elasticity of the baffle is higher, the relationship between modulus of elasticity and tip displacement is found to be linear. The relationship between the tip displacement and the modulus of elasticity of baffle depends on the shape of the tank, the depth of the fluid and the ground motion, etc. The scope of the study is narrowed by keeping the geometry and ground motion constant. Therefore, the relationship between the modulus of elasticity and tip displacement of the baffle cannot be generalized in the scope of this study. A more comprehensive study is planned based on the simulation results obtained in this study.

References

Akyildiz H (2012). A numerical study of the effects of the vertical baffle on liquid sloshing in two-dimensional rectangular tank. *Journal of Sound and Vibration*, 331(1), 41–52.

Anderson JD (1995). Computational Fluid Dynamics: The Basics with Applications. New York: McGraw-Hill.

Bathe KJ, Chaudhary A (1985). A solution method for planar and axisymmetric contact problems. *International Journal for Numerical Methods in Engineering*, 21(1), 65–88.

Bermúdez A, Rodríguez R, Santamarina D (2003). Finite element computation of sloshing modes in containers with elastic baffle plates. *International Journal for Numerical Methods in Engineering*, 56(3), 447–467.

Biswal KC, Bhattacharyya SK, Sinha PK (2006). Non-linear sloshing in partially liquid filled containers with baffles. *International Journal for Numerical Methods in Engineering*, 68(3), 317–337.

Cao XY, Ming FR, Zhang AM (2014). Sloshing in a rectangular tank based on SPH simulation. *Applied Ocean Research*, 47, 241–254.

Chen Z, Zong Z, Li HT, Li J (2013). An investigation into the pressure on solid walls in 2D sloshing using SPH method. *Ocean Engineering*, 59, 129–141.

Demir A, Dinçer AE (2017). MPS ve FEM Tabanlı akışkan-yapı etkileşimi modelinin Çoruh Nehri üzerindeki ardıl baraj-yıkılma problemine uygulanması. *Doğal Afetler ve Çevre Dergisi*, 1–6. (in Turkish)

Demir A, Dinçer AE, Bozkus Z, Tijsseling AS (2019). Numerical and experimental investigation of damping in a dam-break problem with fluid-structure interaction. *Journal of Zhejiang University: Science A*, 20(4), 258–271.

Dinçer AE (2019). Investigation of the sloshing behavior due to seismic excitations considering two-way coupling of the fluid and the structure. *Water*, 11(12), 2664.

Dinçer AE, Demir A, Yavuz C (2017). A Preliminary study for fluid structure interaction model by smoothed particle hydrodynamics and contact mechanics. *37th IAHR World Congress*.

Dinçer AE, Demir A, Bozkus Z, Tijsseling AS (2019). Fully coupled smoothed particle hydrodynamics-finite element method approach for fluid-structure interaction problems with large deflections. *Journal of Fluids Engineering, Transactions of the ASME*, 141(8), 1–13.

Gavrilyuk I, Lukovsky I, Trotsenko Y, Timokha A (2006). Sloshing in a vertical circular cylindrical tank with an annular baffle. Part 1. Linear fundamental solutions. *Journal of Engineering Mathematics*, 54(1), 71–88.

Gedikli A, Ergüven ME (2003). Evaluation of sloshing problem by variational boundary element method. *Engineering Analysis with Boundary Elements*, 27(9), 935–943.

Hasheminejad SM, Mohammadi MM (2011). Effect of anti-slosh baffles on free liquid oscillations in partially filled horizontal circular tanks. *Ocean Engineering*, 38(1), 49–62.

Hernández E, Santamarina D (2012). Active control of sloshing in containers with elastic baffle plates. *International Journal for Numerical Methods in Engineering*, 91(6), 604–621.

Hirsch C (2007). Numerical Computation of Internal and External Flows: The Fundamentals of Computational Fluid Dynamics. Elsevier.

Hwang SC, Gotoh H, Khayyer A, Park JC (2015). Simulations of Incompressible Fluid Flow-Elastic Structure Interactions by a Coupled Fully Lagrangian Solver. *The Proceedings of The Twenty-fifth International Ocean and Polar Engineering Conference*, 21-26 June, Kona, Hawaii, USA (p. 8).

Hwang SC, Park JC, Gotoh H, Khayyer A, Kang KJ (2016). Numerical simulations of sloshing flows with elastic baffles by using a particle-based fluid-structure interaction analysis method. *Ocean Engineering*, 118, 227–241.

Jung JH, Yoon HS, Lee CY, Shin SC (2012). Effect of the vertical baffle height on the liquid sloshing in a three-dimensional rectangular tank. *Ocean Engineering*, 44, 79–89.

Koh CG, Luo M, Gao M, Bai W (2013). Modelling of liquid sloshing with constrained floating baffle. *Computers and Structures*, 122, 270–279.

Lishi W, Zhuang W, Yuchun L (2013). A SPH simulation on large-amplitude sloshing for fluids in a two-dimensional tank. *Journal of Earthquake Engineering and Engineering Vibration*, 12(1), 135–142.

Liu D, Lin P (2009). Three-dimensional liquid sloshing in a tank with baffles. *Ocean Engineering*, 36(2), 202–212.

Madhumitha R, Arunkumar S Karthikeyan KK, Krishnah S, Ravichandran V, Venkatesan M (2017). Computational modeling and analysis of fluid structure interaction in micromixers with deformable baffle. *International Journal of Chemical Reactor Engineering*, 15(3), 20160121.

Maleki A, Ziyaeifar M (2008). Sloshing damping in cylindrical liquid storage tanks with baffles. *Journal of Sound and Vibration*, 311(1–2), 372–385.

Marsh A, Prakash M, Semercigil E, Turan ÖF (2011). A study of sloshing absorber geometry for structural control with SPH. *Journal of Fluids and Structures*, 27(8), 1165–1181.

Modaressi-Tehrani K, Rakheja S, Stiharu I (2007). Three-dimensional analysis of transient slosh within a partly-filled tank equipped with baffles. *User Modeling and User-Adapted Interaction*, 45(6), 525–548.

Newmark NM (1959). A Method of computation for structural dynamics. *Journal of the Engineering Mechanics Division*, 85(3), 67–94.

Serván-Camas B, Cercós-Pita JL, Colom-Cobb J, García-Espinosa J, Souto-Iglesias A (2016). Time domain simulation of coupled sloshing–seakeeping problems by SPH–FEM coupling. *Ocean Engineering*, 123, 383–396.

Wilson EL, Farhoomand I, Bathe KJ (1972). Nonlinear dynamic analysis of complex structures. *Earthquake Engineering & Structural Dynamics*, 1(3), 241–252.

Challenge Journal of Structural Mechanics

Research Article

The effect of slenderness on the lateral-torsional buckling and ultimate shear capacity of plate girders

Celal Cakiroglu [a,*], Kamrul Islam [b], Gebrail Bekdaş [c]

[a] *Department of Civil Engineering, Turkish-German University, 34820 İstanbul, Turkey*
[b] *Department of Civil, Geological and Mining Engineering, Polytechnique Montréal, H3T 1J4 Montréal (Québec), Canada*
[c] *Department of Civil Engineering, İstanbul University-Cerrahpaşa, 34320 İstanbul, Turkey*

ABSTRACT

Lateral torsional buckling and shear buckling are two of the most significant structural responses that should be considered during the design process of plate girders. Particularly the importance of lateral torsional buckling was once again witnessed during the reconstruction process of a bridge in Edmonton, Alberta, Canada when the plate girders failed due to insufficient bracing. This current study aims to acquire a better understanding of the effect of geometric parameters such as the web slenderness, flange slenderness and span-to-depth ratio on the critical buckling moment and ultimate shear strength of plate girders. To achieve this goal the critical buckling moment and ultimate shear strength of a plate girder were parametrically studied for a large number of geometries using a load case from an experimental study. The results of this parametric study clarified the effects of web slenderness, flange slenderness and span-to-depth ratio on the structural performance of a plate girder. The visualization of the results was used to identify the ranges of these geometric parameters where the structural performance is most sensitive to changing them.

ARTICLE INFO

Article history:
Received 29 June 2020
Revised 21 August 2020
Accepted 10 September 2020

Keywords:
Lateral-torsional buckling
Slenderness
Shear
Parametric study
Tension field theory

1. Introduction

Lateral-torsional and shear buckling are known to be two of the major failure modes of slender structural members. While the web of the plate girders is the primary element resisting the shear buckling, the flanges of them are primarily carrying the bending and torsional loads. Both of these failure modes were investigated extensively in order to obtain analytical formulations that predict the load carrying capacity of structures subjected to shear forces and bending moments accurately. The research works done by Nethercot (1974), Fukumoto et al. (1980), and MacPhedran and Grondin (2011), can be mentioned among the notable works investigating lateral-torsional buckling. Particularly plate girders with doubly symmetric I-sections have been the subject of comprehensive research. The importance of having a sound understanding of the buckling behavior of plate girders was once again seen during the replacement project of the 102 Avenue Bridge over Groat Road in Edmonton, Alberta, Canada. The newly installed plate girders of this bridge failed in the lateral-torsional buckling mode under wind and construction loads due to insufficient bracing. This was one of many similar incidents of steel bridge girder failure due to lateral-torsional buckling which occurred at the construction/deconstruction stages or during the service life (Thiébaud et al., 2016).

In addition to bending moment plate girders are also expected to carry shear forces. The web part of the plate girders carries the shear forces and shear buckling is therefore a critical failure mode for these structural members. Frequently the out-of-plane shear buckling resistance of plate girders is increased through the application of transverse stiffeners or corrugated webs. Therefore, in addition to the lateral -torsional buckling analysis, the design process of plate girders also involves the shear buckling of the structural member. Fig. 1 shows an example of shear buckling during experiments carried out by Mamazizi et al. (2013).

* *Corresponding author*. E-mail address: cakiroglu@tau.edu.tr (C. Cakiroglu)
ISSN: 2149-8024 / DOI: https://doi.org/10.20528/cjsmec.2020.04.003

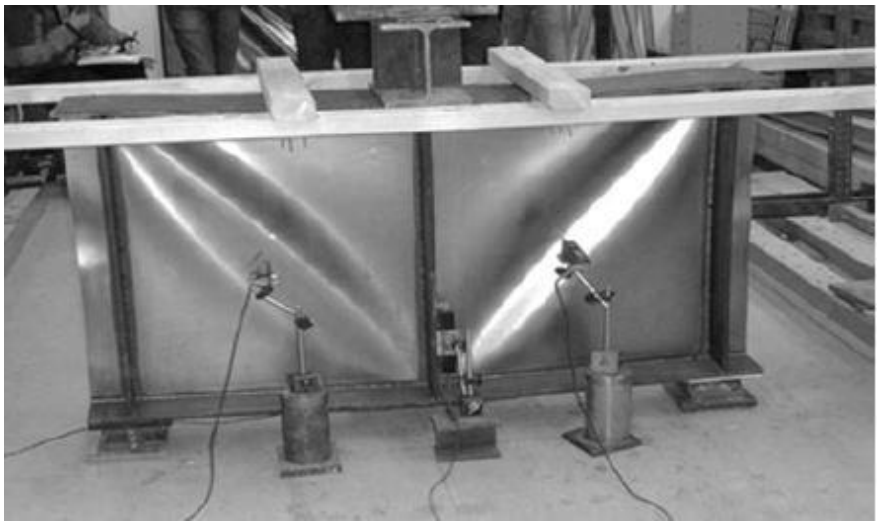

Fig. 1. Post-buckling deformation of stiffened plate girder under transverse loading (Mamazizi et al., 2013).

The design process of plate girders with the maximum load carrying capacity within cost and material constraints includes finding the optimal combination of plate thicknesses, web plate slenderness and stiffener spacing (Ziemian, 2010; Lee and Yoo, 1998; Gupta et al., 2006). While obtaining the plate girder profile that delivers the maximum structural performance with the minimum material usage is a challenging task the variation of the structural cost and performance with respect to flange and web slenderness values is not clear and can be at times counterintuitive. In order to gain a better understanding of these variations parametric studies of the buckling load and cross sectional area of a plate girder are carried out in this study. The main objective of this study is to clarify the impacts of changing the web plate slenderness, flange slenderness and the span-to-depth ratio of a plate girder on the structural performance. The critical buckling moment that leads to lateral torsional buckling and the ultimate shear stress are used as measures of structural performance.

1.1. Slenderness of girder plates

Plate girder components subject to flexure can be classified as compact, noncompact or slender according to their slenderness. Compact sections are those that have a small enough slenderness such that a local buckling of the compression flange or the web would not occur before the entire section reaches its yield strength and the section is able to attain its full plastic moment (Williams, 2011). The slenderness of a flange is quantified as $\lambda_f = b_f/2t_f$ where b_f and t_f are the width and the thickness of the flange respectively. Similarly, the slenderness of the web plate is quantified as $\lambda_w = D/t_w$ where D is the height of the plate girder excluding the flange thicknesses and t_w is the web plate thickness. In order to be classified as compact the flange and the web of a plate girder must satisfy the inequalities in Eqs. (1) and (2) respectively as per (AISC, 2016).

$$\lambda_f = \frac{b_f}{2t_f} \leq 0.38\sqrt{\frac{E}{\sigma_y}} \tag{1}$$

$$\lambda_w = \frac{D}{t_w} \leq 3.76\sqrt{\frac{E}{\sigma_y}} \tag{2}$$

In the above equations σ_y is the yield stress and E is the Young's modulus of steel. Noncompact structural members are those that are susceptible to local buckling before the section attains its full plastic moment. In order for the flange or the web of a plate girder to be classified as noncompact the slenderness values of these members must fall into the intervalls given in Eqs. (3) and (4) respectively (AISC, 2016).

$$0.38\sqrt{\frac{E}{\sigma_y}} < \lambda_f = \frac{b_f}{2t_f} < \sqrt{\frac{E}{\sigma_y}} \tag{3}$$

$$3.76\sqrt{\frac{E}{\sigma_y}} < \lambda_w = \frac{D}{t_w} < 5.70\sqrt{\frac{E}{\sigma_y}} \tag{4}$$

Slender sections are those that are susceptible to local buckling prior to reaching the yield stress anywhere on the section. In case of slender members, the slenderness parameter λ is greater than all limit values given in Eqs. (1) to (4). The classification of structural members with respect to their slenderness values is also visualized in Fig. 2.

1.2. Lateral-torsional buckling

Lateral Torsional Buckling (LTB) can be defined as a combination of lateral displacement and twisting due to the application of transverse forces on a beam type structure in the absence of sufficient lateral bracing (Kabir and Bhowmick, 2016). The research in the field of beam and plate girder buckling resulted in various equations for the prediction of the lateral torsional buckling load. The solutions available in the (AISC, 2016) and (CSA, 2009) codes for the prediction of the lateral torsional buckling capacity provide the buckling capacity for the case of uniform bending moment distribution together with a moment gradient factor C_b for the adjustment of the predicted capacities to the case of a non-uniform bending moment distribution. (Wong and Driver,

2010) developed Eq. (5) in order to incorporate the variation of the bending moment along unbraced sections of the plate girder into the buckling load capacity.

$$C_b = \frac{4M_{max}}{\sqrt{M_{max}^2+4M_A^2+7M_B^2+4M_C^2}} \leq 2.5 \quad (5)$$

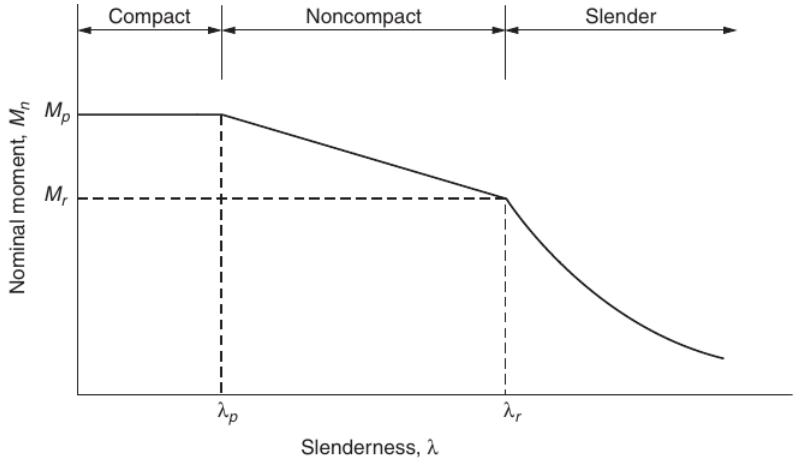

Fig. 2. Classification of structural members according to slenderness (Williams, 2011).

In Eq. (5) M_{max} is the absolute value of the maximum bending moment and M_A, M_B, M_C are the absolute values of the bending moments at a / 4, a / 2 and 3a / 4 length along the unbraced span of the plate girder respectively where a denotes the total length of the unbraced span. In this study the moment distribution between two stiffeners is assumed linear corresponding to an unbraced span of the girder beam shown in Fig. 1. Once C_b is known, the critical bending moment M_{cr} for lateral torsional buckling can be calculated using Eq. (6).

$$M_{cr} = C_b M_{0cr} \quad (6)$$

In Eq. (6), M_{0cr} is the critical bending moment of an unbraced span under uniform bending moment. The solution for M_{0cr} is given in Eq. (7) (Galambos and Surovek, 2008).

$$M_{0cr} = \frac{\pi}{a}\sqrt{EI_y\left(GJ + \frac{\pi^2 EC_w}{a^2}\right)} \quad (7)$$

In Eq. (7), G is the shear modulus, E is the modulus of elasticity, J is the St. Venant torsion constant, I_y is the moment of inertia with respect to the minor axis of the I-section and C_w is the warping constant.

1.3. Ultimate shear strength

The shear forces acting on girder plates are largely carried by the web plates. After the onset of local buckling of the web these steel plates under shear force are known to exhibit a significant amount of load carrying capacity in the post-buckling regime (Glassman and Moreyra Garlock, 2016). This structural behavior is thoroughly investigated in the literature and attributed to the existence of tensile stresses acting in the diagonal direction of the plates after the onset of shear buckling (Basler, 1961; White and Barker, 2008; Ziemian, 2010). These areas along the diagonal of the web plate where tensile stresses are acting can also be seen in Fig. 1. The research led to the development of various models for the prediction of the post-buckling shear capacity of web plates based on the concept of a tension field along the plate diagonal. "Tension field theory" is often used as a concept that includes all of these models. This theory is based on the observation that the stiffeners of a plate girder take up the compressive stresses resulting from the shear forces and the web plate resists buckling due to shear forces through tensile stresses forming along the plate diagonal (Wagner, 1931; Wilson, 1886). Among the models of the tension field theory the one which gained the most widespread acceptance in the research community is the model developed by (Basler, 1961) which is also included in (AISC, 2016).

Fig. 3 illustrates the concept of tension field on a web plate surrounded by flanges and transverse stiffeners. Here τ_u denotes the ultimate post buckling shear strength. The plate in Fig. 3 represents the unstiffened part of a plate girder web and it is assumed to be simply supported (SS) at all edges. An equation that predicts τ_u was first developed by (Basler, 1961) and later modified by (Fujii, 1968; Gaylord, 1963; Selberg, 1974) as given in Eq. (8).

$$\tau_u = \tau_{cr} + \sigma_y\left(1 - \frac{\tau_{cr}}{\tau_y}\right)\left(\frac{sin\theta_d}{2+cos\theta_d}\right) \quad (8)$$

Once τ_u is known, the ultimate postbuckling shear force V_u can be obtained through $V_u = \tau_u\, Dt_w$ where D is the depth of the plate as seen in Fig. 3 and t_w is the thickness of the web plate.

In Eq. (8), θ_d is the angle of the web panel diagonal. σ_y is the yield strength of the plate material from which the shear yield strength τ_y can be obtained through $\tau_y = 0.6\sigma_y$. The elastic shear buckling strength τ_{cr} in Eq. (8) is calculated through Eq. (9) (Timoshenko, 2009).

$$\tau_{cr} = \frac{k\pi^2 E}{12(1-\nu^2)\left(\frac{D}{t_w}\right)^2} \quad (9)$$

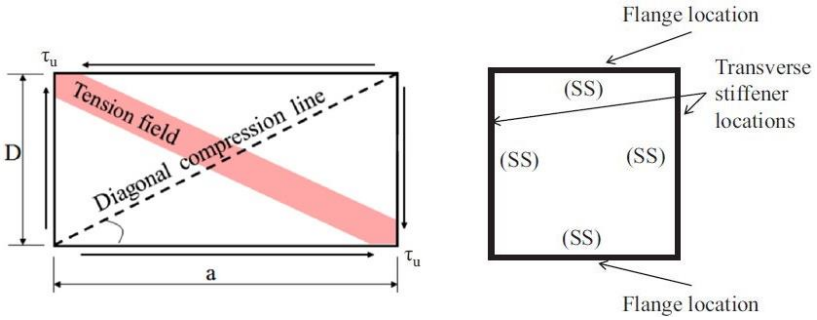

Fig. 3. Schematic of Basler's tension field theory (Glassman and Moreyra Garlock, 2016).

In Eq. (9), E is the modulus of elasticity, ν is the Poisson's ratio, $D\ /\ t_w$ is the slenderness ratio and k is the shear buckling coefficient which can be calculated as a function of $a\ /\ D$(span-to-depth ratio) and the assumed boundary conditions of the web plate. The equation for k is given in Eq. (10) for simply supported boundary conditions where a is the clear distance between transverse stiffeners (AISC, 2016).

$$k = 5.0 + \frac{5.0}{(a/D)^2} \tag{10}$$

2. Methodology and Results

Even though the lateral-torsional buckling load and the ultimate shear strength of plate girders can be predicted for given profile dimensions reliably, the dimensioning of a profile for the best combination of economic design and structural performance often necessitates the application of optimization procedures (Bekdaş and Nigdeli, 2013). Due to the computational overhead that many optimization techniques entail this dimensioning is often done in practice through trial and error. In this process it is crucial to have an intuition about the effect of slenderness of the web and the flange on the structural performance. However, from Eqs. (5) to (8) the variation of M_{cr} and τ_u with respect to the slenderness values of the web and the flange cannot be easily discerned. In order to gain a better understanding of the relationship between slenderness and structural performance, a parametric study of the slenderness is carried out in this study. As the base model the girder plate tested by (Mamazizi et al., 2013) is used. The material properties and dimensions of this model are given in Table 1. In this table f_{yf} and f_{yw} denote the yield strengths of the flange and the web respectively. The parametric study resulted in 917826 different combinations of the web thickness, web plate depth, flange thickness, flange width and corresponding critical LTB moment and ultimate shear strength values. The analysis was carried out using a custom program developed in the Python programming language. The parameter ranges of the parametric study are selected in such a way that they are in the same order of magnitude as the plate girder dimensions listed in Table 1. The upper and lower bounds of these parameters are determined as listed in Table 2 considering fabrication constraints such that web plate thicknesses less than 2mm are not included in the parametric study.

Table 1. The geometric and material properties used in the experimental study (Mamazizi et al., 2013).

$t_f\ [mm]$	$b_f\ [mm]$	$t_w\ [mm]$	$D\ [mm]$	$a\ [mm]$	$f_{yf}\ [MPa]$	$f_{yw}\ [MPa]$
15	250	2	800	750	235	210

Table 2. Parameter ranges and increment sizes used in the parametric study.

	$t_f\ [mm]$	$t_w\ [mm]$	$b_f\ [mm]$	$D\ [mm]$
Upper bound	30	10	350	1200
Lower bound	5	2	150	400
Increment size	1	0.2	10	20

2.1. Effects of slenderness on the lateral-torsional buckling load

Even though the critical buckling moment can be computed using Eqs. (5) to (7), it is hard for the practicing engineer to develop an intuition about how the flange and web slenderness ratios effect the lateral-torsional buckling moment from these equations. To clarify these effects, M_{cr} has been calculated using Eqs. (5) to (7) and its variation has been plotted with respect to λ_f. Fig. 4 shows this variation for five different values of λ_w. Fig. 4 shows that increasing the flange slenderness has a favorable effect on the critical moment for all values of the web slenderness. Furthermore, this favorable effect becomes more pronounced as the web slenderness increases.

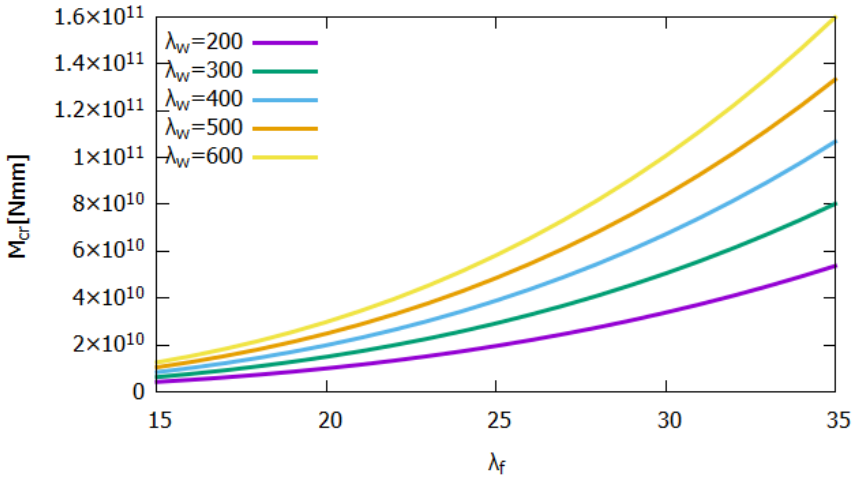

Fig. 4. Variation of the critical bending moment with respect to flange slenderness.

Fig. 5 shows that a similar variation of the critical moment can also be observed with respect to the web slenderness. Also, the rate of increase of M_{cr} seems to be proportional to the flange slenderness. The major difference between the two variations in Fig. 4 and Fig. 5 is that M_{cr} has a nonlinear variation with respect to λ_f and a linear variation with respect to λ_w. A combination of the effects of λ_f and λ_w on M_{cr} can be seen in Fig. 6.

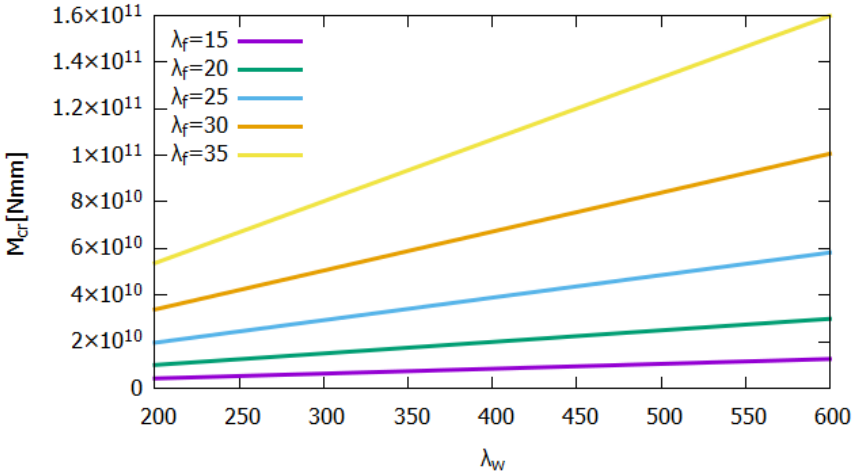

Fig. 5. Variation of the critical bending moment with respect to web slenderness.

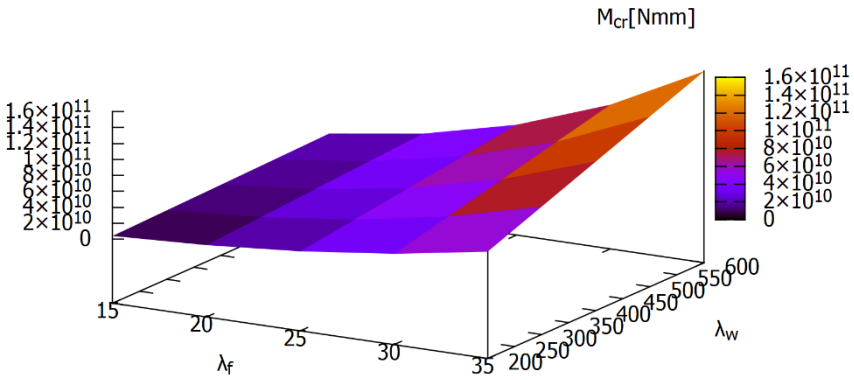

Fig. 6. Variation of the critical buckling moment with respect to the flange and web slenderness ratios.

2.2. Effects of slenderness on the ultimate shear strength

From Eqs.(8) to (10) the parameters that τ_u depends on can be summarized in function format as in Eq. (11).

$$\tau_u = f(\theta_d, \sigma_y, 4\,\lambda_w, \nu, E) \tag{11}$$

From these five parameters σ_y, ν and E are material constants and the effect of the remaining two design variables are investigated in this study. According to Eqs.

(8) and (9) the flange slenderness has no effect on the ultimate shear strength. Therefore, the variation of τ_u with respect to the web slenderness is the same for any flange slenderness. This variation can be seen in Fig. 7 for $\lambda_f = 15$ while this variation is independent of the value that λ_f takes. From Fig. 7 it can be observed that the effect of web slenderness on τ_u is directly related to the web plate thickness. For relatively small values of t_w such as 2mm or 3mm, increasing the web slenderness seems to have a favorable effect on the ultimate shear strength. On the other hand, for greater values of the web plate thickness, increasing the web plate slenderness has the opposite effect on τ_u.

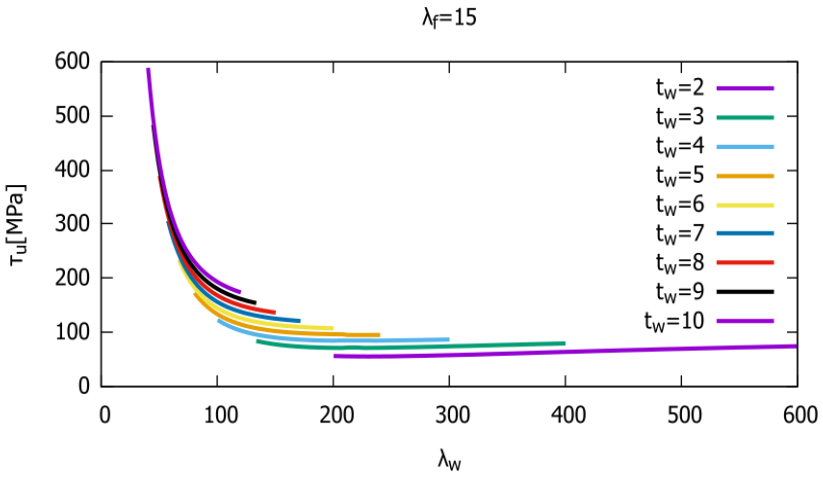

Fig. 7. Variation of τ_u with respect to web plate slenderness.

2.3. Effects of plate diagonal angle on the ultimate shear strength

The effect of the angle θ_d that appears in Eq. (8) is visualized in Figs. 8 and 9. Since this angle is a function of the span-to-depth ratio (a/D), understanding the dependence of τ_u on θ_d also gives insights about the relationship between τ_u and the a/D ratio. According to (Williams, 2011), the a/D ratio is recommended to be in the range from 10 to 12 which corresponds to a range from 4.76° to 5.71° for θ_d. The variation of τ_u for the recommended range of θ_d is plotted in Fig. 8 for five different web plate thicknesses. For all of these t_w values increasing θ_d seems to have an adverse effect on τ_u. Increasing the value of t_w leads to greater ultimate shear stresses as expected.

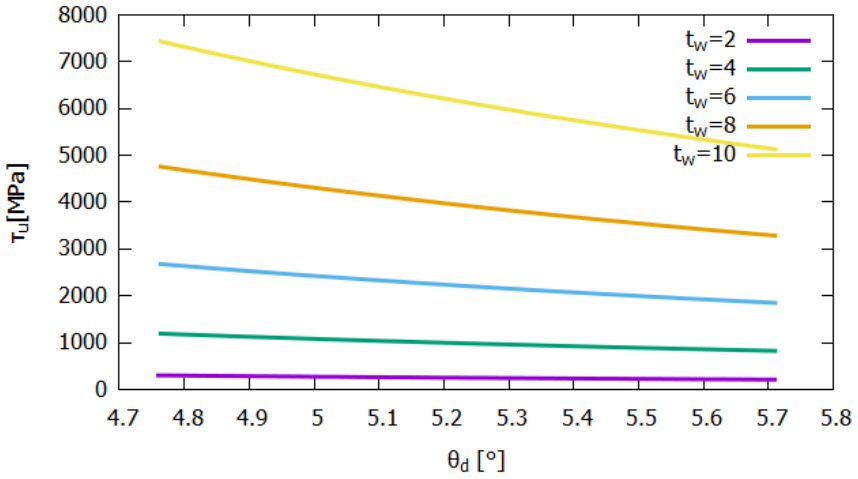

Fig. 8. The variation of τ_u with respect to θ_d in the recommended range for θ_d.

In order to better understand the variation of τ_u for a wider range of θ_d, Figure 9 was plotted for θ_d values up to 45°. From Fig. 9 it can be seen that the effect of θ_d on τ_u is most significant for angles less than about 20°. Overall increasing θ_d has an adverse effect on the ultimate shear strength even though this effect becomes negligible for angles close to 45°.

3. Conclusions

The (AISC, 2016) and (CSA, 2009) codes include equations for the prediction of the critical buckling load and the ultimate shear stress of plate girders. However due to the formulation of these equations it is not easy to identify the effect of slenderness and span-to-depth ratio

on the structural performance even though the information about the effect of these parameters is indirectly included in these equations. The aim of this study is to clarify the effect of these geometric variables on the structural performance. To this end, a parametric study was carried out that calculated the critical buckling load and the ultimate shear stress for a wide range of web and flange slenderness as well as span-to-depth ratio values. As a result, increasing both the flange and the web slenderness ratios were found to have a favorable effect on the critical buckling moment. The effect of the web plate slenderness on the ultimate shear stress was also investigated. The visualization of the results showed that the effect of the web plate slenderness on the ultimate shear stress depends on the web plate thickness. For small web plate thicknesses an increase in web plate slenderness is observed to be favorable whereas for larger thicknesses increasing the web plate slenderness adversely affects the ultimate shear strength. Finally, the effect of the plate diagonal angle on the ultimate shear stress was visualized and this variable was found to have a significant effect on the structural performance only for angle values less than about 25°. Also, this variable is observed to have a greater effect on the structural performance for larger web plate thicknesses.

This study was concerned with the sensitivity of the structural performance to changing cross sectional properties of plate girders related to slenderness and span-to-depth ratio. Knowing the effect these parameters have on the structural performance can be a great advantage for practicing design engineers. In the absence of clearly documented information about the relationship between geometric properties such as slenderness and the structural performance more sophisticated optimization techniques need to be used in the structural dimensioning process. Further research in this field can be carried out to investigate the effect of material properties such as yield stress and elasticity modulus as well as other cross-sectional properties such as the warping constant and the St. Venant torsion constant on the structural performance.

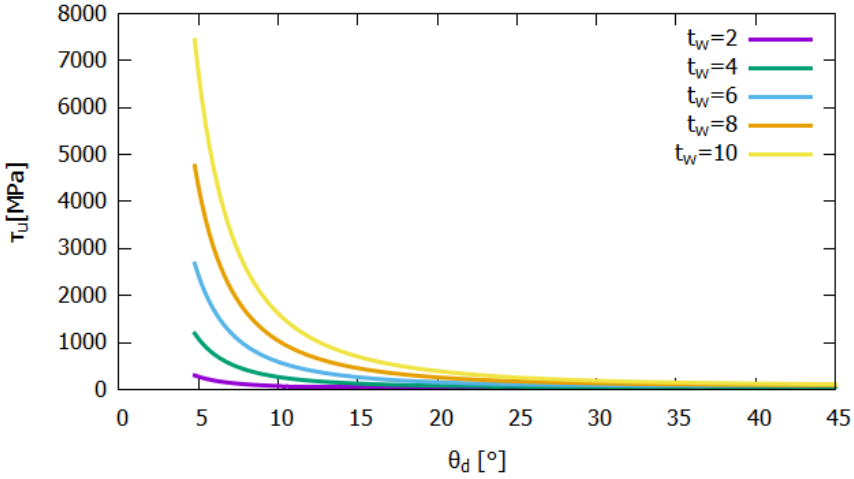

Fig. 9. The variation of τ_u with respect to θ_d.

Appendix

Torsional section properties of a doubly symmetric I-section (Kulak and Grondin, 2002).

St. Venant's torsion constant:

$$J = \frac{2b_f t_f^3 + (D+t_f)t_w^3}{3}$$

Warping constant:

$$C_w = \frac{(D+t_f)^2 b_f^3 t_f}{24}$$

References

ANSI/AISC 360-16 (2016). Specification for Structural Steel Buildings. American Institute of Steel Construction, Chicago, USA.

Basler K (1961). Strength of plate girders in shear. *Journal of Structural Division,* 87, 151–180.

Bekdas G, Nigdeli SM (2013). Optimization of tuned mass damper with harmony search. *Metaheuristic Applications in Structures and Infrastructures*, 345–371.

CSA (2009). Design of Steel Structures S16-09, Canadian Standards Association, Mississauga, Canada.

Edmonton Talks News (2016). https://edmonton.talks.news/groat-road-bridge. Downloaded on 02-24-2020.

Fujii T (1968). On an improved theory for Dr. Basler's theory. *8th Congress of International Association for Bridge and Structural Engineering (IABSE)*, New York, USA, 479–487.

Fukumoto Y, Kubo M, Itoh Y (1980). Strength variation of laterally unsupported beams. *Journal of Structural Division*, ASCE 106(ST1), 165–181.

Galambos TV, Surovek AE (2008). Structural Stability of Steel: Concepts and Applications for Structural Engineers. Wiley Online Library, USA.

Gaylord EH (1963). Discussion of K. Basler Strength of Plate Girders in Shear. *Transactions of ASCE*, 128, 712.

Glassman JD, Moreyra Garlock ME (2016). A compression model for ultimate postbuckling shear strength. *Thin-Walled Structures*, 102, 258–272.

Gupta VK, Okui Y, Nagai M (2006). Development of web slenderness limits for composite I-girders accounting for initial bending moment. *Doboku Gakkai Ronbunshuu A*, 62, 854–864.

Kabir M, Bhowmick A (2016). Lateral torsional buckling of welded wide flange beams. *Structural Stability Research Council Annual Stability Conference*, Orlando, USA, 39–52.

Kulak GL, Grondin GY (2002). Limit States Design in Structural Steel. Canadian Institute of Steel Construction, Canada.

Lee SC, Yoo CH (1998). Strength of plate girder web panels under pure shear. *Journal of Structural Engineering*, 124, 184–194.

MacPhedran I, Grondin G (2011). A proposed simplified Canadian beam design. *Canadian Journal of Civil Engineering*, 38, 141–143.

Mamazizi S, Crocetti R, Mehri H (2013). Numerical and experimental investigation on the post-buckling behavior of steel plate girders subjected to shear. *Proceedings of the Annual Stability Conference Structural Stability Research Council*, St. Louis, MI, USA, 16–20.

Nethercot D (1974). Buckling of welded beams and girders. *IABSE Publications*, 34, 107-121.

Selberg A (1974). On the shear capacity of girder webs, *International Association for Bridge and Structural Engineering Publications*, 34, 145–155.

Thiébaud R, Lebet JP, Beyer A, Boissonnade N (2016). Lateral torsional buckling of steel bridge girders. *Proceedings of the Annual Stability Conference Structural Stability Research Council,* Orlando, USA, 12–15.

Timoshenko SP, Gere JM (2009). Theory of Elastic Stability. Courier Corporation, North Chelmsford, MA, USA.

Wagner H (1931). Flat sheet metal girders with very thin metal web. Part II: Sheet metal girders with spars resistant to bending-oblique uprights-stiffness. *NASA Technical Report*, USA.

White DW, Barker MG (2008). Shear resistance of transversely stiffened steel I-girders. *Journal of Structural Engineering*, 134, 1425–1436.

Williams A (2011). Steel Structures Design ASD/LRFD. McGraw-Hill, USA.

Wilson JM (1886). On specifications for strength of iron bridges. *Transactions of the American Society of Civil Engineers*, 15, 389–414.

Wong E, Driver RG (2010). Critical evaluation of equivalent moment factor procedures for laterally unsupported beams. *Engineering Journal*, 47(1), 1–20.

Ziemian RD (2010). Guide to Stability Design Criteria for Metal Structures. John Wiley & Sons, USA.

Challenge Journal of Structural Mechanics

Research Article

Seismic risk priorities of site and mid-rise RC buildings in Turkey

Ercan Işık [a,*], İbrahim Baran Karaşin [b], Alper Demirci [c], Aydın Büyüksaraç [d]

[a] *Department of Civil Engineering, Bitlis Eren University, 13100 Bitlis, Turkey*
[b] *Department of Civil Engineering, Dicle University, 21100 Diyarbakır, Turkey*
[c] *Department of Geophysical Engineering, Çanakkale Onsekiz Mart University, 17100 Çanakkale, Turkey*
[d] *Çan Vocational School, Çanakkale Onsekiz Mart University, 17100 Çanakkale, Turkey*

ABSTRACT

Especially, the large-scale loss of life and property caused by the significant earthquakes in recent years has brought the importance of research and measures to be taken on this issue. Determining and analysing the ever-increasing building stock of the cities and detecting and managing all information related to buildings are important in terms of spatial planning and urban transformation. This study aims to determine tectonic characteristics calculating a and b values of Gutenberg- Richter magnitude-frequency relation which forms the basis of earthquake statistics for all cities in Turkey and the reinforced-concrete buildings which are primarily risky in terms of urban transformation. For this purpose, a total of 1620, 5-storey buildings from all provinces of Turkey were assessed. Twenty reinforced concrete buildings from each province were taken into consideration which has 5-stories. The first stage evaluation method specified in the principles regarding the identification of risky buildings issued in 2013 by the Republic of Turkey, Ministry of Environment and Urbanization was used in this study. The performance scores for 1620 buildings were calculated by using this method. A risk priority map was created for the provinces, taking into account for these buildings. The study aims to determine risk priorities of site and mid-rise reinforced-concrete buildings among the cities. The results obtained were interpreted and recommendations were made.

ARTICLE INFO

Article history:
Received 1 July 2020
Revised 14 September 2020
Accepted 28 September 2020

Keywords:
Rapid assessment
Turkey
Risk priority
Seismic risk
Site
Building

1. Introduction

The first step in protecting a settlement from an earthquake disaster is to have theoretical predictions of the consequences such as socio-economic losses and structural damage that may occur after an earthquake. This is very important in terms of preparation for disaster management (Hadzima-Nyarko et al., 2016; Harirchian et al., 2020). Earthquakes occur frequently in Turkey due to the active seismic zones, and many reinforced-concrete (RC) buildings are damaged as a result of these earthquakes.

It is almost impossible to determine the seismic safety of existing RC buildings before a possible earthquake. The main purpose of the determination of seismic safety of buildings is to ensure making right decisions about the existing building stock by making necessary examinations and calculations before a possible earthquake. A large amount of existing building stock makes it difficult to evaluate buildings in a reasonable time due to the lack of adequate qualified personnel and economic perspectives. Even the detailed examination of seismic safety verification of an ordinary building continues for days. Therefore, it is not possible to examine every existing building in detail. In this context, accurate results can be achieved by using methods that will give faster and more accurate results (Işık, 2016). These methods are generally called the first stage evaluation methods. The buildings with risk priority can be determined using these methods. This will greatly reduce the number of buildings to be subjected to detailed analysis (Işık, 2015).

* *Corresponding author*. Tel.: +90-434-228-0030 ; Fax: +90-434-222-9101 ; E-mail address: eisik@beu.edu.tr (E. Işık)
ISSN: 2149-8024 / DOI: https://doi.org/10.20528/cjsmec.2020.04.004

There are various methods in the literature regarding the rapid evaluation of structures. Detailed information and analysis are not required in such rapid evaluation methods. There are many case studies on the use of these methods (FEMA-154, 2002; Japan Seismic Index–Ohkubo, 1991; NRCC, 1993; Šipoš et al., 2017; Kepekci and Ozcep, 2011; Hadzima-Nyarko et al., 2018; Villacis et al., 2000; Yakut, 2004; Benavent-Climent, 2011; Foo and Davenport, 2003; Jain et al., 2010; Sucuoğlu, 2007; Sinha and Goyal, 2004; İlki et al., 2014; Bal et al., 2008; Albayrak et al., 2015; Yakut et al., 2014; Arslan et al., 2010). The first stage evaluation method specified in the principles regarding the identification of risky buildings issued in 2013 by the Republic of Turkey, Ministry of Environment and Urbanization was used in this study (DRBB, 2013). A total of 1620 buildings including twenty RC buildings which are 5-storey from each of 81 provinces in Turkey were assessed in this study. Each performance score of these buildings was calculated using this method, and thus their risk priorities were determined.

The Gutenberg-Richter (1944) relation is currently used as a measure of earthquake efficiency based on the magnitude-frequency distribution. Obtaining this relationship for the whole of Turkey, it led to the production of basic information about the earthquake hazard. The "*a*" parameter in the magnitude-frequency relation changes depending on the observation period, the size of the study area and the level of earthquake activity. It is also defined as the average annual seismic activity index. The parameter "*b*" is an important parameter in the statistical analysis of earthquakes and gives the slope of the linear relationship. It is related to the deformation of rocks and thus the physics of earthquake occurrence. The "*b*" value is an indicator of seismic activity and varies from region to region. Normally, a small *b* value is associated with a high stress drop and a large *b* value is associated with a low stress drop. It was observed that the "*b*" value decreased before the earthquake (Anadolu and Kalyoncuoglu, 2010).

The study firstly presented the information about the rapid evaluation methods, mentioned about the reasons for the emergence of these methods and then provided information about Turkey's tectonic settings and seismicity. The seismicity parameters *a* and *b* were obtained for each province. The return periods for each province have been calculated for the probability of exceeding 10% in the earthquake regulation. This study also presented information about the rapid evaluation method used in this study and explained how this method is applied step by step. The method recommended by the Ministry of Environment and Urbanization in 2013 was used as the first stage assessment method in this study. Since this method includes calculations according to the 2007 earthquake regulation, this regulation was also taken into account within the scope of the study. A mapping procedure was applied for the site and RC buildings examined in this study considering their geometrical locations. The images of some of the examined buildings were included in the study. The distribution of the negativity parameters in the mid-rise RC buildings examined in the study was determined and the performance score for each building was calculated. It was tried to determine the risk priority among provinces by using the obtained results for site and mid-rise buildings. The results obtained were interpreted and suggestions were made in line with the results. This work from both seismicity as well as structural covers all provinces in Turkey. Considering the whole country rather than the regional basis adds a special importance to this study.

2. Tectonic Settings and Seismicity in Turkey

Turkey, as a part of Alpine-Himalayan orogenic belt, has tectonic progresses under the complex geodynamic effects of the relative motions of the Arabian, African and Eurasian plates. The majortectonic units, shaping the earthquake distribution in Turkey, are the North Anatolian Fault Zone (NAFZ), the East Anatolian and North-East Anatolian Fault Zones (EAFZ-NEAFZ), West Anatolian Extensional Province (WAEP) including a considerable amount of horst and graben structures bounded by normal faults, the subduction zones (Hellenic and Cyprus) (Reilinger et al., 2006) and the East Anatolian Collision Zone (EACZ) (Fig. 1). The North Anatolian Fault Zone (NAFZ) with an approximately 1600 km long is a right-lateral fault caused hazardous earthquakes and runs from Karlıova (Bingöl) triple junction through North Anatolia to the Marmara Sea. It produced a sequence of earthquakes having magnitudes greater than 7.0 (Mw) (Ateş et al., 2003, 2008, 2009, 2012; Bayrak et al., 2011). The East Anatolian Fault Zone (EAFZ) is also another major tectonic unit as a plate boundary with 500 km length between the Arabian and Anatolian plates. It starts from Gulf of Iskenderun and converges with NAFZ on the Karlıova triple junction. Although not as large as on the NAFZ, many major earthquakes are known to have occurred in or near EAFZ within the historical and instrumental period (Taymaz et al., 1991). WAEP, having the highest geothermal potential in Turkey, is one of the most seismically active and rapidly extending regions of the world (>30 mm/y) (Bozkurt, 2001). As a result of this extension, considerable number of large earthquakes occurs on the boundaries of horst and graben structures. As a result, Turkey can be considered as one of the most important tectonic laboratories in the world. There have been significant losses of life and property, due to earthquake damages in Turkey (Arslan et al., 2013; İnel et al., 2008; Bilgin, 2016; Bilgin and Uruçi, 2018; Utkucu et al., 2013).

After the significant contribution of the earthquake magnitude concept made by C. Richter in 1935, it was revealed that the earthquakes were not evenly distributed in time, space and size. The distribution of the earthquakes by size shows the scale invariance. This emphasizes that there is no characteristic size of the event (the theoretical limits in the maximum earthquake size). An experimental correlation defines the distribution of the earthquakes according to Ishimoto and Lida (1939) in the east and Gutenberg-Richter (1944) in the west (Eq. 1).

$$\log N = a - bM \tag{1}$$

where *a* and *b* are positive real constants for a given region and time interval, *N* number of earthquakes with magnitude *M* is given. *a*-value explains the seismic activity. It is determined by the event rate and depends on the selected region and time window. Typically, the *b*-value, which is close to 1, is a tectonic parameter that defines the relative multiplicity from large to small shocks. It is seen that the seismic environment represents the properties of the seismic environment in such a way as to the tension and/or material conditions. Eq. (1) is often referred to as the Gutenberg-Richter (G-R) magnitude-frequency relationship.

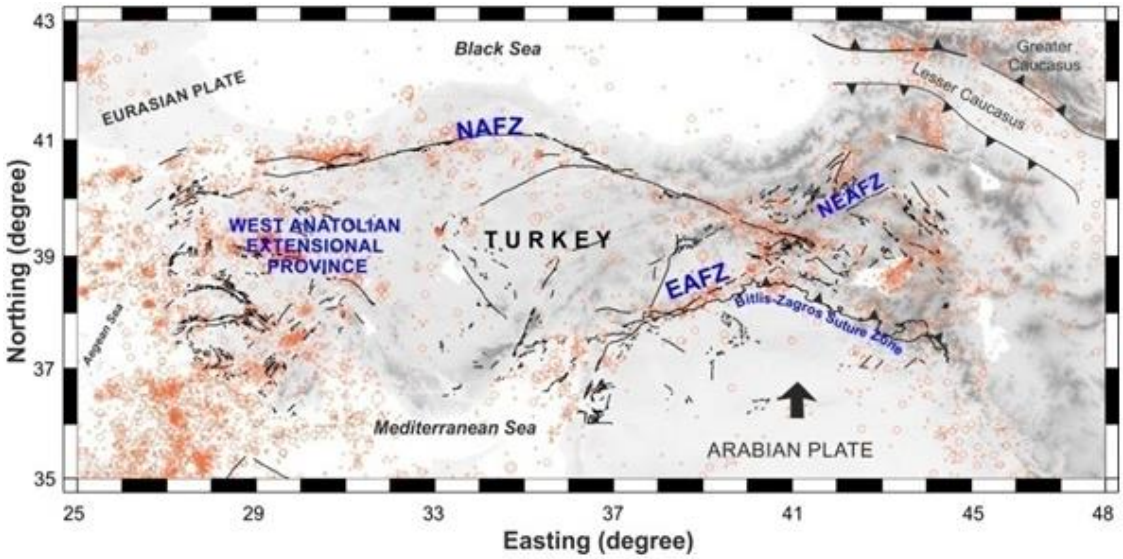

Fig. 1. Significant tectonic structures and earthquake activity (*M*>4) in Turkey during the instrumental period (Kalafat et al., 2011).

The space and temporal changes of the *b*-value have been previously used in a number of several seismicity studies. After the pioneering work of Mogi (1962), Scholz (1968) and Wyss (1973), the volumes of the active magmatic chambers (Wiemer and Benoit, 1996; Wiemer et al., 1998) by many investigators, and the origins of regional volcanism (Monterroso and Kulhanek, 2003) was widely used for identifying and estimating major tectonic earthquakes (Monterroso, 2003; Nuannin et al., 2005). The *b*-value studies on seismicity were carried out with the results published in many scientific articles in the last 25 years (Aki, 1965; Bender, 1983; Cao and Gao, 2002; Murru et al., 2007; Kalyoncuoglu, 2007; Farrell et al., 2009; Anadolu and Kalyoncuoglu, 2010; Kalyoncuoglu et al., 2013; Roberts et al., 2015). For small and $M \geq 7.3$ earthquakes, the frequency decreases faster than linearity, and in some cases, there may be a better approximation of the observed data. There are two explanations for deviations from linearity.

In minor earthquakes; there is a lack of data for years, especially in catalogues. However, recent studies have shown that the reduction of *b*-value below the threshold size is not only due to a lack of catalogues, but those small earthquakes are not counted as much as a fixed *b*-value predicted from major events and that the decrease in frequency may therefore be a certain extent real. In major earthquakes; saturation of the size scales; in other words, the problem with the method in which the magnitudes were measured. Another reason is the length of existing catalogues (usually very short) with large earthquakes missing. In general, repetition times beyond the time interval (catalogue) of data should be considered carefully. There are several acceptable explanations for the observed changes in *b*-values. High and low voltages lead to low and high *b*-value earthquake series (Scholz, 1968; Wyss, 1973). This observation is used to determine the structural anomalies and voltage levels in the crust and/or upper mantle in determining the prediction of earthquakes and determination of the volume of active chambers (Wiemer and Benoit, 1996; Wiemer et al., 1998).

Large heterogeneities correspond to higher *b*-values. Laboratory experiments have shown that heat changes result in an increase in *b*-value from 1.2 to 2.7 (Warren and Latham, 1970). The *b*-value of aftershocks is high, whereas the *b*-value of the leading earthquakes is low (Suyehiro et al., 1964). For example, in 1975, the *b*-value of Haicheng pioneering earthquake series was found to be 0.6. The *b*-value of the aftershocks was 0.9.

Earthquake storms come to the conditions where the *b*-value is greater than 1. Sometimes the *b*-value is greater than 2.5, meaning that large earthquakes occur later. Storms are often associated with volcanic activity. In volcanic regions, faults do not only create large earthquakes, but continuous stresses are largely heterogeneous. Swarms are caused by processes such as the lack of a clear mainstream shock and the migration of magmatic fluids or caldera development.

In summary, there is an inverse relationship between the size of the calculated *b*-value and the level of tension accumulation. Thus, it can serve as an approximation parameter to predict large earthquakes. In this study, *a* and *b* values are calculated using Gutenberg-Richter's (1944) equation for all cities in Turkey. Calculated values were presented city by city in the map of Turkey (Figs. 2 and 3).

When these maps are examined, regional similarities are observed in the *a*-value distribution map in Fig. 2 and continuity can be defined in areas with near tectonic features. In contrast, the *b*-value distribution map in Fig. 3 shows no tectonic identification that can be associated with each other in the nearby settlements. This may be due to province limitations in the database being used. However, if the selected cities are divided into geographic or tectonic regions, a different picture is encountered.

In this study, the risk map of provinces is shown in Fig. 4 if the probability of exceeding within a period of 50 years is 10%.

While all these calculations were performed, a 100 km wide zone was considered for each province and the earthquakes of $M \geq 3$ in this region were taken into consideration. Calculations were made by using the Seismic Hazard and Risk Analysis Program (Alan, 2016).

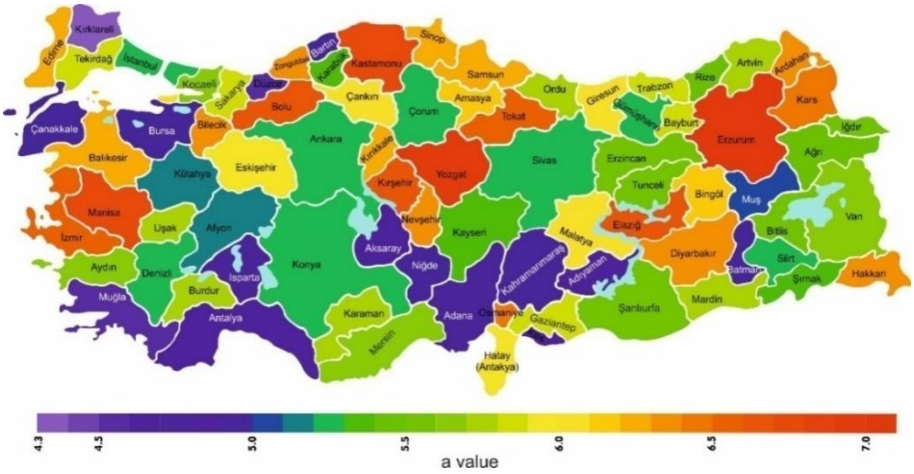

Fig. 2. Distribution map of *a*-value.

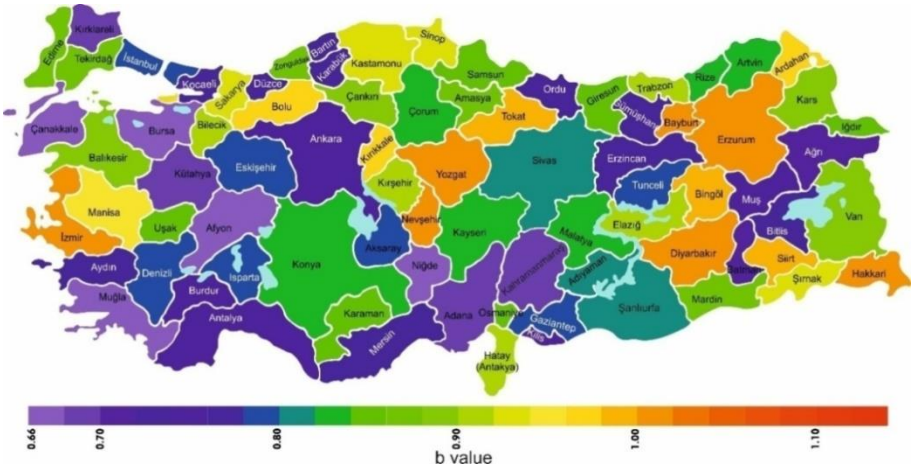

Fig. 3. Distribution map of *b*-value.

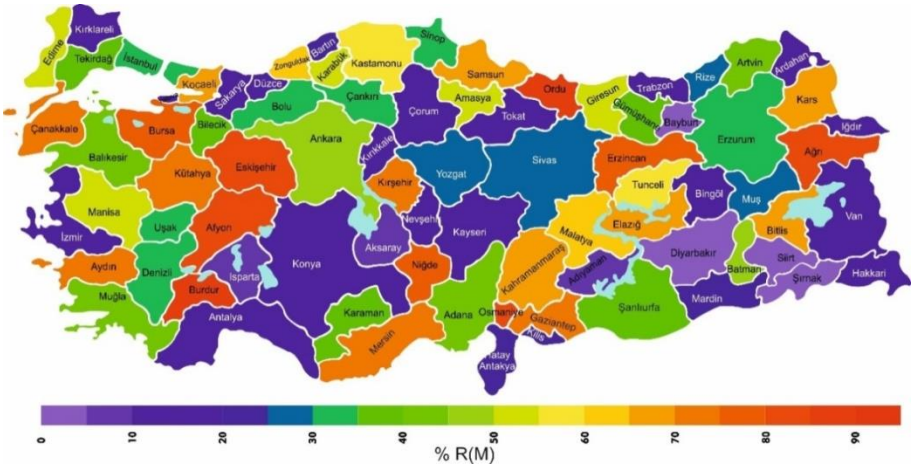

Fig. 4. Risk map for earthquakes with a probability of exceedance over 50 years.

3. Earthquake Risk Priorities of Existing Mid-rise RC Buildings in Turkey

It is a well-known fact that structural damage varies according to structural properties. The nature and amount of structural damage depend on the nature of the loads acting on the structures and the quality of the materials that compose the structural and non-structural elements, on the type and configuration of structural systems (Aksoylu et al., 2016; Hadzima-Nyarko et al., 2011). However, identifying these properties can be achieved pursuant to the evaluation of the data obtained as a result of classifying them. In this context, it is important to identify risky buildings. It cannot be said that buildings with low risk are in compliance with seismic design code. As mentioned above, this is only the first stage evaluation. Therefore, definite results will only be produced as a result of using definite detailed analysis methods. This method is only aimed at determining the priority of the buildings to be examined in the second stage evaluation method (Işık, 2013).

Reducing the weaknesses of the building stock is an important step towards reducing seismic risk. Large scale evaluation methods are popular for the evaluation of building stock, although they are expensive and not easy to use (Chever, 2012). Another effective way to assess the seismic vulnerability of existing buildings is to make an urban and regional emergency response and earthquake protection and remediation plans to protect human life and the economy (Ahmed et al., 2014; Bilgin and Frangu, 2017). During the seismic risk assessment of RC buildings, seismic hazard and building sensitivity should be considered (Tesfamariam and Liu, 2010; Jain et al., 2010; Özcebe, 2004). Seismic scanning methods are designed as rough scan procedures using fewer resources per building (Tischer et al., 2011; Tischer et al., 2012).

A period of high residential building demand during the 1980's due to high population growth and migration from rural areas to the urban areas has caused non-engineered or low construction quality structures. As a result, major portion of Turkey's existing building stock is susceptible to earthquake-induced damage despite its high earthquake threat (Inel and Meral, 2016).

Taking into account the amount of building stock in Turkey, it is important to correctly know buildings' parametric data and to be able to access these data easily and quickly. The purpose of rapid screening methods is to determine the building's risk priorities and to make the right decisions for them. The building performance scores are calculated using these methods which enable to collect values for the parameters provided by methods without entering the building or partially entering the building, and then the building's risk priority can be decided as a result of comparing these values. The first-stage evaluation methods taking into account of building properties and earthquake hazard can be used to determine the risk priorities and regional distribution of the buildings which may be at risk in certain areas under the law issued by Republic of Turkey Ministry of Environment and Urbanization (DRBB, 2013). This method was revised in 2019, according to the earthquake regulation updated in 2018. This method was carried out by a commission created by experts in the field. In general, the factors weakening the building defence mechanism are considered in these methods. Short column, soft/weak story, vertical discontinuity, lateral discontinuity, year of construction, visible building quality and hill-slope effect are some of these negative parameters (DRBB, 2013; NRCC, 1993; Kaminosono, 1992; Okada, 1999; Gülay et al., 2010; Işık, 2016; Bayraktar et al., 2013; Inel, 2016; Işık and Kutanis, 2015; Srikanth et al., 2014; Alam et al., 2012; Sucuoğlu, 2007;Eleftheriadou and Karabinis, 2012; Mirshaiei et al., 2017; Zülfikar et al., 2017; Özmen and Inel, 2017; Işık et al., 2017; Scawthorn, 1986; Işık et al., 2018; Shehu et al., 2019).

This method can be used for RC buildings which vary between 1 to 7 storeys. The parameters which are required for the use of this method are given below:

- Structural system type
- Number of story
- Current situation and visual quality
- Soft /weak story
- Vertical irregularity
- Heavy overhangs
- Irregularity in plan / torsion
- Short column
- Building regulation / pounding
- Hillside effect
- Seismicity and soil type

A data collection report is created for each RC building to evaluate the reinforced concrete buildings under earthquake risk. This form is shown in Table 1. The data was collected for each building according to Table 1 and then these data are subjected to evaluation.

Table 1. Inputs of the building examined.

District	Vertical irregularity
Neighbourhood	Irregularity in plan/torsion
Street	Building regulation/pounding
Door No.	Soft/weak storey
Block	Heavy overhangs
Parcel	Short column
Latitude	Hillside effect
Longitude	Structural system type
Seismicity of the region	Number of storey
Year of Construction	Soil type

The geometric location distribution of the buildings which is subject to this study is shown in Fig. 5.

When conducting building evaluations, the primary issues to determine are seismicity of the area and the seismic risk zone of the building according to its soil type. Earthquake area and the seismic risk zones according to soil types are given in Table 2.

The map of earthquake zones which were considered in this study is shown in Fig. 6. Soil types were determined for each city, and the references in the literature and the data obtained from relevant institutions and organizations were taken into consideration (Tabban, 2000).

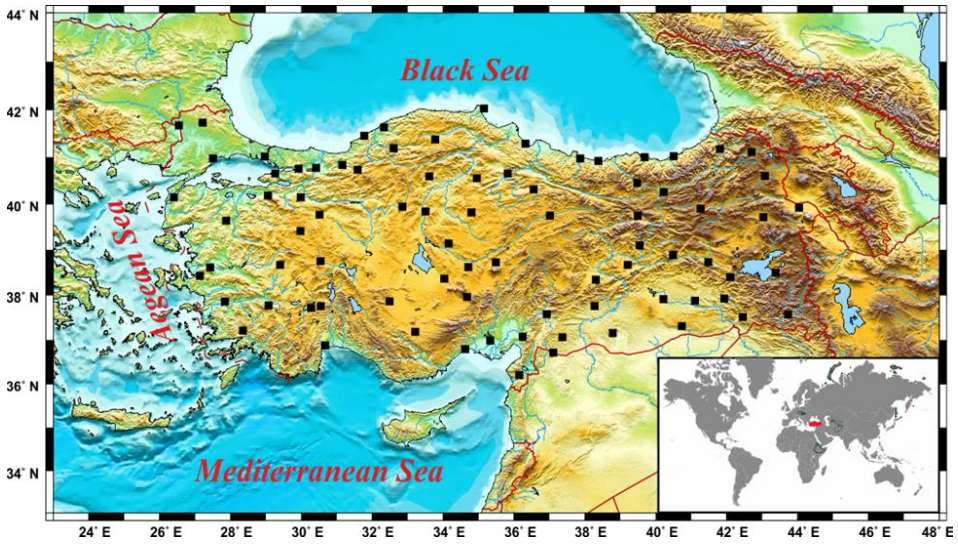

Fig. 5. Location distribution map of the buildings analyzed.

Table 2. Earthquake areas determined according to TEC-2007

Seismic risk zone	Earthquake area according to TEC-2007	Soil types according to TEC-2007
I	1	Z3/Z4
II	1	Z1/Z2
	2	Z3/Z4
III	2	Z1/Z2
	3	Z3/Z4
IV	3	Z1/Z2
	4	All soil types

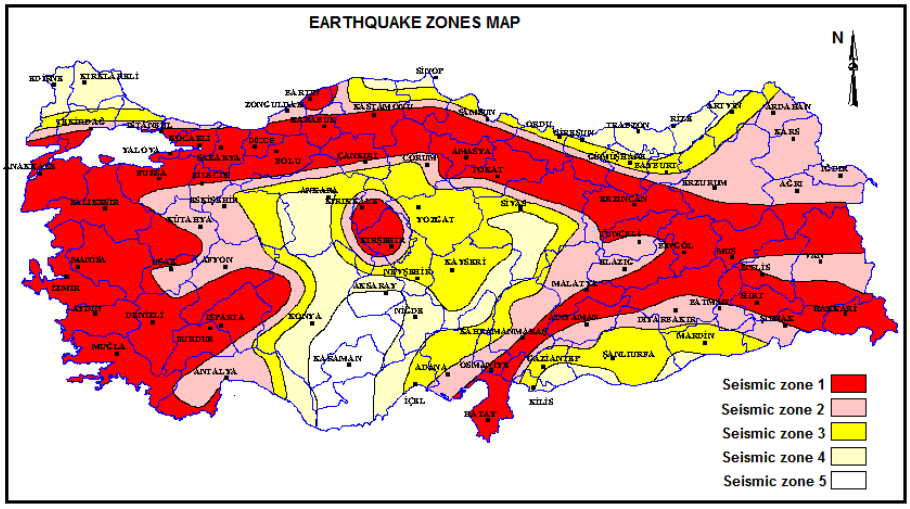

Fig. 6. The earthquake zones map for Turkey (arranged from http://deprem.gov.tr).

It is known fact that local soil conditions directly affect and change the characteristics of seismic movements and that these conditions can cause damage to existing buildings which are situated on these soils (Borcherd, 1990). Earthquake risk and soil type are one of the parameters to take into consideration. The local site classes and soil groups are determined by considering the ground criteria specified by TEC (2007). In the method, firstly, the hazard zone, in which the building is located, is determined taking into consideration seismic zones defined according to the soil class and the Turkish Earthquake Regulations. A base score (*TP*) is determined taking into account the number of building story according to the determined hazard zone. Structural system score (YSP) is determined according to type of the structural system. The obtained base score and structural system score are

added. In the later stage, the negativity parameter values corresponding to each negativity parameter in the building are multiplied by the negativity parameter score. The sum of the values obtained as a result of this multiplication is subtracted from the sum of the base score and the structural system score, and thus the performance score for the building is calculated. After this procedure is performed for each building, the risk priority is determined between the buildings. The effect of structural system type will be considered as a positive score. This score is shown in short as YSP. No additional positive score (YSP) will be given for the buildings with RC frame system (RCF). The positive parameter score (YSP) will be added to the buildings which have RC frame system + RC walls (RCFW) structural systems in respect to Table 3. Table 4 describes how to get the base and structural system score.

All negativity parameters except visible quality will be determined as "Yes" or "No". The negativity parameter values corresponding to these determinations will be taken as 1 and 0 respectively for the cases of "Yes" and "No". If the visible quality evaluation is "good", "medium", and "bad", then the negativity parameter value will be taken as 0, 1, and 2, respectively. The negativity coefficients corresponding to each parameter are shown in Table 4.

After each negativity coefficient is multiplied by negativity parameter score according to total number of storey located in the building, the sum of these values determines the total score of the negativities in the building. The negativity parameter scores are presented in Table 5.

One of the negativity parameters regarding the buildings is the pounding effect. For determining the pounding effect, it is first checked whether the building is detached or attached. If it is detached, the negativity parameter score is assigned as zero. If it is attached, then it is first checked whether the building is located in the middle or on the edge. In the later stage, the position of floors of the attached buildings to each other is checked. Fig. 7 is used to decide the floors with the same or different level.

Table 3. Base and structural system score table (DRBB, 2013)

Total number of storeys	Base score				Structural system score (*YSP*)	
	Seismic risk zone				Structural system type	
	I	II	III	IV	RCF	RCFW
1 and 2	90	120	160	195	0	100
3	80	100	140	170	0	85
4	70	90	130	160	0	75
5	60	80	110	135	0	65
6 and 7	50	65	90	110	0	55

Table 4. Negativity parameter values (O_i) (DRBB, 2013)

Negativity parameter no	Negativity parameter	Condition 1		Condition 2	
		Parameter determination	Parameter value	Parameter determination	Parameter value
1	Soft storey	No	0	Yes	1
2	Heavy overhang	No	0	Yes	1
3	Visual quality	Good	0	Average (Bad)	1 (2)
4	Short column	No	0	Yes	1
5	Hill/slope effect	No	0	Yes	1
6	Irregularity in plan	No	0	Yes	1
7	Vertical Irregularity	No	0	Yes	1

Table5. Negativity parameter score (OP_i) table (DRBB, 2013)

Storey level/Detached building condition											
Total number of storeys	Soft storey	Visual quality	Heavy overhang	Same Middle	Same Side	Different Middle	Different Side	Vertical irregularity	Irregularity in plan	Short column	Hillside effect
1,2	-10	-10	-10	0	-10	-5	-15	-5	-5	-5	-3
3	-20	-10	-20	0	-10	-5	-15	-10	-10	-5	-3
4	-30	-15	-30	0	-10	-5	-15	-15	-10	-5	-3
5	-30	-25	-30	0	-10	-5	-15	-15	-10	-5	-3
6,7	-30	-30	-30	0	-10	-5	-15	-15	-10	-5	-3

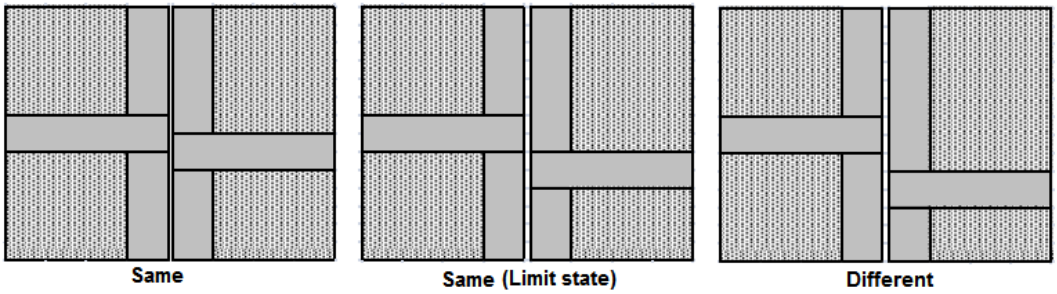

Fig. 7. Floors levels in adjacent buildings.

The performance score of a reinforced concrete building will be calculated with the data to be collected regarding the building. The building performance score for a reinforced concrete building will be calculated using the following formula;

$$PP = TP + \sum_{i=1}^{n} O_i \times OP_i + YSP \quad (2)$$

The above formulation is described as; *PP*- Performance Score; *TP*- Base Score; *Oi*- Irregularity Score and *YSP*- Structural System Score. The final scores are compared to each other for risky buildings and provide priority for retrofit. The performance score (*PP*) for each building will be calculated applying the method on the buildings in the region studied. The calculated performance scores will be sorted descending from high to low values. The risk priority by region can be determined using the distribution of the scores calculated in this way. The performance score is calculated using the formula 2 and determined as 295 for a building that is located in the hazard zone IV and includes no negativity parameter. The performance score is calculated as -118 for a building that is located in the hazard zone I and includes all negativity parameters. The performance scores in this quick evaluation method range from -118 to 295. The method's application procedure is broadly shown in Fig. 8.

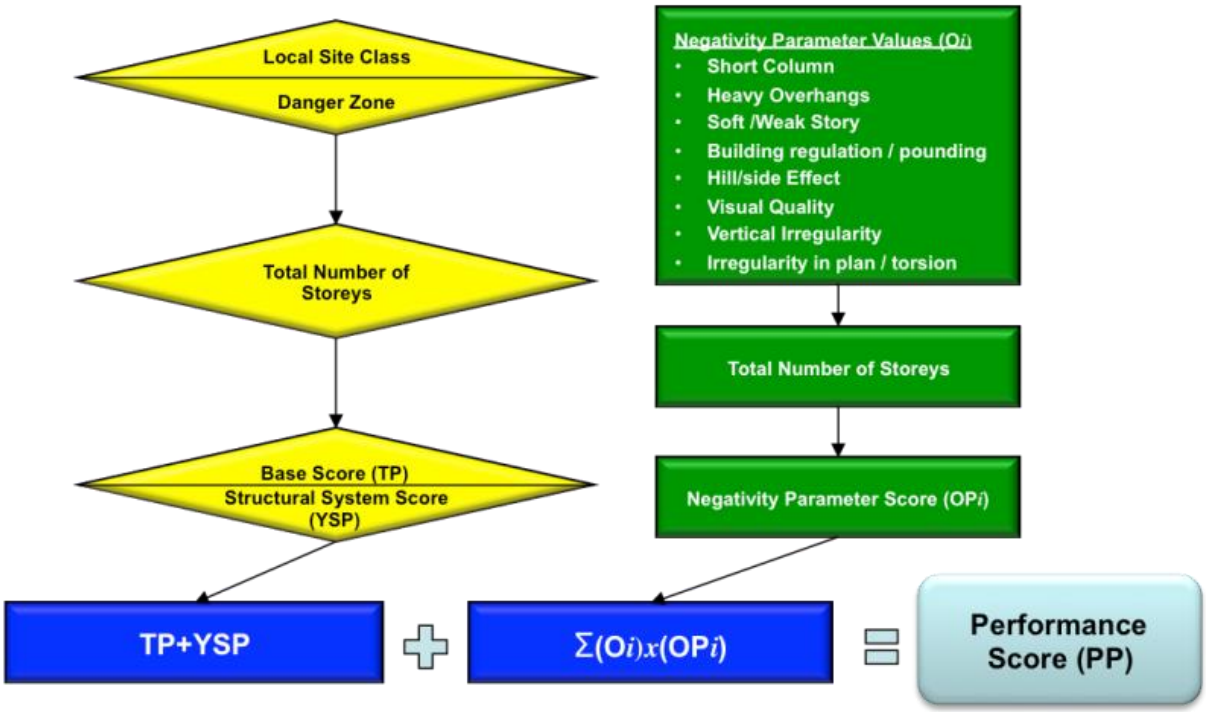

Fig. 8. Flowchart of the processes implemented in the study.

4. Analysis Results

Twenty RC buildings selected from each province which are 5-storey in Turkey were evaluated. Risk calculations were made for a total of 1620 reinforced concrete buildings from 81 provinces in Turkey. Following the creation of building credentials, the data on buildings' technical information was collected; it was seen that the data collection form prepared for the RC buildings consisted of the questions which can be filled out using observations from outside the building as suitable for visual screening method. In this context, the information such as the number of building stories, heavy overhangs, short columns, natural soil slope, building regulation, normal story function, which are located in the form, can be directly detected from outside the building, and there was no problem in determining these data in general. In this context, the data collection form given in Table 1 was

filled out for each building. The completed data collection forms were then transferred to the computer in the office. Some information about the buildings was also obtained with the transfer of the data. The values of the negativity parameters obtained for mid-rise RC buildings are shown in Fig. 9.

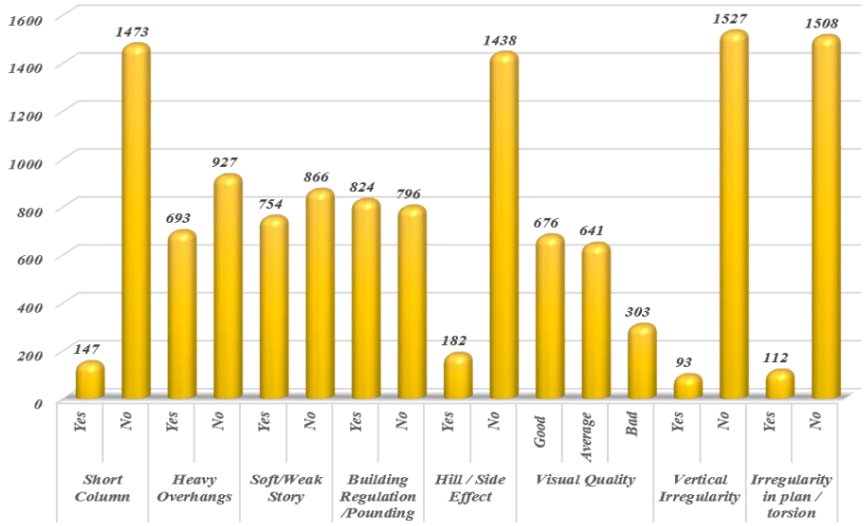

Fig. 9. Distribution of the negativity parameters of selected 5-storey buildings.

According to the results obtained, of the 1620 buildings examined, 9% had short columns, 43% had heavy overhangs, 47% had soft / weak story, 51% were attached buildings and could be subjected to pounding effect, 11% had hill/slope effect, 6% had vertical irregularity, and 7% had an irregularity in the plan. Also, it was determined that of the buildings examined, 42% had good quality, 40% had medium quality, and 18% had poor quality in terms of visual quality. The data collection form suitable for each building examined was filled out based on the observation made from outside the building, and the result performance scores of the buildings were calculated by deducting the penalty scores determined according to the structural defects observed in the building from the initial score defined for each building using the information in the form. The lower the resulting performance score, the higher the risk of building. Performance scores were calculated for each reinforced concrete building examined in the study, using the data collection form and equation 2. The distribution of these performance scores is shown in Fig. 10.

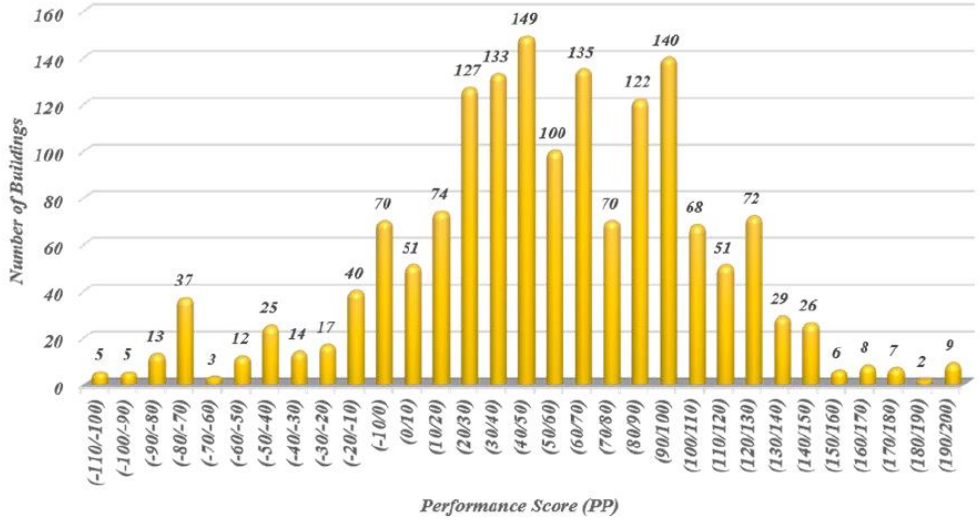

Fig. 10. The distribution of performance scores.

As it can be seen in the graphic, RC building performance scores range between -110 and 200. According to the distribution of performance scores of the reinforced concrete buildings examined in the study, the mean performance score of 1620 buildings was calculated as 53. This value is an average score, indicating that a significant percentage of the RC buildings in the region have high-performance scores. If the performance scores of all buildings with performance scores in the range of 50-200 are accepted to be higher than the mean score of 53,

a total of 845 buildings have performance scores on average or higher. 52% of the buildings have a higher performance score than the mean performance score. The provincial risk priority map has been created by considering the total scores of 20 RC buildings selected from each province in Turkey. The performance scores of 20 reinforced concrete buildings from each province were calculated separately. These scores obtained for 20 reinforced concrete buildings from each province were added, and thus a total score was obtained for each province. A mapping procedure was applied according to the total scores obtained. Because a decrease in the result scores increases the risk priority according to the quick evaluation method used in this study, the mapping procedure has been applied accordingly. This map is shown in Fig. 11. According to this map, the provinces with risk priority are Bitlis, Tekirdağ, Sakarya, Niğde, Tokat, and Rize.

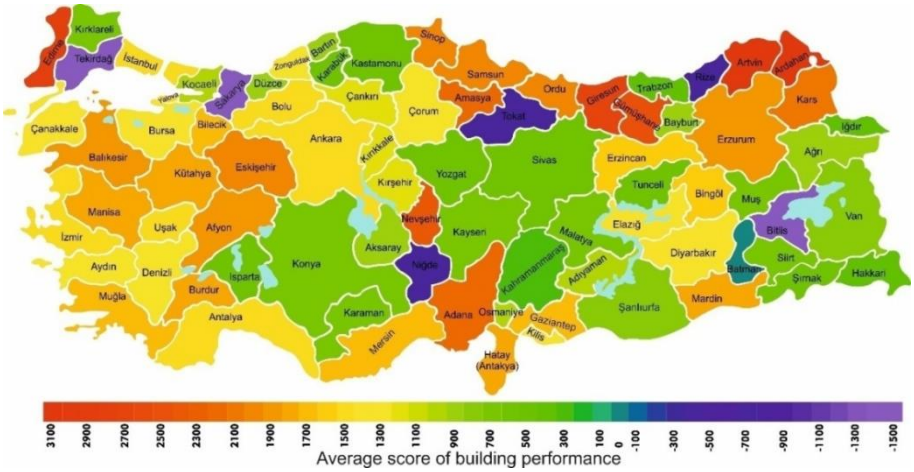

Fig. 11. The map for the risk priorities of cities according to the buildings included in this study.

5. Conclusions

Earthquake hazard is one of the main risks of human life in cities. *b*-value is an important parameter in terms of revealing the earthquake risk in settlements. In this study, changing of *a* and *b* values depending on Gutenberg-Richter (1942) relation in Turkey were examined, and the resulting value in the entire characteristic of earthquake occurrence was described. When these maps are examined, regional similarities are observed in the *a*-value distribution map in Fig. 2 and continuity can be defined in areas with near tectonic features. In contrast, the *b*-value distribution map in Fig. 3 shows no tectonic identification that can be associated with each other in the nearby settlements.

It cannot be said exactly whether buildings identified as low risk comply with existing earthquake regulations. As noted above, this is only the first stage assessment. Therefore, the final result can only be obtained as a result of certain analysis methods. This method aims only to determine the priorities of the buildings to be examined in the second stage evaluation method. However, selection of known earthquake behaviour buildings has made the results more valuable. The determination, analysis, detection and the management of all the information concerning the building stock of cities which gradually increase are important issues in terms of spatial planning and urban transformation. The priority of risky reinforced concrete buildings can be determined with this study.

The safe transfer of seismic loads to the soil through the structural system and the structural system's capability of reacting to the responses from the soil is directly related to the correct design and construction of the load-bearing mechanism. Therefore, avoiding all kinds of negativity will lead to adapt serious approaches to reduce the amount of damage that can occur in possible earthquakes. The calculation and design principles given in the building design rules must be strictly adhere in order to achieve this. Once this is achieved, then the construction of the properly designed buildings by their projects will contribute their project values.

A total of 1620 five-storey buildings from all provinces of Turkey were assessed. Twenty reinforced concrete buildings from each province were taken into consideration. These buildings were selected taking into consideration the population of the province they are located and the areas where the housing is intensive in the province. This number is a practically possible number. The first stage evaluation method specified in the principles regarding the identification of risky buildings promulgated in 2013 by the Republic of Turkey Ministry of Environment and Urbanization was used in this study. The performance scores for 1620 buildings were calculated using this method.

The buildings were examined in terms of effects such as heavy overhangs, soft story, short column, vertical irregularity and irregularity in the plan, which are included in the effects causing the building performance score to decrease in the RC buildings. These buildings were determined to be subjected to a pounding effect at most. In these structures, it was determined that the maximum number of collision effects was seen. Of the 1620 reinforced concrete buildings examined, 147 had short column effect, 693 had heavy overhangs, 745 had a soft story, 93 had vertical irregularity, and 112 had an

irregularity in the plan. This result showed that the negative structure properties were more effective in 1st stage evaluation.

The study shows the ranking of the buildings in the area concerned in terms of their performance scores and thus determines the buildings concentrated in a certain range of scores in certain areas. It is not possible to classify the buildings as risky, medium risky or riskless within the scope of the method. Only a ranking and comparison of performance scores between buildings can be performed using the existing data. Accordingly, it can be said that the building with a higher performance score is better than the building with lower performance score. Again within this context, the same comparison can be made regarding the areas where the buildings within a specific score range are concentrated. Accordingly, the data obtained in the study reveals that the buildings with lower performance scores are concentrated. It can be concluded that it is appropriate to prioritize these regions in disaster risk assessment plans or urban transformation project plans to be carried out within this scope.

In this context, it is thought that the rapid screening method used in the study serves for area prioritization as it stands, however, does not contain a limit value to compare the building performance scores, or is missing in terms of being able to comment on the risk situation of buildings because there is no guidance regarding the risk range.

To obtain correct and healthy data in the process of filling the building data collection forms, the field inspection team must be selected from civil engineers or construction technicians who have adequate knowledge and experience in accurately determining and interpreting the data requested in the data collection form.

The multiplicity of negativity parameters is related to housing and inadequate engineering services. The ground floors of the majority of the buildings were generally designed as workplaces, which, in turn, have led to the formation of a soft story. This has also led to an increase in the buildings' risk priority scores. Weak-soft story formation should be avoided as much as possible. Structural systems that are free of irregularities and were designed in compliance with the regulations as well as of which quality control was effectively carried out in construction phase may be damaged only in acceptable limits by showing a ductile behaviour even in a very severe earthquake.

Additionally, the construction of attached buildings has become widespread to optimize land use. Constructing detached buildings instead of attached buildings will be a useful way to reduce earthquake damages. Moreover, ground floors are constructed to have a lower surface area than upper floors to be able to fully utilize from the building area, but this leads to the formation of heavy overhangs.

The prepared map only indicates the provinces with the buildings that were examined in the study and have risk priority. All buildings in these provinces should be examined in order to report that they are exactly risky.

Such work will lead to the system of earthquake prevention, which will be used to analyses an inventory of building stock against earthquake. While taking precautionary measures against reducing earthquake risk after producing a building inventory, the buildings, which are not safe and not economical to strengthen, need to be demolished. This study includes the previous earthquake code and rapid assessment method. This study will be a resource for similar studies based on new codes.

References

Ahmed MM, Jahan I, Alam MJ (2014). Earthquake vulnerability assessment of existing buildings in cox's-bazar using field survey & GIS. *International Journal of Engineering*, 3(8), 1147-1156.

Aki K (1965). Maximum likelihood estimate of b in the formula log N=a-bM and its confidence limits. *Bulletin of the Earthquake Research Institute,* 43**,** 237-239.

Aksoylu C, Öztürk O, Erkan İH, Arslan MH (2016). Investigation of vertical column discontinuity in reinforced concrete buildings. *International Journal of Scientific & Engineering Research*, 7(6), 474-481.

Alam N, Alam MS, Tesfamariam S (2012). Buildings' seismic vulnerability assessment methods: a comparative study. *Natural Hazards*, 62(2), 405-424.

Alan E (2016). Deprem İstatistik Programı V1. Alan Mühendislik, Turkey.

Albayrak U, Canbaz M, Albayrak G (2015). A rapid seismic risk assessment method for existing building stock in urban areas. *Procedia Engineering*, 118, 1242-1249.

Anadolu NC, Kalyoncuoğlu ÜY (2010). Güneydoğu Anadolu Bölgesinin depremselliği ve deprem tehlike analizi. *Süleyman Demirel University Journal of Natural and Applied Science*, 14(1), 84-94.

Arslan MH, Ceylan M, Kayuncu TA (2010). New method for rapid assessment of performances of existing RC buildings under earthquake loading. *IV. European Conference on Computational Mechanics Palais des Congrès*, Paris, France

Arslan MH, Olgun M, Köroğlu MA, Erkan IH, Köken A, Tan O (2013). 19 May 2011 Kütahya--Simav earthquake and evaluation of existing sample RC buildings according to the TEC-2007 criteria. *Natural Hazards & Earth System Sciences*, 13(2).

Ates A, Kayıran T, Sincer I (2003). Structural interpretation of the Marmara region, NW Turkey, from aeromagnetic, seismic and gravity data. *Tectonophysics*, 367(1-2), 41-99.

Ateş A, Bilim F, Büyüksaraç A, Bektaş O (2008). A tectonic interpretation of the MarmaraSea, NW Turkey from geophysical data. *Earth Planets and Space*, 60(3), 169–177.

Ateş A, Büyüksaraç A, Bilim F, Bektaş Ö, Şendur Ç, Komanovalı G (2009). Spatial correlation of the aeromagnetic anomalies and seismogenic faults in the Marmara region, NW Turkey. *Tectonophysics*, 478(1-2), 135-142.

Ates A, Bilim F, Buyuksarac A, Aydemir A, Bektas O, Aslan Y (2012). Crustal structure of Turkey from aeromagnetic, gravity and deep seismic reflection data. *Surveys in Geophysics*, 33(5), 869-885.

Bal IE, Gulay FG, Tezcan SS (2008). A new approach for the preliminary seismic assessment of RC buildings: P25 scoring method. *Proceedings of 14th WCEE*, 12-17.

Bayrak Y, Çinar H, Bayrak E (2011). The North Anatolian Fault Zone: an evaluation of earthquake hazard parameters. *In: New Frontiers in Tectonic Research - At the Midst of Plate Convergence, Uri Schattner, Ed.,* Intech Open, Zagrep, 269-280.

Bayraktar A, Altunişik AC, Pehlivan M (2013). Performance and damages of reinforced concrete buildings during the October 23 and November 9, 2011 Van, Turkey, earthquakes. *Soil Dynamics and Earthquake Engineering*, 53, 49-72.

Benavent-Climent A (2011). A seismic index method for vulnerability assessment of existing frames: application to RC structures with wide beams in Spain. *Bulletin of Earthquake Engineering*, 9(2)**,** 491-517.

Bender B (1983). Maximum likelihood estimation of b values for magnitude grouped data. *Bulletin of the Seismological Society of America*, 73(3), 831–851.

Bilgin H (2016). Generation of fragility curves for typical RC health care facilities: emphasis on hospitals in Turkey. *Journal of Performance of Constructed Facilities*, 30(3), 04015056.

Bilgin H, Frangu I (2017). Predicting the seismic performance of typical R/C healthcare facilities: emphasis on hospitals. *International Journal of Advanced Structural Engineering*, 9(3), 277-292.

Bilgin H, Uruçi R (2018). Effects of structural irregularities on low and mid-rise RC building response. *Challenge Journal of Structural Mechanics*, 4(2), 33-44.

Borcherdt RD (1990). Influence of local geology in the San Francisco bay region California on ground motions generated 1990, by the Loma Prieta earthquake of October 17, 1989. *Proceedings of International Symposium on Safety of Urban Life and Facilities,* Tokyo, Japan.

Bozkurt E (2001). Neotectonics of Turkey - a synthesis. *Geodinamica Acta*, 14, 3-30.

Cao A, Gao SS (2002). Temporal variation of seismic b-values beneath northeastern Japan island arc. *Geophysical Research Letters*, 29(9), 1–3.

Chever L (2012). Use of seismic assessment methods for planning vulnerability reduction of existing building stock. *Proceedings of the 15th World Conference on Earthquake Engineering—WCEE,* Lisbon, Portugal.

DRBB (Determination of Risk-Bearing Buildings) (2013). Afet riski altındaki alanların dönüştürülmesi hakkında kanunun uygulama yönetmeliğinde değişiklik yapılmasına dair yönetmelik. Türkiye Çevre ve Şehircilik Bakanlığı, Ankara, Turkey.

Eleftheriadou AK, Karabinis AI (2012). Seismic vulnerability assessment of buildings based on damage data after a near field earthquake (7 September 1999 Athens- Greece). *Earthquake and Structures,* 3(2)**,** 117-140.

Farrell J, Husen S, Smith RB (2009). Earthquake swarm and b-value characterization of the Yellowstone volcano–tectonic system. *Journal of Volcanology and Geothermal Research*, 188, 260–276.

FEMA-154 (2002*). Rapid Visual Screening of Buildings for Potential Seismic Hazards: a Handbook*, Federal Emergency Management Agency, Washington.

Foo S, Davenport A (2003). Seismic hazard mitigation for buildings. *Natural Hazards*, 28(2-3), 517-536.

Gülay FG, Bal İE, Gökçe T, Çelik N (2010). Field applications of P25 preliminary assessment method for identifying the collapse vulnerability of existing RC structures. *9th International Congress on Advances in Civil Engineering*, Karadeniz Technical University, Trabzon, Turkey, 10p.

Gutenberg B, Richter CF (1944). Frequency of earthquakes in California. *Bulletin of the Seismological Society of America*, 34(4), 185-188.

Hadzima-Nyarko, M., Nyarko, E. K., Morić, D. (2011). A neural network based modelling and sensitivity analysis of damage ratio coefficient. *Expert Systems with Applications*, 38(10), 13405-13413.

Hadzima-Nyarko M, Pavic G, Lesic M (2016). Seismic vulnerability of older confined masonry buildings in Osijek, Croatia. *Earthquakes and Structures*, 11(4), 629-648.

Hadzima-Nyarko M, Mišetić V, Morić D (2017). Seismic vulnerability assessment of an old historical masonry building in Osijek, Croatia, using Damage Index. *Journal of Cultural Heritage*, 28, 140-150.

Hadzima-Nyarko M, Morić D, Pavić G, Mišetić V (2018). Spectral functions of damage index (DI) for masonry buildings with flexible floors. *Tehnički Vjesnik*, 25(1), 181-187.

Harirchian E, Lahmer T, Buddhiraju S, Mohammad K, Mosavi A (2020). Earthquake safety assessment of buildings through rapid visual screening. *Buildings*, 10(3), 51.

Inel M, Meral E (2016). Seismic performance of RC buildings subjected to past earthquakes in Turkey. *Earthquakes and Structures,* 11(3), 483-503.

Inel M, Ozmen HB, Bilgin H (2008). Re-evaluation of building damage during recent earthquakes in Turkey. *Engineering Structures*, 30(2), 412-427.

Ishimoto M, Lida K (1939). Observations sur les seismes enregistres parle microsismographe construit dernierement (1). *Bulletin of the Earthquake Research Institute, The University of Tokyo*, 17, 443-478.

Işık E (2013). The evaluation of existing buildings in Bitlis province using a visual screening method. *Süleyman Demirel University Journal of Natural and Applied Science,* 17(1), 173-178.

Işık E (2015). Investigation of an existing RC building with different rapid assessment method. Bitlis Eren University, *Journal of Science and Technology*, 5(2), 71-74.

Işık E (2016). Consistency of the rapid assessment method for reinforced concrete buildings. *Earthquakes and Structures*, 11(5)**,** 873-885.

Işık E, Kutanis M (2015). Performance based assessment for existing residential buildings in Lake Van basin and seismicity of the region. *Earthquakes and Structures*, 9(4), 893-910.

Işık E, Işık MF, Bülbül MA (2017). Web based evaluation of earthquake damages for reinforced-concrete buildings. *Earthquakes and Structures*, 13(4), 423-432.

Işık E, Tozlu Z (2015). Calculation of building performance score by using different variables. *BEU Journal of Science,* 4(2), 161-172.

Işık MF, Işık E, Bülbül MA (2018). The application of IOS / android based assessment and monitoring system for building inventory under the impact of earthquake. *Gradevinar*, 70(12), 1095-1108.

Ilki A, Comert M, Demir C, Orakcal K, Ulugtekin D, Tapan M, Kumbasar, N (2014). Performance based rapid seismic assessment method (PERA) for reinforced concrete frame buildings. *Advances in Structural Engineering,* 17(3), 439-459.

Jain SK, Mitra K, Kumar M, Shah, M (2010). A proposed rapid visual screening procedure for seismic evaluation of RC-frame buildings in India. *Earthquake Spectra*, 26(3), 709-729.

Kalafat D, Güneş Y, Kekovalı K, Kara M, Deniz P, Yılmazer M (2011). A revised and extended earthquake catalogue for Turkey since 1900 (M≥4.0). İstanbul, Turkey: Boğaziçi University Kandilli Observatory and Earthquake Research Institute.

Kalyoncuoğlu UY (2007). Evaluation of seismicity and seismic hazard parameters in Turkey and surrounding area using a new approach to the Gutenberg–Richter relation. *Journal of Seismology*, 11, 131–148.

Kalyoncuoğlu UY, Elitok Ö, Dolmaz MN (2013).Tectonic implications of spatial variation of b-values and heat flow in the Aegean region. *Marine Geophysical Researches*, 34, 59–78.

Kaminosono T (1992). Evaluation method for seismic capacity of existing reinforced concrete buildings in Japan. In Memoria (pp. 44-53). México. Centro Nacional de Prevención de Desastes (CENAPRED); Japón. Agencia de Cooperación Internacional (JICA); NU. Centro para el Desarrollo Regional (UNCRD).

Kepekci D, Ozcep F (2011). Fast-track earthquake risk assessment for selected urban areas in Turkey. *Natural Hazards and Earth System Sciences*, 11(2), 571-585.

Mirshafiei F, Mirshafiei M, McClure G (2017). A new three-dimensional seismic assessment method (3D-SAM) for buildings based on experimental modal analysis. *Computers & Structures*, 180, 125-137.

Mogi K (1962). Magnitude-frequency relationship for elastic shocks accompanying fractures of various materials and some related problems in earthquakes. *Bulletin of the Earthquake Research Institute, The University of Tokyo*, 40, 831-883.

Monterroso D (2003). Seismic precursory potential of temporal variation of b-value: five case studies in Central America. *Comprehensive Summaries of Uppsala Dissertations from the Faculty of Science and Technology*, 897-914.

Monterroso D, Kulhanek O (2003). Spatial variations of b-values in the subduction zone of Central America. *Geofisica International*, 42, 1-13.

Murru M, Console R, Falcone G, Montuori C, Sgroi T (2007). Spatial mapping of the b value at Mount Etna, Italy, using earthquake data recorded from 1999 to 2005. *Journal of Geophysical Res*earch, 112, B12303.

NRRC (1993). Manual for Screening of Buildings for Seismic Investigation. Canadian Standard. National Research Council of Canada, Ottowa, Canada.

Nuannin P, Kulhanek O, Persson L (2005). Spatial and temporal b value anomalies preceding the devastating off coast of NW Sumatra Earthquake of December 26, 2004. *Geophysical Research Let*ters, 32, L11307

Ohkubo M (1991). Current Japanese system on seismic capacity and retrofit techniques for existing reinforced concrete buildings and post-earthquake damage inspection and restoration techniques, Report No. SSRP-91/02, Department of Applied Mechanics and Engineering Sciences, University of California, San Diego.

Okada T (1999). Needs to evaluate real seismic performance of buildings-lessons from the 1995 Hyogoken-nambu Earthquake. *INCEDE Report*, 15, 225-231.

Ozcebe G (2004). Seismic assessment and rehabilitation of existing buildings. *TÜBITAK Research Report,* no: ICTAG YMAU I, 574.

Ozmen HB, Inel M (2017). Effect of rapid screening parameters on seismic performance of RC buildings. *Structural Engıneerıng and Mechanics*, 62(4), 391-399.

Reilinger R, McClusky S, Vernant P, Lawrence S, Ergintav S, Cakmak R, Ozener H, Kadirov F, Guliev I, Stepanyan R (2006). GPS constraints on continental deformation in the Africa–Arabia–Eurasia continental collision zone and implications for the dynamics of plate interactions. *Journal of Geophysical Research,* 111.

Richter CF (1935). An instrumental earthquake magnitude scale. *Bulletin of the Seismological Society of America*, 25(1), 1-32.

Roberts NS, Bell AF, Main IG (2015). Are volcanic seismic b-values high, and if so when? *Journal of Volcanology and Geothermal Research*, 308, 127–141.

Scawthorn C (1986). Techniques for Rapid Assessment of Seismic Vulnerability. ASCE, USA.

Scholz CH (1968). The frequency-magnitude relation of microfracturing in rock and its relation to earthquakes. *Bulletin of Seismology Society of Am*erica, 58, 399-415.

Shehu R, Angjeliu G, Bilgin H (2019). A Simple approach for the design of ductile earthquake-resisting frame structures counting for P-Delta effect. *Buildings*, 9(10), 216.

Sinha R, Goyal A (2004). A national policy for seismic vulnerability assessment of buildings and procedure for rapid visual screening of buildings for potential seismic vulnerability. Report to Disaster Management Division, Ministry of Home Affairs, Government of India.

Srikanth T, Kumar RP, Singh AP, Rastogi BK, Kumar S (2014). Earthquake vulnerability assessment of existing buildings in Gandhidham and Adipur cities Kachchh, Gujarat (India). *European Journal of Scientific Research*, 41(3), 336-353.

Sucuoğlu H (2007). A screening procedure for seismic risk assessment in urban building stocks. *6th National Conference on Earthquake Engineering*, İstanbul, Turkey

Suyehiro S, Asada T, Ohtake M (1964). Foreshocks and aftershocks accompanying a perceptible earthquake in central Japan: On the peculiar nature of foreshocks. *Papers in Meteorology and Geophysics*, 19, 427-435.

Šipoš TK, Hadzima-Nyarko M (2017). Rapid seismic risk assessment. *International Journal of Disaster Risk Reduction*, 24, 348-360.

Tabban A (2000). Kentlerin Jeolojisi ve Deprem Durumu. *Jeoloji Mühendisleri Odası Yayınları,* 56, 500 p.

Taymaz T, Eyidoğan H, Jackson J (1991). Source parameters of large earthquakes in the East Anatolian Fault Zone (Turkey). *Geophysical Journal International*, 106, 537-550.

Tesfamariam S, Liu Z (2010). Earthquake induced damage classification for reinforced concrete buildings. *Structural Safety*, 32(2), 154-164.

Tischer H, Mitchell D, McClure G (2011). Comparison of seismic screening methods for schools in a moderate seismic zone. *Proceedings of the COMPDYN*.

Tischer H, McClure G, Mitchell D (2012). Development of a seismic vulnerability assessment method for schools in Eastern Canada. *Proceedings of the 15th World Conference on Earthquake Engineering — WCEE*, Lisbon, Portugal.

Turkish Earthquake Code (2007), Turkish Earthquake Code-Specification for Structures to be built in Disaster Areas, Ankara, Turkey.

Utkucu M, Durmus H, Yalçin H, Budakoglu E, Isik E (2013). Coulomb static stress changes before and after the 23 October 2011 Van, eastern Turkey Earthquake (MW= 7.1): implications for the earthquake hazard mitigation. *Natural Hazards and Earth System Sciences*, 13(7), 1889.

Warren NW, Latham GV (1970). An experiment study of thermal induced microfracturing and its relation to volcanic seismicity. *Journal of Geophysical Reearch,* 75, 4455-4464.

Wessel P, Smith WHF (1991). Free software helps map and display data. *Eos, Transactions American Geophysical Union*, 72, 441.

Wiemer S, Benoit J (1996). Mapping the b-value anomaly at 100 km depth in the Alaska and New Zealand subduction zones. *Geophysical Research Letters,* 23, 1557-1560.

Wiemer S, McNutt SR, Wyss M (1998). Temporal and three-dimensional spatial analyses of the frequency-magnitude distribution near Long Valley Caldera, California. *Geophysical Journal International*, 134, 409-421.

Wyss M (1973). Towards a physical understanding of the earthquake frequency distribution. *Geophysical Journal of the Royal Astronomical Society,* 31, 341-359.

Villacís C, Cardona CN, Tucker B (2000). Implementation of fast earthquake scenarios for risk management in developing countries. *Proceedings of the 12th World Conference on Earthquake Engineering* (*12WCEE*), Auckland, New Zealand.

Yakut A (2004). Preliminary seismic performance assessment procedure for existing RC buildings. *Engineering Structures,* 26(10), 1447-1461.

Yakut A, Erberik MA, Ilki A, Sucuoğlu H, Akkar S (2014). Rapid seismic assessment procedures for the Turkish Building Stock. In *Seismic Evaluation and Rehabilitation of Structures*, 15-35.

Zülfikar AC, Fercan NÖZ, Tunç S, Erdik M (2017). Real-time earthquake shake, damage, and loss mapping for Istanbul metropolitan area. *Earth, Planets and Space*, 69(1), 9.

Challenge Journal of Structural Mechanics

Case Study

Comparison between fixed base and isolated base in seismic response of high-rise buildings: a case study

Anas M. Fares [a,*]

[a] *Department of Civil Engineering, Faculty of Engineering, Necmettin Erbakan University, 42140 Konya, Turkey*

ABSTRACT

In this study, the influence of soil condition under the isolated and fixed bases is studied by using ETABS 16 software for a high-rise regular building. A regular building with 10 floors is modeled and the results are obtained for story displacements, story shear forces and spectral acceleration according to the Uniform Building Code 97 (UBC-97) code. The time history analysis has been performed by using 1999 Izmit earthquake record. 3 types of soil which have different stiffnesses are considered in this study. The results show that the value of the base shear increases when the soil stiffness decreases. It also noticed that the spectral acceleration is larger in soft soil condition than that of other soil conditions; and this confirms that the structural response spectrum depends on the soil condition. In addition, when using base isolated building the drift of lower floors will be larger than that of using base isolated, but in the upper floors the drifts of fixed base building will be larger than that of the isolated base building. Finally, the time history method in the seismic design will produce base shear less than that from equivalent static method, so calibration factor for design purpose shall be used.

ARTICLE INFO

Article history:
Received 20 April 2020
Revised 21 May 2020
Accepted 3 June 2020

Keywords:
Nonlinear time history analysis
Isolated base
Fixed base
Spectral acceleration
UBC-97

1. Introduction

Loads are transferred from vertical structural elements to the soil by foundations. The foundations represent the upper layer of the earth. The condition of soil under foundations may be assumed as an important factor in the seismic analysis and design of structures. The engineering codes such as the Uniform Building Code 97 (UBC-97, 1997) and the International Building Code (IBC) have been classified soil according to its stiffness. In UBC-97, the soil is classified into 6 categories: 1) hard rock (SA), 2) rock (SB), 3) very dense soil and soft rock (SC), 4) stiff soil profile (SD), 5) soft soil profile (SE), 6) very soft soil which requiring site-specific analysis (SF). (UBC-97, 1997). During the earthquake, the deformation and vibration of the soil under the footings of the building cause the structure to vibrate and floors to move which produce base shear, base moment, and lateral displacement of slabs (Sayani and Ryan, 2009; Hatami, 2015).

Researchers (Sayani and Ryan, 2009; Hatami, 2015; Hassan et al., 2018) have tried to study the effect of soil-structure interaction on the seismic response of structures. They found that the interaction between soil and structure play major role especially in the results of natural frequency of building and in the energy dissipation. Conflicting assumptions in design process are found between structural engineers who assume flexible structures on rigid foundations and geotechnical engineers who assume flexible foundations supporting rigid structures (Touqan, 2008). Researchers found that the damages which occur during the earthquake are not in the same pattern for buildings which locate in the same region, and same earthquake magnitude (Jayalekshmi et al., 2016).

It means that there are some factors which affect the shape of damage of structures like: soil condition under foundations, structural system of plans, building mass and stiffness and vertical irregularities of buildings (Gjorgjiev, 2012; Magade et al., 2008).

* *Corresponding author*. E-mail address: anas_fares76@yahoo.com (A. M. Fares)
ISSN: 2149-8024 / DOI: https://doi.org/10.20528/cjsmec.2020.04.005

Nomenclature

C_a	acceleration seismic coefficient
C_v	velocity seismic coefficient
V	total base shear
R	overstrength factor
I	importance factor of the building
W	total weight of the building
T	fundamental period of the building
F_y	yielding strength of steel
f_c'	concrete compressive strength
h	height of the building
C_t	coefficient of period depending on the lateral resisting system
f_i	lateral force at level *i* of the floor
δ_i	elastic deflection due to lateral force at level *i* of the floor
g	gravity acceleration
w_i	weight at level *i* of the floor

It is thus of prime importance to quantify the effect of soil condition beneath the foundation on the dynamic performance of the building. To conduct this study the popular commercial finite element program, ETABS16 software, has been used by running nonlinear time history analysis (CSI, 2017). Then, the seismic response of the building which is provided by fixed base and isolated base of the structure at 3 different soil type conditions according to UBC-97 will be discussed. The soil profiles are: hard rock (S_A), very dense soil and soft rock (S_C) and soft soil profile (S_E).

When using UBC-97 code, the seismic coefficient C_a and C_v shall be found from code tables for a specific seismic zone (Z). In this paper and for seismic zone Z=0.30, the C_a and C_v are found and summarized in Table 1. The reasons for using the same seismic zone are to compare the results of the three different soil types at that same zone. Moreover, to study the effect of the stiffness of soil on the seismic response of the high buildings in both fixed bases and isolated bases conditions.

Fig. 1 shows the UBC-97 response spectrum curve for the previous types of soil.

Table 1. Seismic coefficient.

Z=0.30		
Soil type	C_a	C_v
S_A	0.24	0.24
S_C	0.33	0.45
S_E	0.36	0.84

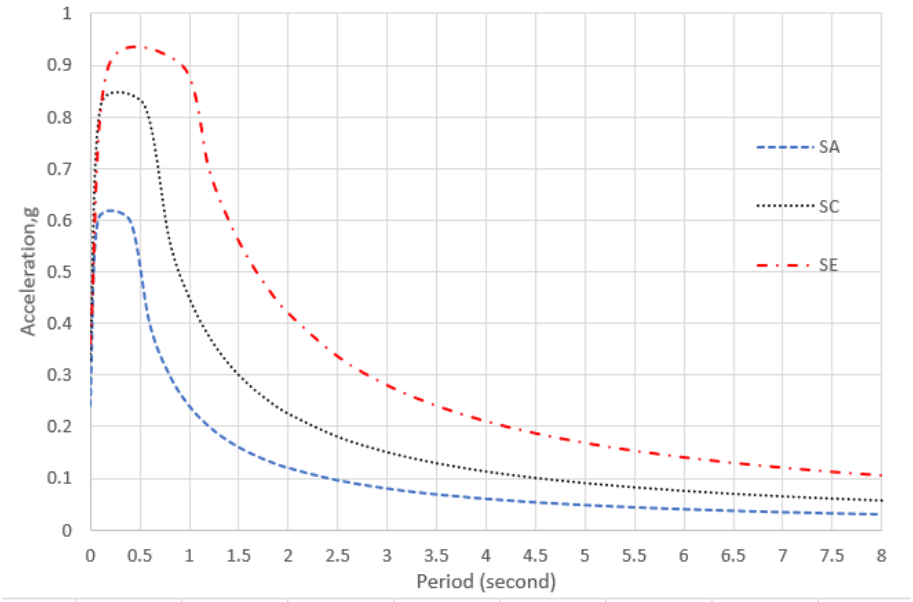

Fig. 1. UBC-97 response spectrum curve.

2. Modeling of the Building

In this study, ETABS 16 has been used as a commercial Finite Element software. The nonlinear time history analysis is conducted. The slabs are modeled as 2D shell-thin members. The beams and columns are modeled as 1D line members. The results from the program will show the performance levels and the behavior of the buildings.

10 floors are simulated and Uniform Building Code 1997 (UBC-97) is taken into consideration. All input data for materials properties, reinforced concrete sections, and type of loads as given in Table 2.

Isolator characteristics are as described and calculated at the book of Kelly and Naeim (Kelly J. and Naeim F., Design of seismic isolated structures, 1999) and Table 3 summarizes the final results. The isolator which used in the model will be the same for all columns and depending on the maximum axial load in the building. This

assumption is used to simplify the modeling process and to make the analysis as fast as possible. The structural system is chosen to be special moment resisting frames.

Fig. 2 shows the modeled columns layout, while Fig. 3 shows the 3D view of the building as modeled in ETABS 16. The building is assumed to be regular in the both main directions, because this type of building behaves more safely during the earthquake. Moreover, using this assumption leads to simplifying the modeling process and it reduces the time which is required to analyze the model using nonlinear time history analysis.

Figs. 4, 5 and 6 show the matched response spectrum-time history functions for Izmit 1999 earthquake for hard rock (S_A), very dense soil and soft rock (S_C) and soft soil (S_E) respectively. The direction of the time history is south to north (S-N).

Table 2. ETABS input data.

Concrete f'_c	24 MPa
Steel f_y	420 MPa
Floor height	3.00 m
Superimposed load	4.00 kN/m²
Live load	2.5 kN/m²
Masonry wall load	15 kN/m
Columns	50x50 cm
Beams	30/50 cm
Two-way solid slab thickness	20 cm
Overstrength factor, R	8.5
Eccentricity ratio	0.05

Table 3. Isolator characteristics.

Maximum vertical column load	4296 kN
U_1 effective stiffness	2668580.68 kN/m
U_2 and U_3 effective stiffness	2668.60 kN/m
Yield displacement	0.00321 m
U_2 and U_3 stiffness	24591 kN/m
Damping ratio	0.05

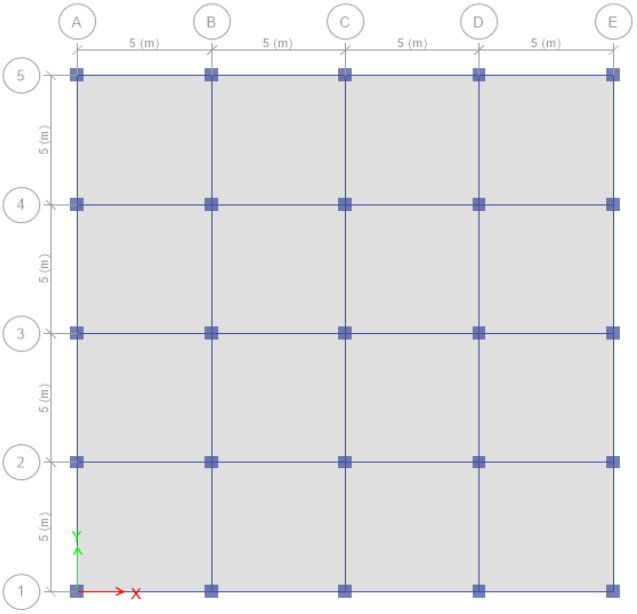

Fig. 2. Columns layout.

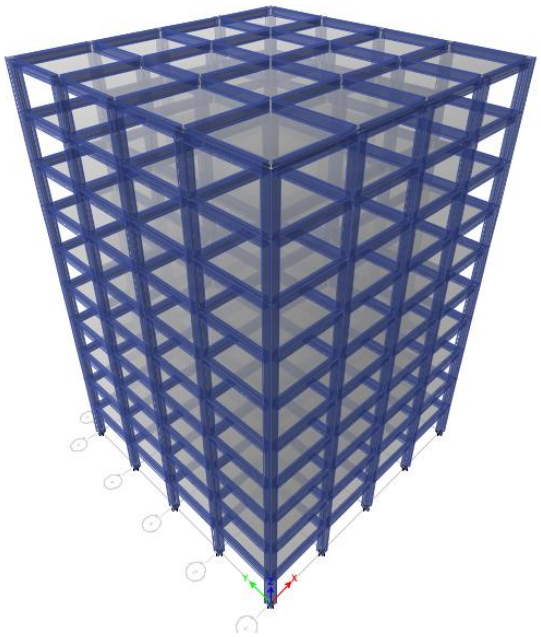

Fig. 3. 3D model of building.

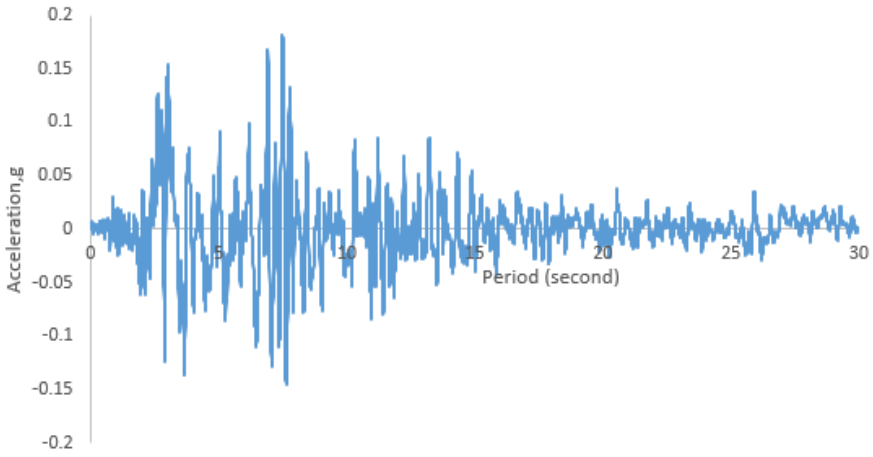

Fig. 4. Matched response spectrum- time history function for Izmit 1999 earthquake for hard rock (S_A).

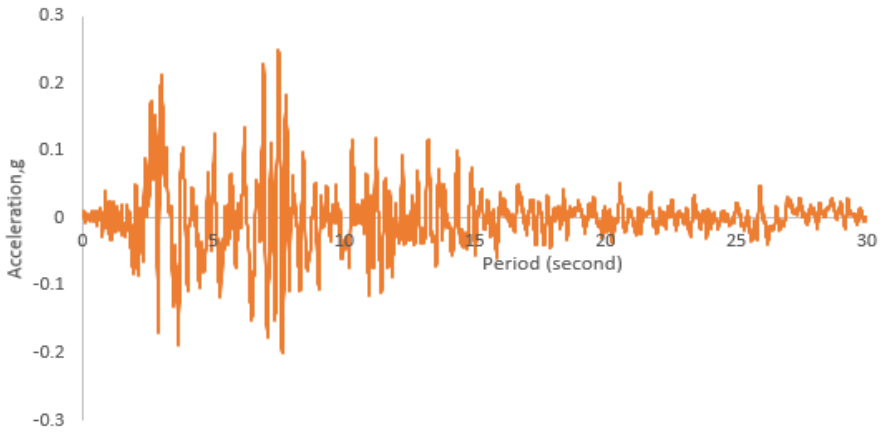

Fig. 5. Matched response spectrum- time history function for Izmit 1999 earthquake for very dense soil and soft rock (S_C).

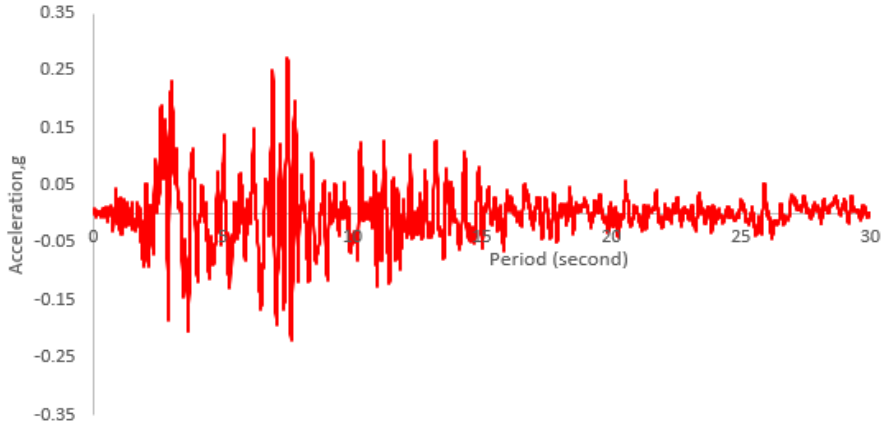

Fig. 6. Matched response spectrum- time history function for Izmit 1999 earthquake for soft soil (S_E).

3. Verification of the Analysis

When using any finite element program, it is much important to verify the analysis results which will obtain. The verifications can be found as a percentage of difference between hand calculation and program results (Alnajajra et al., 2017). This difference shall not be greater than a certain value which described in the ETABS manual. The results of the static analysis are proved according to CSI (2017):

1. The condition of compatibility: Where all members in the model should be connected and move together with no gaps. Fig. 7 shows the satisfaction of this condition from the dead load deflected shape.
2. The condition of equilibrium: Where the applied loads shall be equal to the reaction loads from the analysis; If it is not, then a difference between program results and manual results should be less than or equal to 5% to be accepted. This condition is satisfied as shown in Table 4.
3. The stress strain relationship: Where the internal forces such as bending moment, shear and axial forces from program results should be equal to the manual results; If it is not, then an acceptable difference between program results and manual results should be less than or equal to 10% . This condition is satisfied by finding axial load in a specific column as shown in Fig. 8 and Table 5.

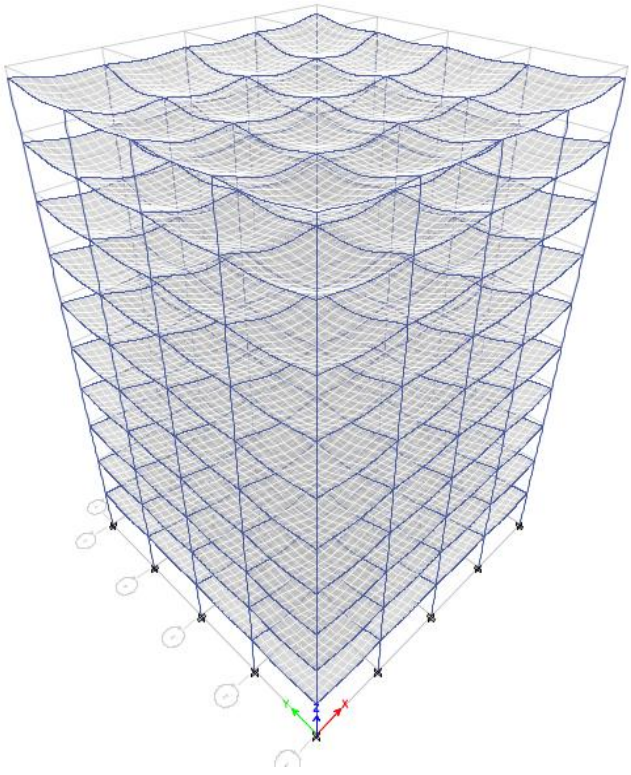

Fig. 7. 3D deflection shape from dead load.

Table 4. Check for the balance of forces.

Item	ETABS results	Manual results	Difference (%)
Weight of the structure (kN)	28737.50	29187.50	1.54
Superimposed dead load (kN)	28000	28000	0.00
Live load (kN)	10000	10000	0.00

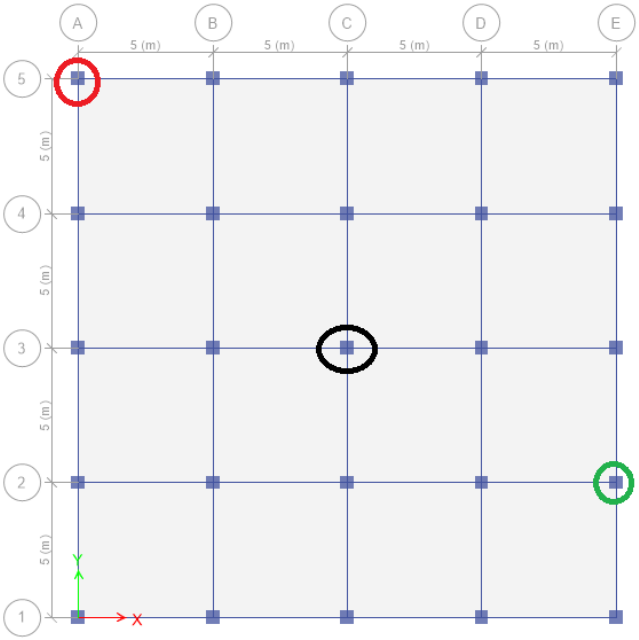

Fig. 8. Location of the checked columns.

4. Results of the Building Analysis

After analyzing the models, the results are obtained and curves are drawn.

4.1. Story displacement

Fig. 9 shows the floors top displacement results for both conditions of isolated base (IB) and fixed base (FB) for soil S_A for Time History Analysis in X direction. Due to the symmetry of the building the THA results are the same for both X direction and Y direction. Fig. 10 shows the same but for medium soil S_C and for soft soil S_E Fig. 11.

Tables 6, 7 and 8 show the difference between floors top displacements according to fixed base and isolated base for soil S_A, S_C and S_A respectively. The differences are calculated with respect to fixed base condition.

As shown in the following figures and tables, the soil stiffness is playing a major role in the lateral displacement of each floor in the building. When the soil stiffness is very strong as in S_A case, then the lateral displacement value of floors will be small comparing to the other cases such as S_C and S_E soils. This result can make advice to engineers to construct buildings on a hard soil such as rock, and to avoid build structures on a weak soil.

Also, when using base isolated buildings, the first floor lateral displacement value shall be more than that of the fixed base building and if you move away from the footing, the lateral displacement of floors of fixed base will be larger than the base isolated buildings, and this trend is the same for all type of soil cases.

In general, it can be illustrated that base isolated gives lateral displacement more than that of fixed base, and this will produce flexible structures.

Table 5. Check for the axial load internal force.

Columns position	Item	ETABS results	Manual results	Difference (%)
Internal	Dead load (kN)	1646.50	1662.50	0.97
Internal	Superimposed load (kN)	994.87	1000	0.51
Internal	Live load (kN)	628	625	0.47
Edge	Dead load (kN)	965.22	981.25	1.66
Edge	Superimposed load (kN)	1223.93	1250	2.13
Edge	Live load (kN)	312.86	312.50	0.11
Corner	Dead load (kN)	586.09	612.50	4.50
Corner	Superimposed load (kN)	968.26	1000	3.27
Corner	Live load (kN)	147.69	156.25	5.79

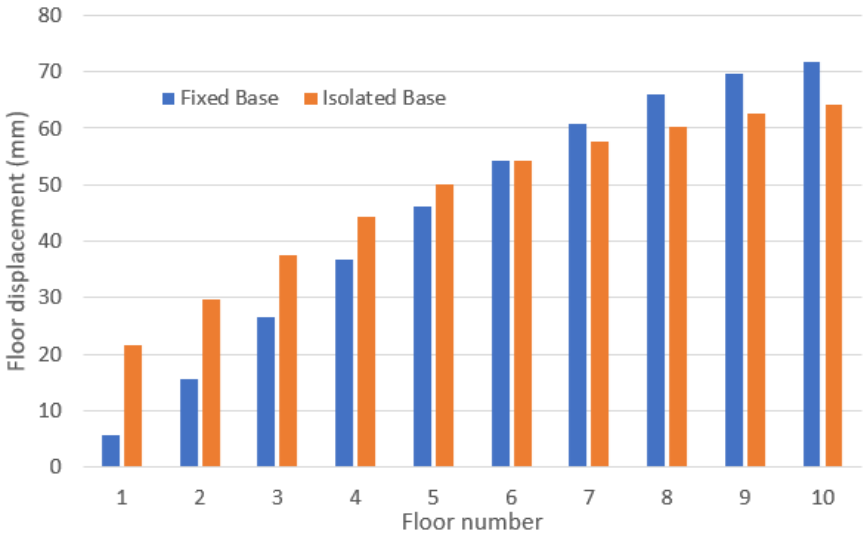

Fig. 9. Floor displacements for hard rock (S_A).

Table 6. Variation of floor displacement for hard rock (S_A).

Floor number	Floor displacement for FB (mm)	Floor displacement for IB (mm)	Difference (%)
1	5.59	21.70	288.02
2	15.70	29.81	89.91
3	26.51	37.46	41.32
4	36.82	44.41	20.62
5	46.13	50.05	8.50
6	54.20	54.30	0.19
7	60.86	57.57	-5.41
8	66.02	60.31	-8.64
9	69.64	62.63	-10.07
10	71.85	64.27	-10.54

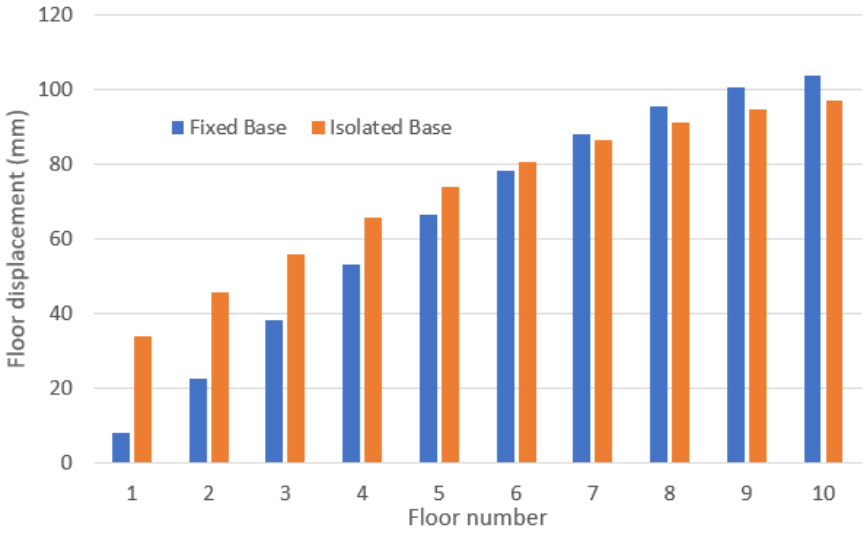

Fig. 10. Floor displacements for medium soil (S_C).

Table 7. Variation of floor displacement for medium soil (S_C).

Floor number	Floor displacement for FB (mm)	Floor displacement for IB (mm)	Difference (%)
1	8.08	33.90	319.62
2	22.67	45.57	100.96
3	38.29	56.09	46.48
4	53.18	65.69	23.52
5	66.63	73.9	10.97
6	78.29	80.75	3.15
7	87.91	86.40	-1.72
8	95.36	91.09	-4.48
9	100.59	94.72	-5.84
10	103.78	97.12	-6.41

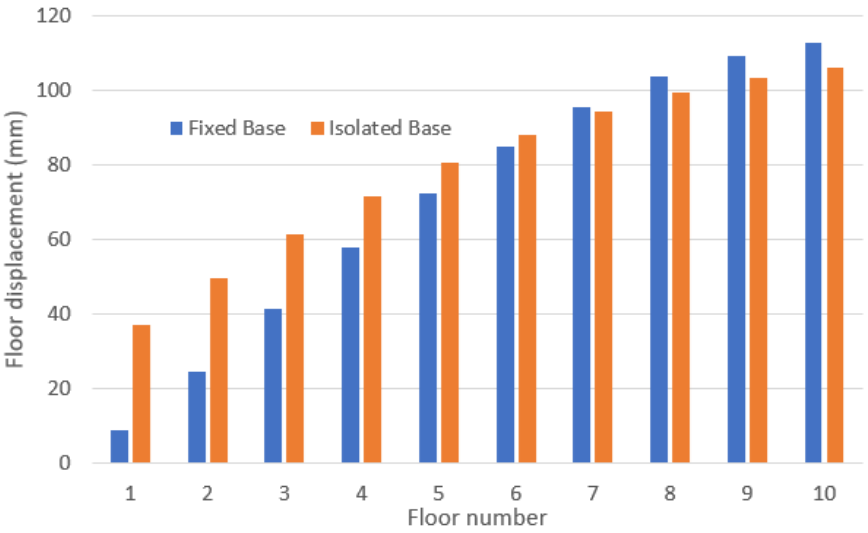

Fig. 11. Floor displacements for soft soil (S_E).

Table 8. Variation of floor displacement for soft soil (S_E).

Floor number	Floor displacement for FB (mm)	Floor displacement for IB (mm)	Difference (%)
1	8.77	37.15	323.48
2	24.62	49.83	102.38
3	41.58	61.23	47.25
4	57.75	71.66	24.08
5	72.36	80.69	11.51
6	85.02	88.21	3.75
7	95.47	94.45	-1.07
8	103.56	99.58	-3.84
9	109.24	103.50	-5.26
10	103.78	97.12	-6.41

4.2. Story shear

Fig. 12 shows the maximum story shear results for both conditions of isolated base (IB) and fixed base (FB) for soil SA for time history analysis in X direction, and due to the symmetry of the building the THA results is the same for both X direction and Y direction. Fig. 13 shows the same but for medium soil S_C and Fig. 14 for soft soil S_E.

According to UBC-97, the total base shear by using manual equivalent static method shall be calculated as Eq. (1). It shall not be less than Eq. (2) and greater than the result of Eq. (3).

$$V = \frac{C_v I}{R T} W \quad (1)$$

$$V = 0.11\, C_a\, I\, W \quad (2)$$

$$V = \frac{2.5\, C_a\, I}{R} W \quad (3)$$

UBC-97 provides two methods to calculate the period of building, either by using the simple quick equation Eq. (4), which only requires to know the building height and lateral force resisting system, or by using a more detailed equation Eq. (5), which needs stiffness of building and it depends on the rational analysis such as the Rayleigh's method.

$$T_a = c_t(h^{0.75}) \quad (4)$$

$$T_b = 2\pi\sqrt{(\sum_{i=1}^{n} w_i \delta_i^2) \div (g \sum_{i=1}^{n} f_i \delta_i)} \quad (5)$$

Table 9 shows the final results from applying Eqs. (1-4) for each soil type.

Table 9. Hand calculation of the total base shear.

W (dead + superimposed dead load)	56737.50 kN
C_t	0.0731
h	30 m
T_a	0.93 second
V manual, hard soil S_A	1722.58 kN
V manual, medium soil S_C	3229.90 kN
V manual, soft soil S_E	6007.50 kN

From Table 9, it can be noticed that using hand calculation equivalent static method to find the total base shear will produce larger values than that from using time history analysis for all types of soils, and this value will appear obviously in the soft soil type. Thus, when using time history method in the design against earthquake calibration factor should be used to make the final base shear which calculated from time history method is equal to that from equivalent static method, to be conservative by using high value of force in the design process.

Also, it can be seen in Figs. 12, 13 and 14 that increase the soil stiffness will decrease the floor shear due to earthquake, and that's produce another confirmation for the previous advice to construct structures on a strong soil to reduce the cost of building. Moreover, the largest story shear is in the top of the building. Thus, putting plastic water tanks on the roofs shall be avoided.

The isolated base building story shears are smaller than those obtained from fixed base building as shown in the figures.

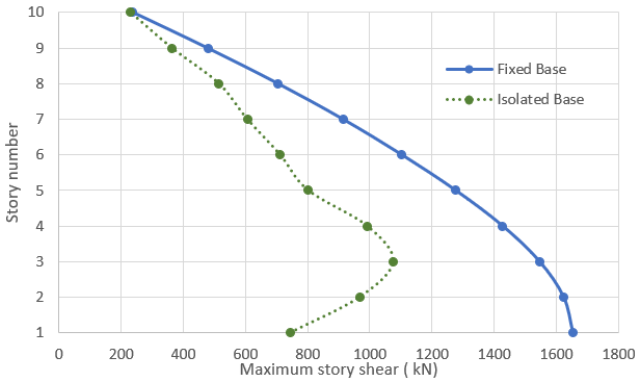

Fig. 12. Maximum story shear for strong soil (S_A).

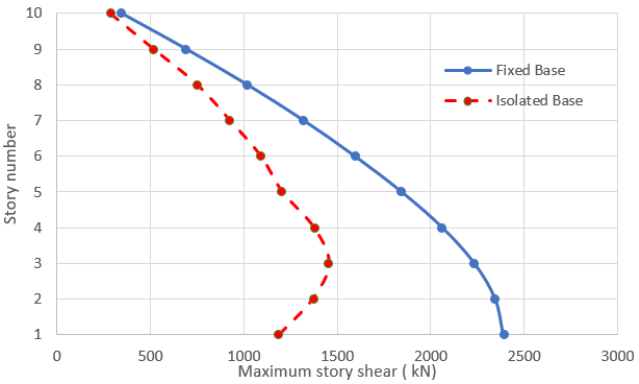

Fig. 13. Maximum story shear for medium soil (S_C).

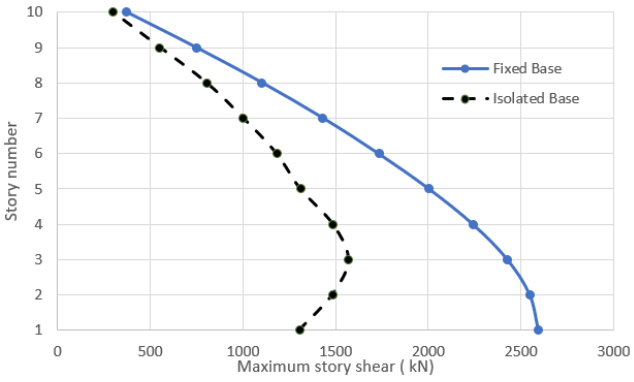

Fig. 14. Maximum story shear for weak soil (S_E).

4.3. Spectral acceleration

The maximum ground acceleration that occurred during ground motion at a site is called the peak ground acceleration (PGA) (Hassan et al., 2018).

During the earthquake the largest absolute acceleration amplitude recorded on an accelerogram at a studied location equals the PGA. Earthquakes usually occur in all three directions (Hatami, 2015). So, PGA can be components in horizontal and vertical. In general, the horizontal PGAs direction are larger than the vertical direction. Therefore, in engineering applications, the peak horizontal acceleration (PHA) is the most frequently used.

Fig. 15 shows isolated base building spectral acceleration for the three cases of soil: hard, medium, and soft for 0.05 damping ratio. It can be noticed that the maximum spectral acceleration values can be produced by soft soil and this will give maximum shear force in building. The maximum values of spectral acceleration are 1545.29 mm/second^2, 2155.10 mm/second^2 and 2304.52 mm/second^2 for hard soil, medium soil, and soft soil respectively.

As it is seen in Fig. 16, it is found that the increasing percentage of spectral acceleration values obtained by considering the hard soil condition is 39.46% when comparing to the medium soil condition, and 49.13% when comparing to the soft soil condition. So, as it is found, the soft soil condition produces higher acceleration as compared to other type of soils.

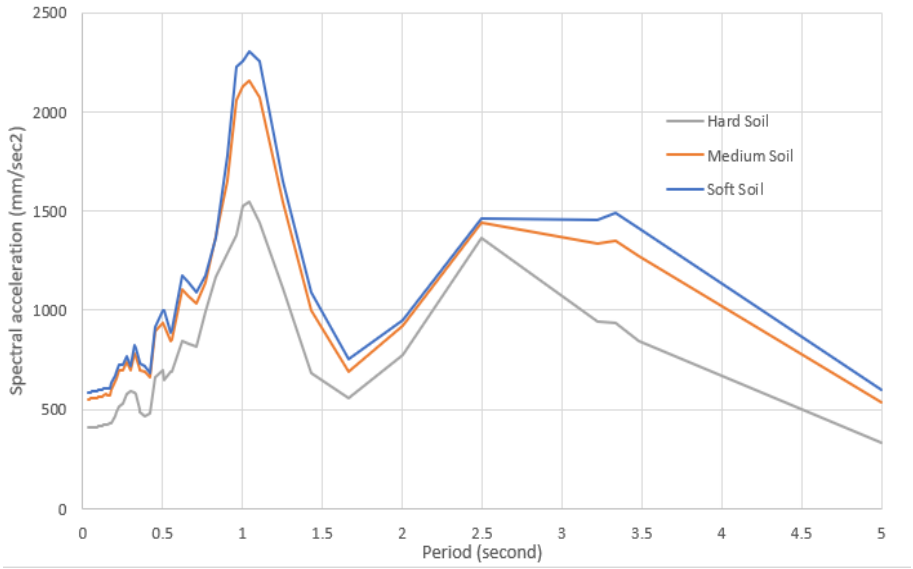

Fig. 15. Spectral acceleration.

Figs. 16, 17 and 18 show comparison between isolated and fixed base building in term of maximum values of spectral acceleration for three cases of soil. In these figures the maximum values of spectral acceleration for isolated and fixed base respectively are; 1545.29 mm/s^2, 3150.91 mm/s^2 in case of hard soil, and 2155.10 mm/s^2, 4551.32 mm/s^2 in case of medium soil. The increasing in spectral acceleration will be in the case of soft soil, the values are 2304.52 mm/s^2 for isolate base condition and 4942.61 mm/s^2 for fixed base condition. As it is noticed in the three cases of soil, the fixed base model's spectral acceleration values are greater than that in isolated base models. Thus, the design base shear of fixed base building will be larger than isolated base building.

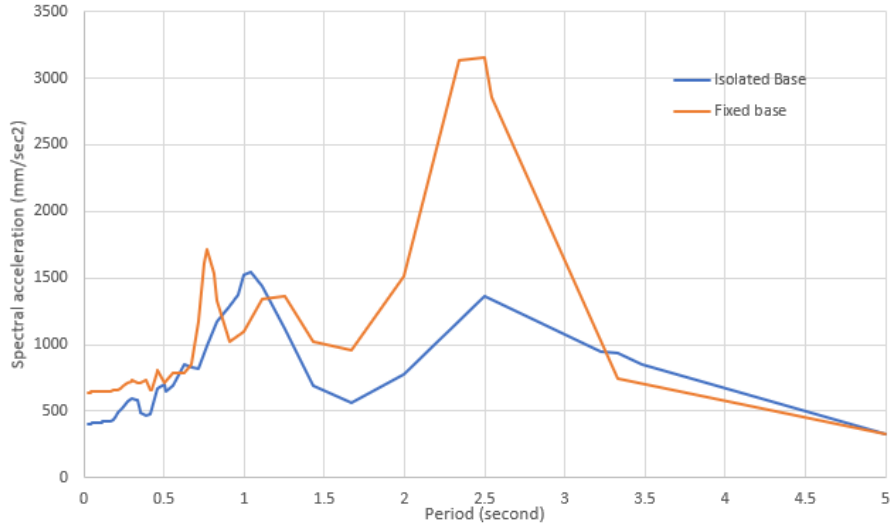

Fig. 16. Spectral acceleration for hard soil.

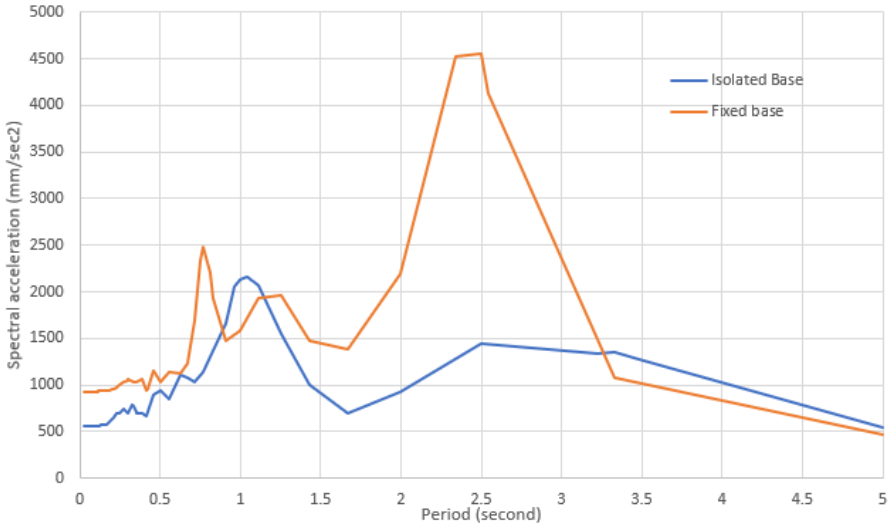

Fig. 17. Spectral acceleration for medium soil.

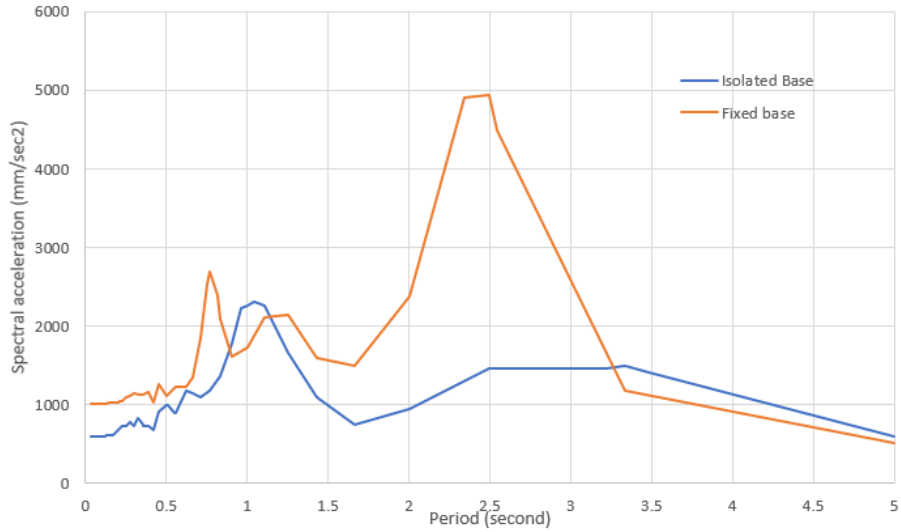

Fig. 18. Spectral acceleration for soft soil.

5. Conclusions

This study is an investigation in the seismic performance of an isolated and fixed base regular buildings under different soil conditions according to UBC-97. 10-floors high-rise building with an isolated base and fixed base has been studied for three types of soil: hard, medium and soft soil conditions according to UBC-97 code. Nonlinear time history analysis has been carried out using ETABS16 software and Izmit 1999 earthquake. Story displacements, story shear force and roof spectral acceleration have been studied. The main results and conclusions in this study as follows:

- Story shear force value increases when the soil stiffness decreases. It is found that the value of shear force will be the highest for soft soil and the lowest for hard soil type.
- Using equivalent static method will produce a total base shear larger than that by using time history analysis, and this appears clearly when reducing the stiffness of the soil.
- When using time history method in the seismic design, calibration factor shall be used to make the final base shear value from time history method equaled to that from equivalent static method.
- The roof level spectral acceleration of an isolated base model increases in medium soil condition by 39.46% and 49.13%in soft soil condition when compared with hard soil.
- Soft soil conditions produced the largest displacement compared with hard soil and medium soil.
- The first-floor lateral displacement value will be more than that of the fixed base building when using base isolated buildings. But if you move away from the foundations, the lateral displacement of floors of fixed base will be larger than that of the base isolated buildings, and this trend is the same for all types of soil cases.
- When using base isolated building, the drift of lower floors will be larger than that of the case of base isolated; but in the upper floors the drifts of fixed base building will be larger than that of the isolated base building.

REFERENCES

Alnajajra H, Touqan A (2017). The effect of reducing superimposed dead load on the lateral seismic deformations of structures. *International Journal of Civil and Environmental Engineering*, 11, 1587–1593.

CSI (2017). CSI Analysis Reference Manual. Computers and Structures Inc., Berkeley.

Gjorgjiev I (2012). Effects of soil medium on response of base isolated multistory frame structures. *15th World Conference on Earthquake Engineering*, Lisbon, Portugal.

Hassan A, Pal S (2018). Effect of soil condition on seismic response of isolated base buildings. *International Journal of Advanced Structural Engineering*, 10, 249–261.

Hatami F (2015). Effects of soil-structure interaction on the seismic response of base isolated in high-rise buildings. *International Journal of Structural and Civil Engineering Research*, 4(3), 237–242.

Jayalekshmi BR, Chinmayi HK (2016). Effect of soil stiffness on seismic response of reinforced concrete buildings with shear walls. I*nnovative Infrastructure Solutions*, 1(1), 2.

Kelly J, Naeim F (1999). Design of Seismic Isolated Structures, 1st edn. John Wiley & Sons Inc., USA.

Magade SB, Patankar JP (2008). Effect of soil structure interaction on the dynamic behavior of buildings. *Second International Conference on Emerging Trends in Engineering (SICETE). IOSR Journal of Mechanical and Civil Engineering*, Pune, 9–14.

Sayani PJ, Ryan KL (2009). Comparative evaluation of base-isolated and fixed-base buildings using a comprehensive response index. *Journal of Structural Engineering*, 135(6), 1141–1160.

Touqan AR (2008). Three dimensional response spectrum soil structure modeling versus conceptual understanding to illustrate seismic response of structures. *2008 Seismic Engineering Conference Commemorating the 1908 Messina and Reggio Calabria Earthquake*, American Institute of Physics.

UBC-97 (1997). Uniform Building Code: Structural Engineering Design Provisions. *International Conference of Building Officials*, Whittier, California.

Challenge Journal of Structural Mechanics

Case Study

Structural performance of URM school buildings during the 2019 Albania earthquakes

Marjo Hysenlliu [a], Huseyin Bilgin [b,*], Altin Bidaj [a], Marsed Leti [b]

[a] *Department of Civil Engineering, Polytechnic University of Tirana, 1000 Tirana, Albania*
[b] *Department of Civil Engineering, Epoka University, 1032 Tirana, Albania*

ABSTRACT

This paper aims to study the seismic performance of school buildings, which have been built in accordance with template unreinforced masonry [URM] school projects in Albania. For this purpose, the most widely used two template designs which were damaged during the 2019 Durrës (Albania) Earthquakes, have been selected. Analytical models of each school were prepared following the experimental data on the quality of the masonry constitutive components of the selected school buildings. Geotechnical investigations were deployed to obtain the soil characteristics of the area where the schools' foundation are located. Nonlinear static analyses have been performed to obtain the seismic capacity, the performance point and the damage level states. The performance-based method has been used to that purpose. The detailed examination of capacity curves and performance evaluation identified deficiencies and weak parts of the school building blocks. Results have shown that existing school buildings constructed pre-modern codes are far from satisfying the required performance criteria, suggesting that urgent response and necessary measure should be put into action.

ARTICLE INFO

Article history:
Received 22 April 2020
Revised 3 June 2020
Accepted 17 June 2020

Keywords:
URM school buildings
Seismic performance
2019 Albanian earthquakes
Non-linear static analysis
Template projects

1. Introduction

The school buildings play a crucial role in every society. These buildings should be earthquake resistant in earthquake-prone countries whose closure may cause disruption of community life and hampering education immediately after the earthquakes. Recent devastating earthquakes in Albania and in other countries such as Algeria, Greece, India, Iran, Italy, Morocco and Turkey in the world have underlined insufficient seismic performance of school buildings as found in OECD (2004), Bilgin (2015), Bilgin and Hysenlliu (2020).

Understanding the earthquake history of any place is important to recognize the possibility that an earthquake can affect the region again and to consider the extent of probable damage. While the latter is a function of the vulnerability of the built environment, the former notifies us of the predominant hazard, especially in regions with a history of earthquakes.

Throughout the history, earthquakes in Albania, like in many earthquake-prone countries worldwide, have seriously affected buildings causing numerous human casualties and economic loses as found in the work of Irfanoglu (2009), Magenes and Penna (2011), Yilmaz et al. (2013), Chaulagain et al. (2014), Mwafy and Elkholy (2016), Bilgin and Huta (2018), Estêvão et al. (2018). In this context, buildings' vulnerability is a key notion to focus on to reduce the consequences of catastrophic events. Generally, URM buildings present a worse seismic response as compared to reinforced concrete (RC) buildings due to the low strength and stiffness of their components.

Consequently, modern seismic guidelines include recommendations and commentaries aimed at reducing their seismic vulnerability. However, a significant part of masonry building stock has been constructed per pre-modern codes, thus considering unrestrictive requirements.

* *Corresponding author*. Tel.: +355-42-232086 ; Fax: +355-42-222177 ; E-mail address: hbilgin@epoka.edu.al (H. Bilgin)
ISSN: 2149-8024 / DOI: https://doi.org/10.20528/cjsmec.2020.04.006

The dominant building types in the Albanian building stock comprise URM structures with load-bearing masonry walls and buildings with RC framing system and infill baked clay and/or concrete walls. Moreover, mixed types are also observed. The majority of current buildings have been constructed according to the KTPs–Albanian Technical Codes, which were first issued and implemented as a legal provision in 1963 and last improved and updated in 1989 and still in force. Most of the existing masonry buildings in the country, like in many other European countries were designed considering earlier seismic codes (i.e. KTP-63, 1978; KTP-N2, 1989) when seismic loads were not required, or the design was to reduce the level of seismic loads. Nevertheless, its compliance requirements were not as explicit as those established by recent modern seismic codes like Eurocode 6 and Eurocode 8 from European practice. This led to a lack of seismic considerations in building's design process. In the meantime, the EN version of Eurocodes has been used for the design of structures in Albania since several years ago. Many industries and companies operating in civil engineering industry have introduced European norms in their products. Despite of this fact, according to the Albanian legislation in the field of construction, the design of structures still must follow the KTPs–Albanian Technical Codes. Therefore, Eurocodes are National Standards that can be used voluntarily as mentioned by Bilgin and Frangu (2017).

The URM structures with the load-bearing masonry walls suffered the most by the November 26, 2019 Durrës Earthquake due to reasons including old construction age, poor quality of construction, poor workmanship, interventions made by people, the design code of the time – if ever was applied- lack of maintenance and inadequate repair after previous damaging seismic events. This type suffered not only non-structural damage but also structural damage including partial or total collapse of the load-bearing masonry walls.

The object of this study, Shkolla 9-Vjeçare Publike "Emin Duraku" school blocks in Albanian capital city Tirana also suffered considerable damage during November 26, 2019 Durrës Earthquake sequences. In the on-site studies, the general condition of the buildings, the presence of observable settlements on the ground and the crack situation in the structure were determined and damage relieves were prepared. The data has been obtained from original blueprints and in-site visits to the buildings.

This study aims to evaluate the seismic performance of the typical low-rise existing masonry school buildings, constructed per pre-modern seismic codes of Albanian Construction practice. In order to reflect the properties of low-rise existing masonry buildings, two URM school buildings with template designs were selected and modelled by using the TREMURI, Lagormasino et al. (2013). Structural features such as member dimensions, material types and loading conditions of the buildings were determined from their architectural and structural designs projects and field investigations on investigated buildings in several cities of Albania. Mechanical characteristics were determined experimentally and adopted for nonlinear analysis. Nonlinear static (pushover) analyses have been performed to obtain the seismic capacities, the performance points and the damage level states according to Eurocode 8 by using 3MURI software.

2. Seismicity of Albania

Albanian neighborhood is in a rather complicated seismotectonic region and prone to earthquakes. A high frequency of earthquakes has been experienced, resulting in loss of life and property destruction in the region (Table 1).

Fault zones in Eastern Albania are mostly characterized by the influence of normal type faults. Most of them in directions of 325°-350°. The Western Albania fault zones are defined by reverse faulting– at the range of 40-50% stretching along the coastal shore (165°), while the appearance of strike-slip faults is in range of 15% of total tectonic activity (Fig. 1). Three longitudinal and two transverse active fault zones are evidenced in the region.

Table 1. Major earthquakes in Albania (after Aliaj et al. (2010)).

Date	Affected County	M_w	Depth (km)	Casualties	
				Dead	Injured
26/11/2019	Durrës	6.4	20.0	52	3000+
21/09/2019	Durrës	5.6	10.0	-	108
09/01/1988	Tirana	5.4	24.0	-	-
16 /11/1982	Fier	5.6	21.9	1	12
15/04/1979	Montenegro, Shkoder	6.9	10.0	136	1000+
30/11/1967	Diber	6.6	20.0	12	174
18 /03/1962	Fier	6.0	-	5	77
26/05/1960	Korçe	6.4	-	7	127
01/09/1959	Fier	6.2	20.0	2	-
27/08/1942	Diber	6.0	33.0	43	110
21/11/1930	Vlore	6.0	35.0	30	100
26/11/1920	Tepelena	6.4	-	36	102
06/01/1905	Shkoder	6.6	-	200	500

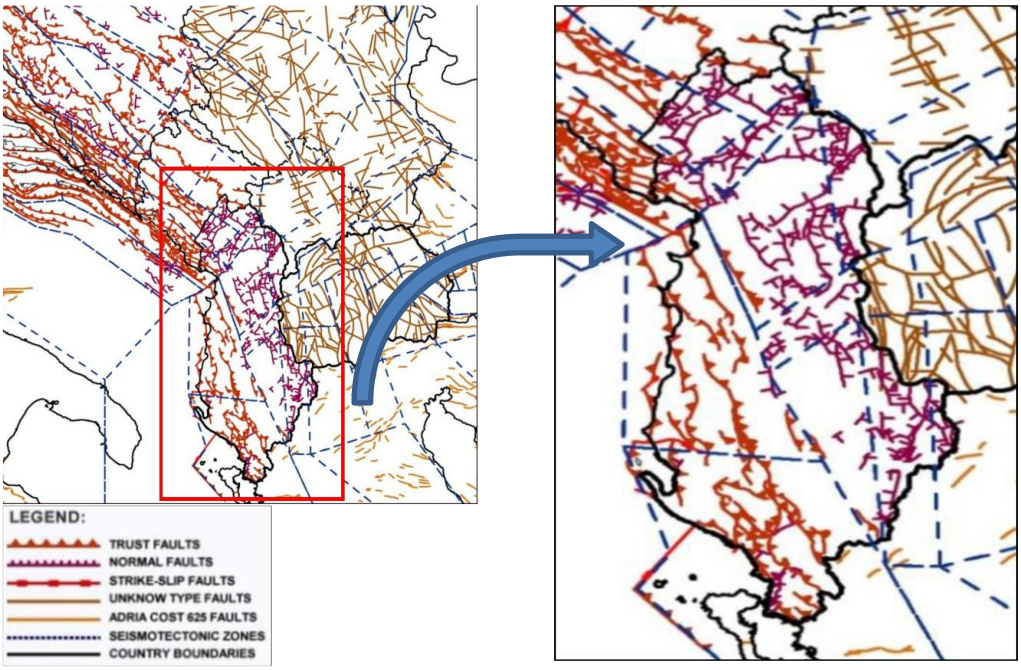

Fig. 1. From NATO SfP Project No. 983054 (BSHAP).

The 2019 earthquake affected area is dominated by NW-SE striking reverse active faults. The seismicity of Albania is characterized by an intensive seismic micro activity (1.0 < M ≤ 3.0), many small earthquakes (3.0 < M ≤5.0), rare medium-sized earthquakes (5.0 < M ≤ 7.0) and very seldom by strong earthquakes (M > 7.0).

2.1. The November 26, 2019 earthquake and its consequences on Albanian buildings

On November 26, 2019, an earthquake hit the central western part of Albania. It was assessed as M_w 6.4 (Fig. 2). Its epicenter was located offshore NW Durrës, about 7 km north of the city and 30 km west from the capital city of Tirana. Its focal depth was about 10 km [USGS, 2019].

Based on the focal plane solutions provided by several seismological institutes and observations, the main shock was generated by the activation of a NW-SE striking reverse fault. The main shock was felt in the neighboring Kosovo, Montenegro, Italy, Northern Macedonia and Greece, especially in Corfu Island. This was the second major earthquake to strike the region in the space of three months.

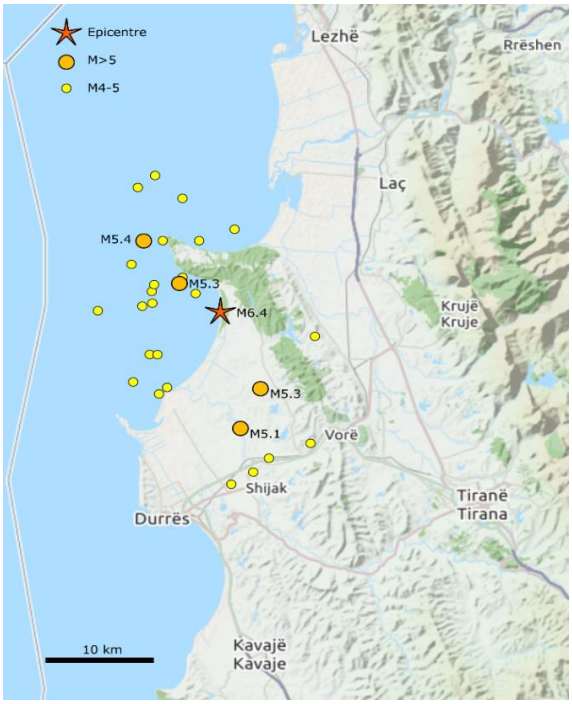

Fig. 2. Location of epicenter and aftershocks in the first twenty days of the 26 November Earthquake.

As regards the impact on the current building stock, the main shock and the following aftershocks induced damage to buildings of Durrës, Tirana and several settlements of the broader area. The most earthquake-affected regions are found in the city of Durrës and the town of Thumanë at the central-western Albania. Damage was also observed in Laç town, Fushë-Krujë town, Kamëz as well as capital city, Tirana.

Building damage was concentrated along two ellipses, whose major axis is oriented generally NW-SE (Fig. 3). This direction coincides with the strike of the seismogenic fault as it is derived from the fault plane solutions provided by several seismological institutes and observatories (INGV, 2019; USGS, 2019).

Spectral response of the earthquake is given for 0.3s and 1.0s in Fig. 4.

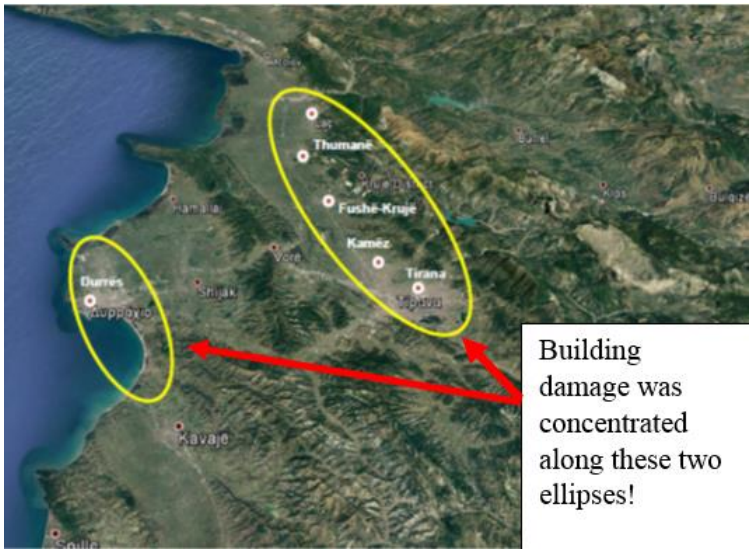

Fig. 3. Earthquake-affected area during the November 26, 2019 Durrës Earthquake.

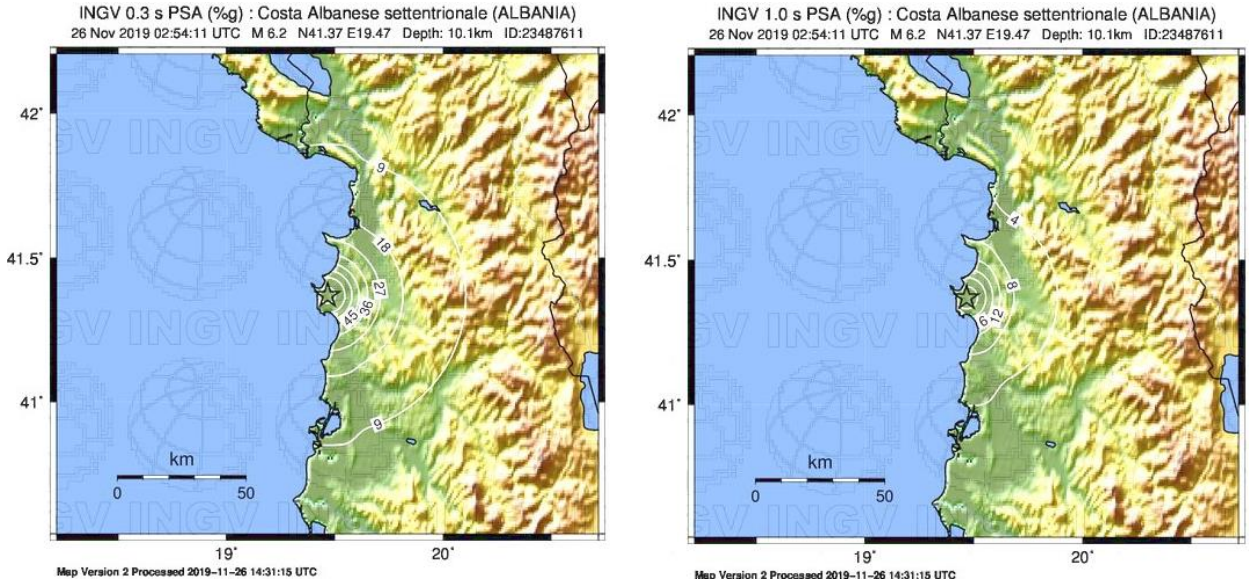

Fig. 4. Spectral response maps are given for 0.3s and 1.0 s for November 26 Earthquake. (http://shakemap.rm.ingv.it/shake/23487611/products.html).

2.2. Seismic hazard maps of Albania

Based on the seismic zonation map of Albania from the Earthquake Resistant Design Regulations, issued by the Seismic Center, Academy of Science of Albania, Department of Design, Ministry of Construction (1989), it is concluded that the resulted intensities from the earthquake under consideration, are within the limits specified in the Seismic Zonation Map (Fig. 5).

It is significant to note that the seismic zonation map in the seismic design code of Albania comprises zones based on observed seismic intensities and not on design accelerations.

On the other hand, based on the probabilistic approach, the seismic hazard maps for horizontal PGA, with the return period of 475 years, is shown for hard rock conditions (Fig. 6).

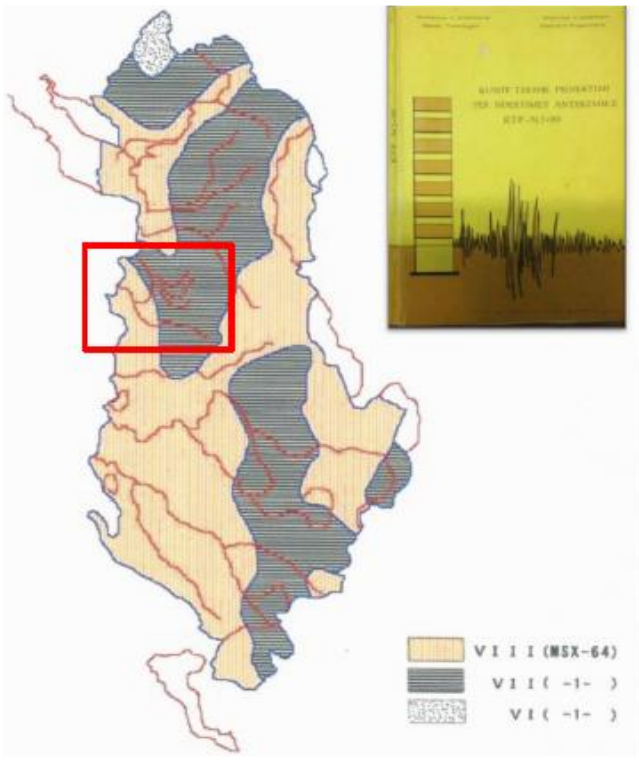

Fig. 5. Seismic zonation map of Albania.

3. Current Status of the School Buildings and the Load Bearing Systems of the Main Blocks and Its Adequacy according to the Earthquake Resistant Rules

The 9-vjeçare "Emin Duraku" school building blocks were built and located in the capital city of Tirana (Fig. 7).

Since the buildings under investigation are old ones, limited number of architectural drawings or details of the initial conditions of the buildings were reached. Only the original design plan of block B could be reached, and details of block A could not be found. Therefore, a detailed inspection of the existing structures was extracted. In these plans, the location and dimensions of the walls, windows and doors were determined. Based on the measurements obtained, structural floor plans of the existing structures were prepared, and structural models were developed accordingly for seismic analysis.

Building blocks were designed as two stories. But later, an additional story was added to both of them and became 3-stories due to the demand by time. So, buildings original designs were changed by these interventions. From the site survey and inspections, the floor plans of the blocks were generated and used for detailed seismic analysis.

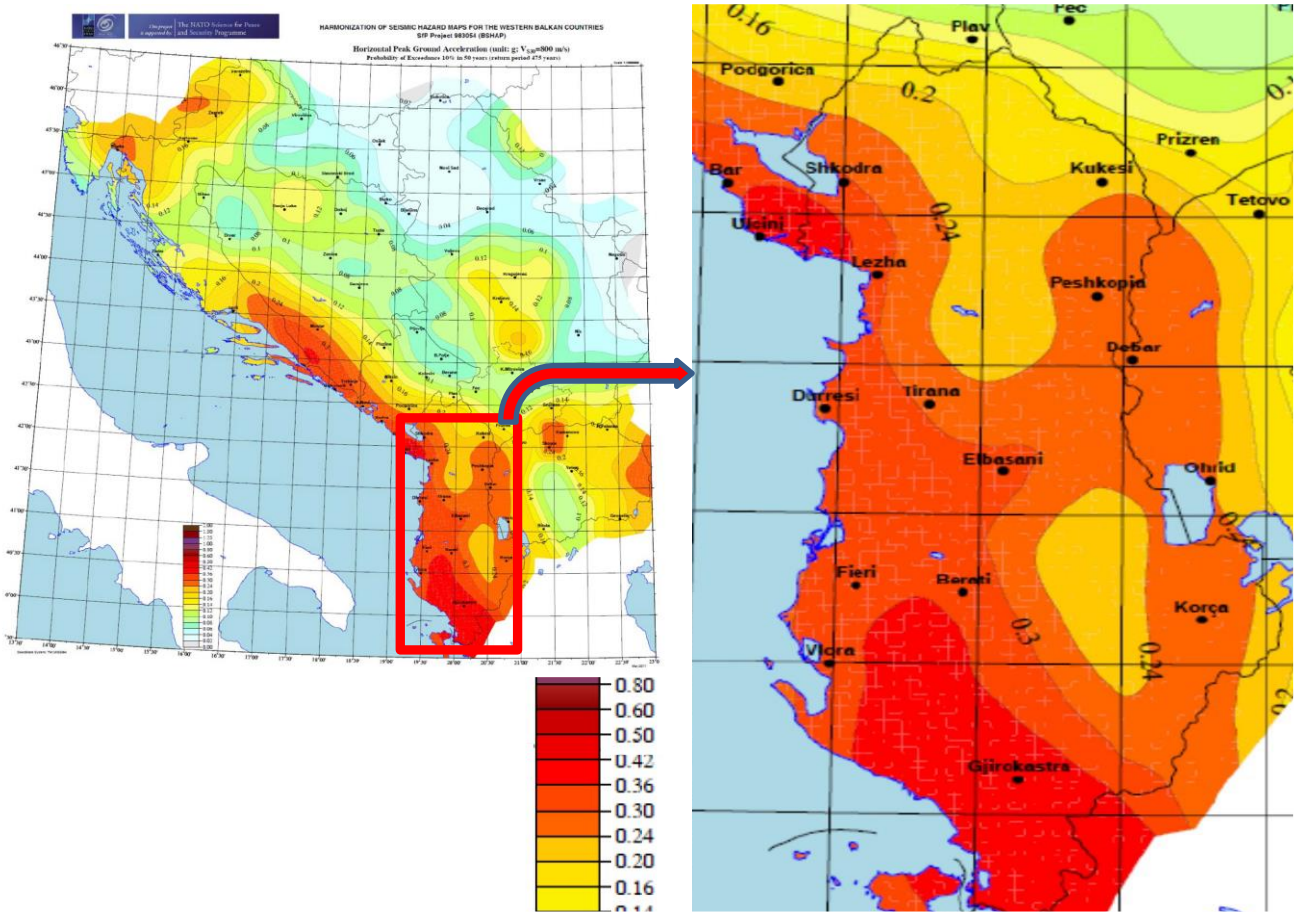

Fig. 6. Probabilistic seismic hazard map for horizontal PGA, with the return period of 475 years, for hard rock conditions (V_{s30} ≥ 800 m/sec) (from NATO SfP Project No. 983054).

(a)

(b)

Fig. 7. a) Front view of A Block; b) Front view of B Block and its intersection with A Block.

The expansion joint in the junction area of the old masonry structure (Block A) with the later added Block B structure is insufficient (Fig. 8).

The actual floor plans of the Blocks are given in Fig. 9.

In order to determine the type of wall material used in the masonry structures and the way the walls were built in the corner area, the cover layer was removed (Fig. 10). Lime mortar and solid clay bricks were used for wall construction in Block A and silicate bricks were used in Block B.

During the inspection inside the buildings, a considerable damage was observed on Block B. We observed a 45^0 inclined shear crack on a number of walls on the ground floor (Fig. 11). This structural crack was formed on the 45 cm thick wall, which was subsequently removed in the upper floors to make additional space, during the Durrës earthquake of 26 November 2019.

Fig. 8. Expansion joint between two buildings (11.55 mm < 30.00 mm).

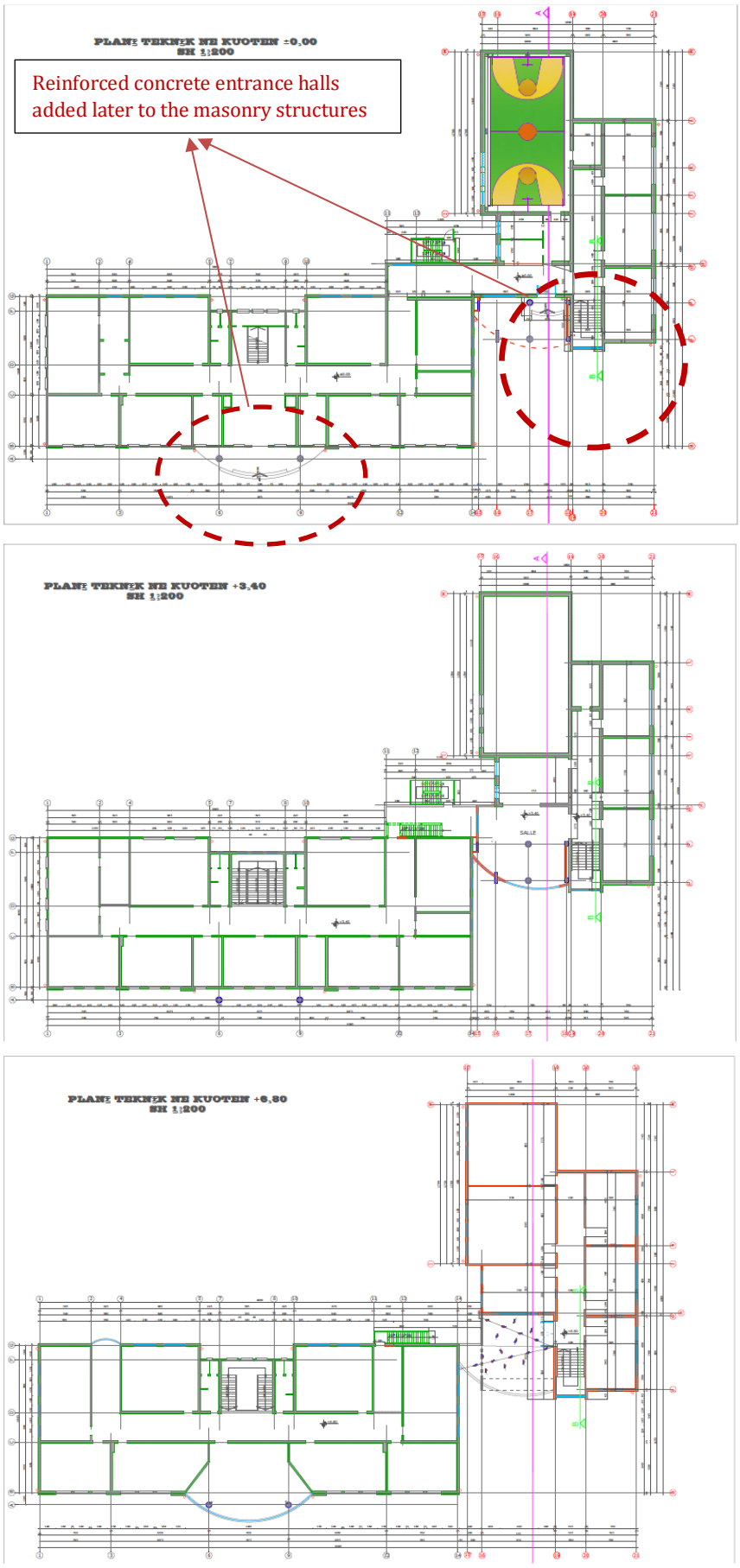

Fig. 9. a) Structural layout of Block A and B (ground floor), Reinforced concrete entrance halls added later to the masonry structures (shown by dashed red circles); b) Structural layout of Block A and B (1st floor); c) Structural layout of Block A and B (2nd floor).

a) Block A- Clay bricks b) Block B- Silicate masonry

Fig. 10. Type of bricks used for the school building blocks.

Fig. 11. Shear cracks on load bearing walls in the ground floor of the Block B.

In the structure, a reinforced concrete slab system was applied to the beams above the wall. It was realized that due to the thick coating applied as a covering material on the reinforced concrete slabs, the total weight of the structure was increased. In this way, due to overlapping floor coverings, the floor thickness in the structure has approached to ~25 cm. As a natural consequence of this, there is much higher load transfer from the slabs to the supporting walls than it should be.

According to modern earthquake codes in force (i.e. TSDC, 2018), "In masonry-masonry buildings, the height of each floor shall not be more than 3.0 m". It is observed that this condition was exceeded in this building.

In Block B, wall thicknesses range from 45 cm to 25 cm. Thicknesses vary between layers, even on the same floor. On the ground floor, the walls were applied in two different thicknesses: 45 cm and 25-30 cm. The outer walls on the ground and first floor are usually 45 cm. The wall thicknesses vary from 30 cm to 25 cm on the top floor. In Block A, the wall thicknesses vary between 38 cm and 25 cm and there is a more regular distribution in the level of the floor than Block B.

In the masonry structures, all the vertical and horizontal loads acting on the structure are carried by the load bearing walls and transferred to the foundation. For this reason, in the earthquake-resistant structure design regulations, it is stated that "The load bearing walls of masonry buildings shall be arranged as regularly as possible and symmetrical or close to symmetry with respect to the main axes".

So, in order to create different spaces in a masonry structure, the location and thickness of the walls should not be changed. Different walls should not be applied between the floors. However, as can be seen from the floor plans given in Fig. 12, different wall axes were applied between the ground floor, first floor and second floors in some parts of the structure. In this way, vertical discontinuities are created between the floors and all the loads coming from the upper floor wall are loaded onto the floor covering.

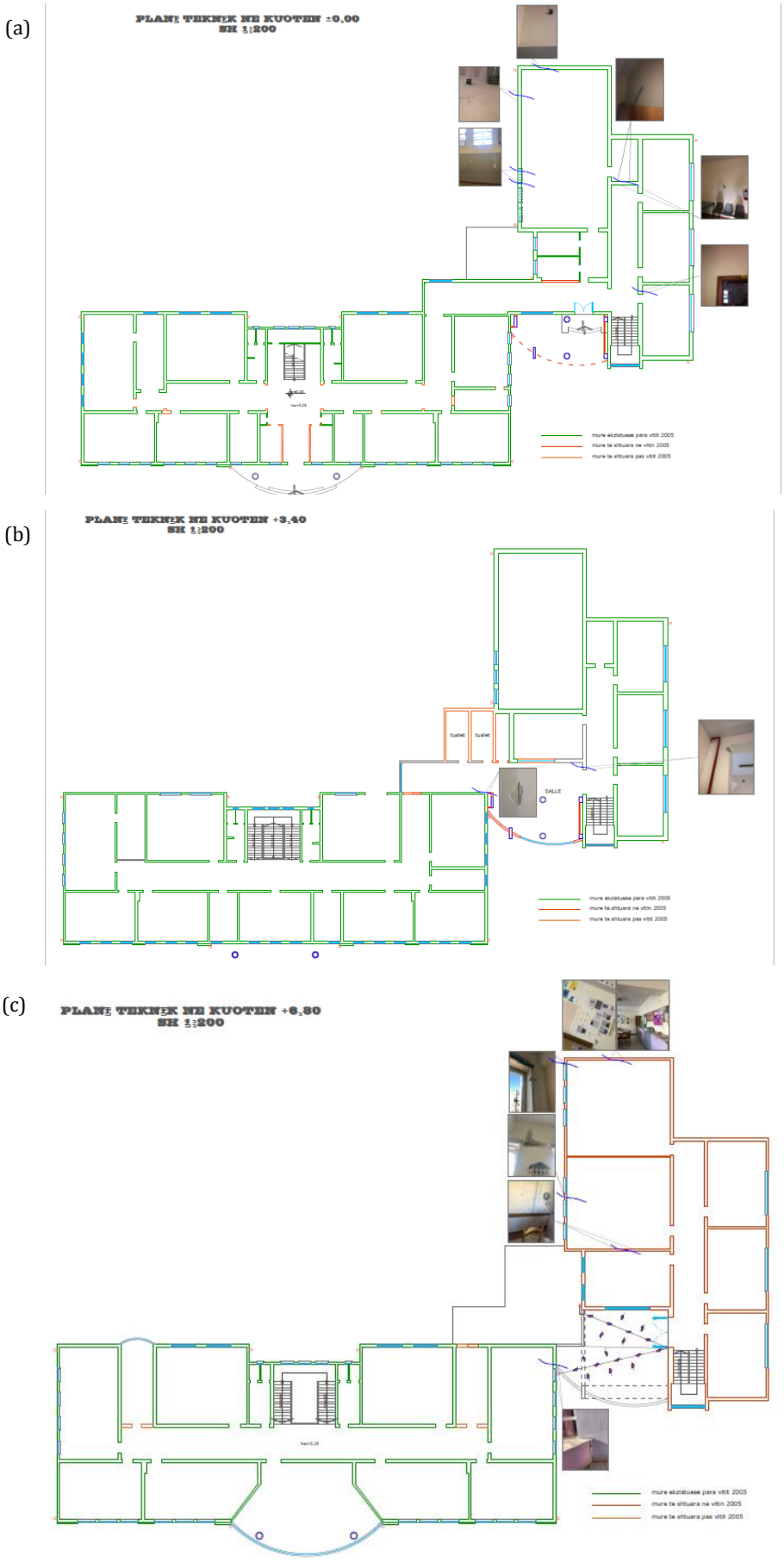

Fig. 12. a) Slight-moderate damaged locations on the ground floor; b) Slight-moderate damaged location on the 1st floor; c) Moderate-severe damaged locations on the 2nd floor of the Block B (This floor was added lately and made the building more vulnerable during 26 November earthquake.

In modern earthquake regulations (i.e., EC 8; TSDC 2018), it should be noted that in the masonry structures, the plan length of the wall part to be left between the window or door space closest to the building corner should not be less than 1.5 m in the 1st and 2nd degree earthquake zones and 1.0 m in the 3rd and 4th degree earthquake zones. As can be seen in Fig 6, this requirement in Block B is not satisfied in many locations. For example, at the corners this value is measured as 0.5 meter << 1.5 meters. An important detail to note in Fig. 9 is that the window locations and wall axes are variable between the floors. However, in masonry structures, the axes of the walls must be the same between the floors. In addition, the positions of the windows between the floors should not be shifted.

On the last floor, it was observed that the beams were located on the spandrels in the middle of the windows (Fig. 13). During the earthquake, this caused serious damage in the inner and outer part of the connecting areas. They should have been cast on the pier elements to safely convey the slab and roof loads to the foundation.

Apart from the corners of the building, the length of the filled wall pieces between the window and door spaces in the plan was determined. According to the modern seismic codes in practice, it is suggested that the length of the masonry wall between the two openings cannot be less than 1.0 m in the 1st and 2nd degree earthquake zones and 0.8 m in the 3rd and 4th degree earthquake zones. It was determined that this value decreased up to 60 cm in Block B which does comply the requirements. This application was made on the top floors, especially on the exterior.

(a)

(b)

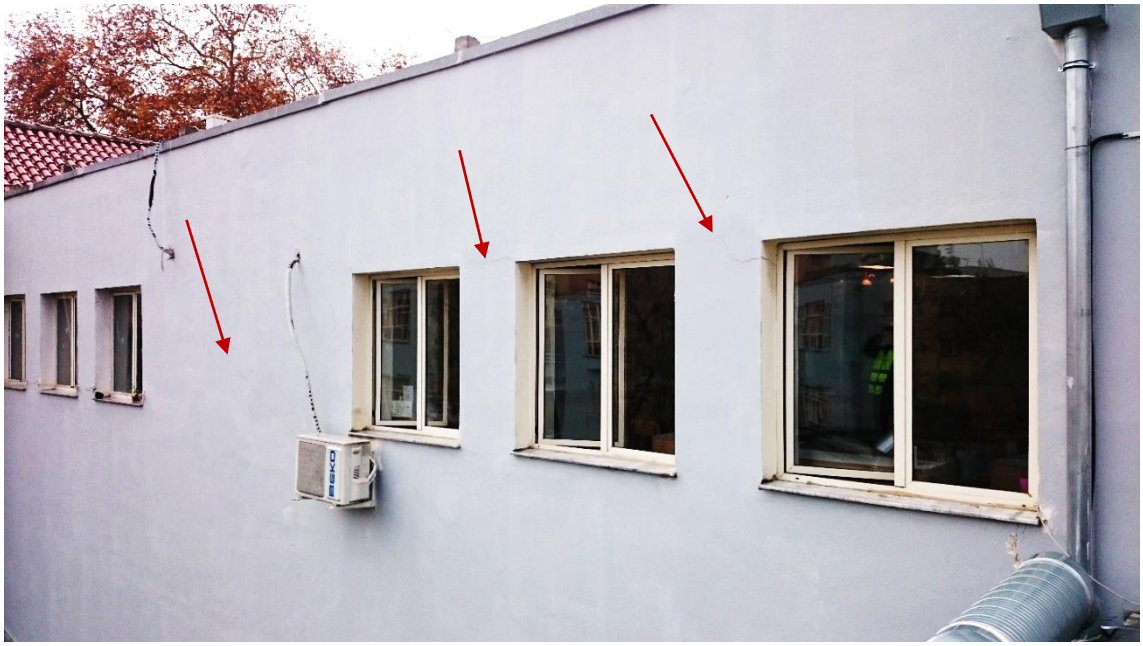

Fig. 13. a) A beam casted on spandrel over a window in the last floor of Block B and caused serious damage; b) Diagonal shear cracks on outer façade of the last story. This damage patterns also continue in the inner part.

The evaluation of the building blocks is based on conceptual earthquake-resistant design rules in modern earthquake regulations. These rules are summarized and listed in Table 2. As a result of the on-site inspections and measurements, the compliance of the buildings with the earthquake resistant design regulations is evaluated in the same table.

Table 2. Suggested earthquake resistant design rules for masonry buildings and the adequacy of the school blocks (Following EC-8 and TSDC, 2018).

	Provision	Limit	Current status of the buildings	Adequacy
1	Number of floors for masonry buildings can be maximum 2 in 1st Degree Earthquake Zones	2	Both Block A and B are 3 floors. Their original design projects (projected as 2-stories) were intervened by adding one additional floor.	Inadequate
2	In masonry buildings, the height of each floor shall not be more than 3 m above the floor.	3 m	For both blocks, story heights are more than 3 meters.	Inadequate
3	The load bearing walls of the masonry buildings shall be arranged as regularly as possible in the plan and symmetrical or symmetrical to the main axes.	As much as possible	Although orientation of the walls and the axes are symmetric or close to symmetry in Blok A, the plan orientation of the walls and the continuation has some discontinues over the height of the building on Block B.	Inadequate for Block B. A could be considered as adequate.
4	All bearing walls shall be constructed on top of each other in the plan.		The underneath of some load bearing walls remained empty. There are discontinuities in the floor height, especially in Block B.	Inadequate. Block A is regular.
5	Natural stone, filled bricks, filled concrete briquettes or similar blocks will be used as masonry materials in the construction of bearing walls.		Clay bricks and silicate brick were used as load bearing material.	Adequate
6	Natural stone load bearing walls will be used only in foundations and ground floors of masonry buildings.		The building is not made of stone with walls.	Adequate
7	In the 1st degree earthquake zones, natural stone load bearing walls shall be at least 50 cm in the foundation and ground floor.	50 cm	70 cm > 50 cm	Adequate
8	The unrestrained length of any load bearing wall between the axis of the load bearing wall perpendicular to the plan shall not exceed 5.5 m in the 1st degree earthquake zone and 7.0 m in other earthquake zones.	5.5 m	On the upper floors, this length can reach up to 5.5 meters and more.	Inadequate
9	In the case of masonry structures, additional measures should be takenif the following condition is not met in one direction. L_d / A> 0:25 * I; I: Building Importance Coefficient (1.5 for Schools)	0.25*1.5= =0.375	This value is very low especially in the last floors	Inadequate
10	The length of the solid wall part to be left between the window or door space closest to the building corner shall not be less than 1.5 m in the 1st and 2nd seismic zones and 1.0 m in the 3rd and 4th seismic zones.	1.0-1.5 m	The length of this filled wall section decreases up to 60 cm in places, especially on the upper floors of Block B.	Inadequate
11	Apart from the corners of the building, the length of the solid wall pieces between the window and door spaces shall not be less than 1.0 m in the first and second seismic zones and 0.8 m in the third and fourth seismic zones.	1.0 m	The distance between the two openings decreases up to 31 cm.	Inadequate
12	Apart from the corners of the building, the length of the full wall piece to be left between the window or door space closest to the intersection of the walls intersecting each other and the intersection of the walls shall not be less than 0.50 m in all earthquake zones.	0.50 m	This value is lower than 50 cm especially in upper floors.	Inadequate
13	The length of each door and window opening in the plan shall not be more than 3.0 m.	3.0 m	There are openings reaching up to 4.0 meters in Block B.	Inadequate
14	Eurocode-8 Part-3 (EC8-3) establishes that URM buildings can only be constructed in areas of low seismicity (a_g<0.08g) (where a_g is the EC8 design acceleration)		Nearly all the municipalities located around Tirana have higher values of a_g, greater than 0.15g.	Inadequate

4. Seismic Capacity Evaluation of the School Buildings Blocks

The pushover analysis consists of the application of gravity loads and a representative lateral load pattern. Gravity loads were in place during lateral loading. In all cases, lateral forces were applied monotonically in a step-by-step nonlinear static analysis. The applied lateral forces were proportional to the product of mass and the first mode shape amplitude at each story level under consideration.

In pushover analysis, the behavior of structure is characterized by a capacity curve that represents the relationship between the base shear force and the displacement of the roof. This useful demonstration is very practical and can easily be visualized by practicing engineers. Roof displacement is commonly used for capacity curve.

4.1. Determination of the material and soil characteristics of the school buildings

For the modelling of the selected buildings two types of issues should be considered: correct representation of the mathematical model and inelastic characteristics of materials. URM is a composite construction material which consists of masonry units and mortar. Brick and stone are the usual elements of masonry units. Mortar is used to make the connection between these units. Under vertical and horizontal loads, load bearing of masonry considered as the assemblage of the masonry units and mortar is influenced by the compressive, shear and flexural strengths, durability, water absorption and thermal expansion.

These two structures are composed of two main components, namely load bearing walls and roof diaphragms. The walls are stiff with openings and the diagrams are usually constructed by RC slabs. For the construction of the Blok A, solid clay bricks with 250 mm x 120 mm x 60 mm dimensions connected with cement mortar are used to build the masonry walls. In order to achieve a better distribution of the loads, perimeter RC beams are used to create a better connection between slabs and load bearing walls. Block B was constructed by the calcium silicate solid bricks and cement mortar and Block A was constructed by solid clay bricks.

The load bearing walls are made with masonry walls that can be classified in facade with a thickness of 380 mm and inner masonry walls 250 mm thick. The thickness of outer load bearing walls has 380 mm for Block A and these values are 450 mm for Block B. Calcium silicate solid and solid clay bricks with 250 mm x 120 mm x 65 mm dimensions connected with cement mortar were used to build the masonry walls of the school blocks.

For the mathematical modelling and the seismic analyses of the school buildings, as built material properties determined from site investigations and experimental test were taken into consideration. In order to truly represent the strength and structural integrity of the buildings, mechanical characteristics were obtained from the experimental tests with destructive methods (Fig. 14). The samples were tested to determine the compressive strength of the solid bricks units and the obtained results are used for seismic analyses.

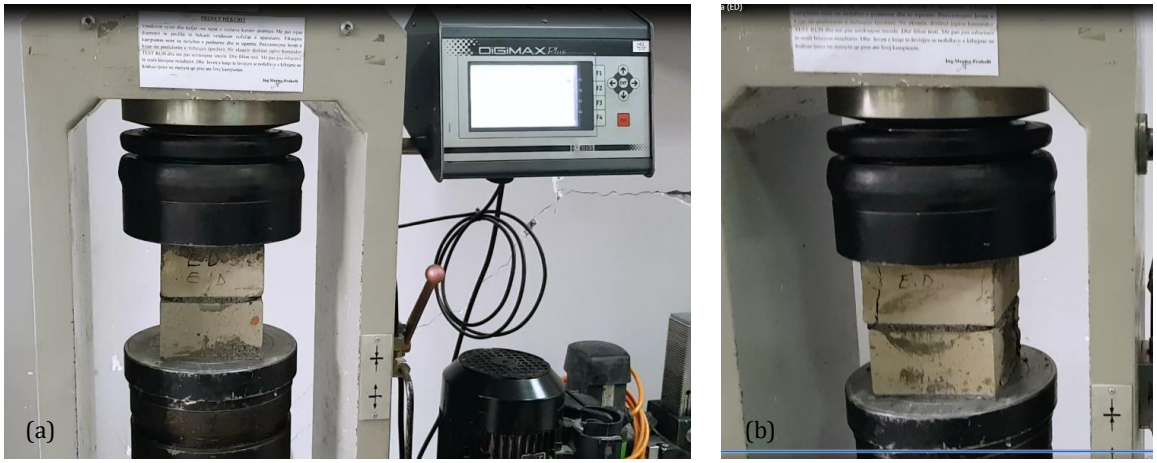

Fig. 14. a) Sample during testing; b) Sample after testing.

The characterization of masonry walls in existing buildings is complex. In this study, mechanical characteristics have been obtained by using the building codes, blueprints and the similar buildings constructed during the similar periods. In the case when experimental data is not sufficient, several equations are proposed by different codes and guidelines to calculate the compressive strength of the masonry walls. In this study, Eurocode 6 (2005) guideless are followed as given in Eq. (1);

$$f_k = K * f_b^{0.70} * f_m^{0.30} \text{ (MPa)} \quad (1)$$

Following the Eurocode 6 guidelines CEN (2005) together with the relevant material characteristics obtained from experimental tests are used to calculate the required input data for mathematical modeling of the buildings (Table 3).

Seismic loads are usually characterized by response spectrum functions which are derived from the time history records of past earthquakes in specific locations. To perform a reliable performance evaluation, seismic demands of the studied buildings were determined based on detailed seismic hazard assessment. A detailed soil

investigation was carried out in order to have a comprehensive understanding of the actual structural conditions for the area where both buildings are located. The boreholes were drilled, and the samples were analyzed. According to the geotechnical investigations, the type of soil that forms the foundation of the area is classified as "Dense gravel or medium dense sand and gravel" according to the laboratory test results that has an allowable load bearing capacity of 220 kPa (2.2 kg/cm^2).

According to the European norms (EC 8), the soil class of the unit is considered in the seismic analysis as Type C. In this study, the demand calculations for the seismic assessment of the considered buildings were performed considering the actual soil conditions with a moderate seismicity according to Eurocode 8. Elastic seismic demand spectra shape was given in comparison between Eurocode 8 and KTP-N2-89 (Fig. 15).

Table 3. Masonry wall data used as Input for analytical modeling.

Building Type	Compressive strength f_k (N/mm^2)	Mortar strength f_m (N/mm^2)	Tensile fracture energy G_t (N/mm)	Shear strength f_t (N/mm^2) as per EC 6	E (N/mm^2) as per EC 6	G (N/mm^2) as per EC 6	Poisson ratio ν
Block A	5.50	5.00	0.1	0.50	5500	1675	0.2
Block B	5.50	5.00	0.1	0.50	5500	1675	0.2

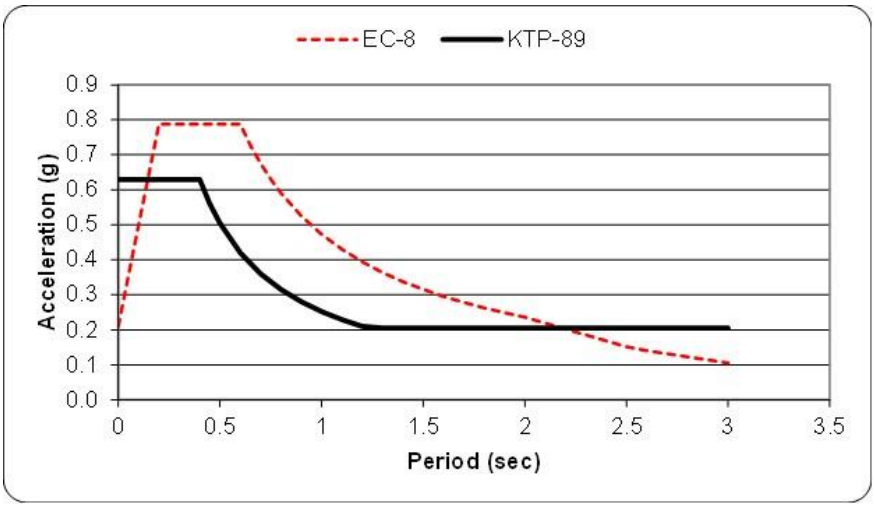

Fig. 15. Shape of the Elastic Acceleration Response Spectrum in EC-8 and KTP-N2-89 (Albanian Seismic Code).

4.2. Mathematical modeling

Modelling masonry structures is not an easy task due to the nonlinear response of masonry and lack of experimental data regarding the inherent characteristics of masonry structural elements. Masonry is a heterogeneous material composed of masonry bricks and mortar whose mechanical characteristics depend upon the inherent properties of its constituents. Its behaviour under different loadings may be very complex. In order to model the response of masonry, numerous assumptions and analytical models are proposed in Lourenço (2010). Each of these techniques requires the adoption of different constitutive models. Due to the complexity of the two case study buildings, several assumptions on the material properties and the necessity of having high performance computers to process the nonlinear analyses, macro-modelling technique was considered in this study. Nonlinear static analyses have been conducted by TREMURI software that is a multi-purpose finite element program dedicated for the linear and nonlinear analysis of masonry structures.

School building blocks are analysed considering 4 different cases. According to the 1st design, both blocks were constructed as two stories and later on depending on space demand for education, one additional story was added to both of the blocks. Currently, each building has 3 stories and Block B experienced moderate-severe damages during the November 26 Earthquake and Block A did not have a serious observed damage. To make a comparative performance assessment, actual status of each building (3-story) and the original designs (2-story) are modelled separately and seismic load bearing capacities are estimated. A 3-D model of each building typology is created in TREMURI to carry out pushover analyses (Fig.16).

During the modelling, the walls are the load bearing elements, while the floors are considered as stiffening elements, on which the lateral effects are distributed between the connected walls.

Damage limit states are quantitative definition of performance levels by a convenient damage indicator capable of representing the seismic performance with appropriate damage thresholds. They should be defined in

terms of quantitative measure of structural behavior such as displacements and deformation quantities. In this study, damage limit states were defined as suggested in Eurocode 8.

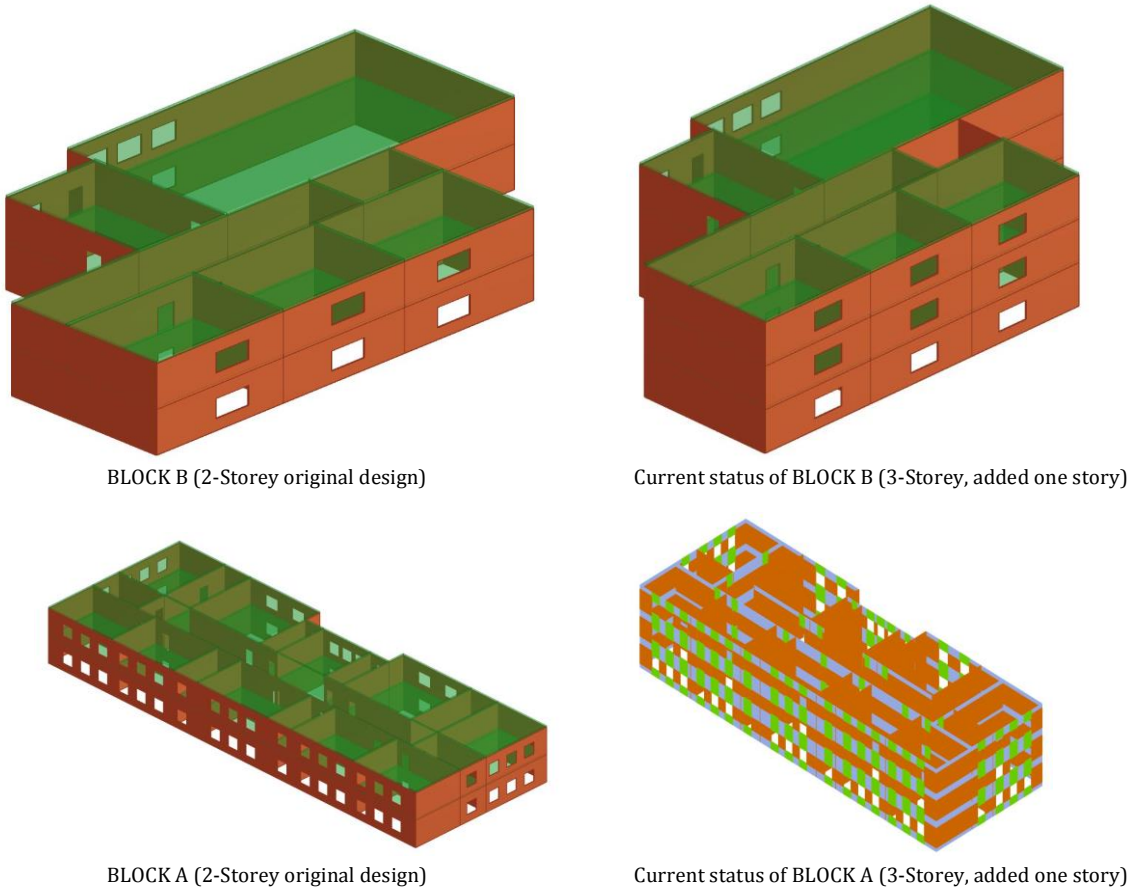

BLOCK B (2-Storey original design)

Current status of BLOCK B (3-Storey, added one story)

BLOCK A (2-Storey original design)

Current status of BLOCK A (3-Storey, added one story)

Fig. 16. 3D view of the school building mathematical models (3MURI software).

Capacity evaluation of the investigated buildings is performed using Eurocode 8. Three damage limit states levels, i.e., "Limited Damage" (LD), the limit state "Significant Damage" (SD) and the limit state "Near Collapse" (NC) are considered. Eurocode 8 approximates the base shear force-drift relationship of masonry piers by a bilinear curve.

4.3. Seismic analyses of Block B

4.3.1. 2-story model

The building is pushed by 24 different loading cases and the pushover curves are plotted for the most critical loading pattern (Fig. 17).

4.3.2. 3-story model (current status)

The building is pushed by 24 different loading cases and the pushover curves are plotted for the most critical loading patterns (Fig. 18).

Table 4 defines the PGA limits that can be sustained by building for the damage limit states according to EC 8 for Block B.

From the comparison of *2-* and *3-* story building performances of Block B, it can be revealed that the 3-story building has nearly 25-30% less load bearing capacity than the 2- story design. Pushover analyses results and the damage patterns observed during the damage inspection confirms the induced damage patterns during the November 26, 2019 earthquake.

4.4. Seismic analyses of Block A

4.4.1. 2-story model

The building is pushed by 24 different loading cases and the pushover curves are plotted for the most critical loading pattern (Fig. 19).

4.4.2. 3-story model

The building is pushed by 24 different loading cases and the pushover curves are plotted for the most critical loading pattern (Fig. 20).

Table 5 defines the peak ground acceleration (PGA) limits that can be sustained by building for the damage limit states according to EC 8 for Block A.

Similar to the Block B vulnerability, addition of one story caused a reduction to the seismic resistance of Block A. This reduction in seismic resistance (around 30%) can easily be observed from the comparisons PGA values.

(a)

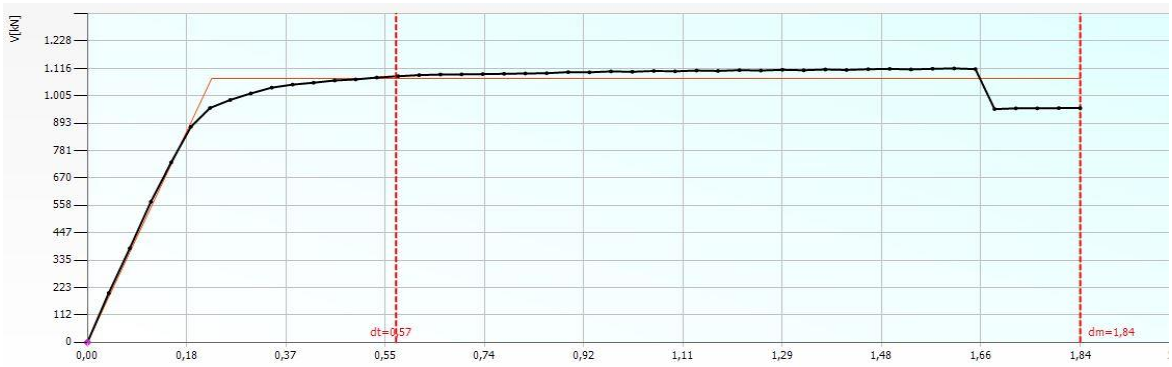

(b)

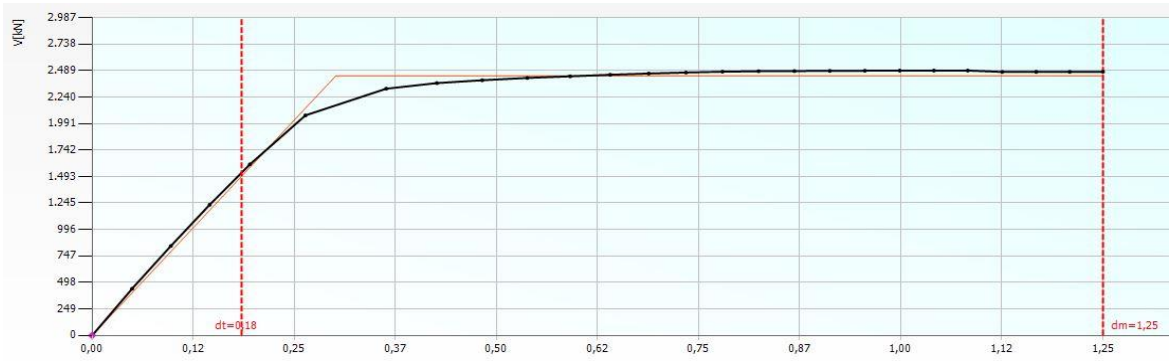

Fig. 17. Pushover curves of B Block_2-Story: a) *x*- direction; b) *y*- direction.

(a)

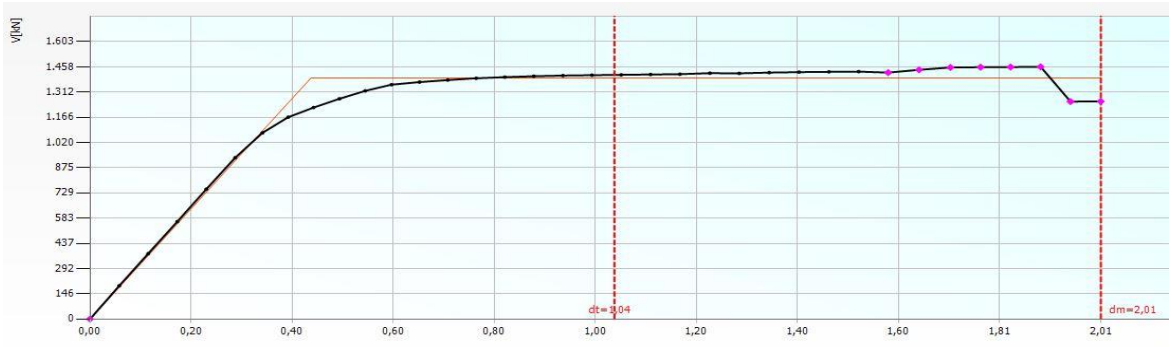

(b)

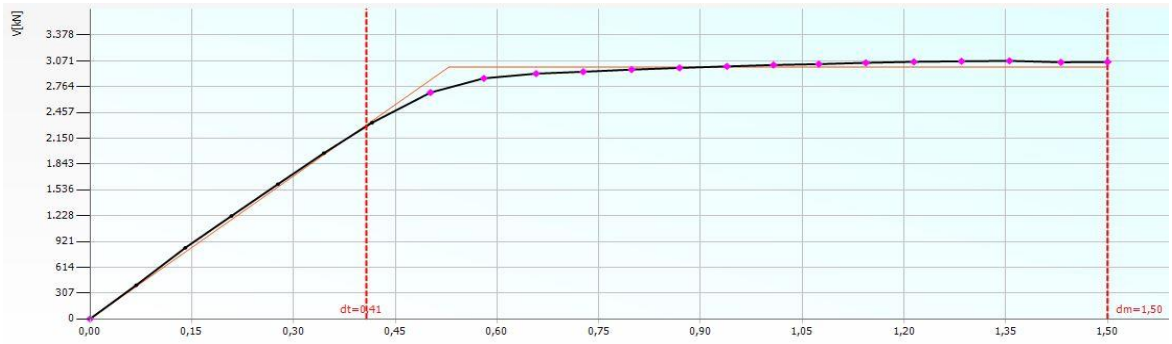

Fig. 18. Pushover curves of B Block_3-Story: a) *x*- direction; b) *y*- direction.

Table 4. PGA limit states for Block B.

Limit State	PGA (m/s²)			
	2-story		3-story	
	x-	*y*-	*x*-	*y*-
NC	2.947	3.880	2.139	2.823
SD	2.349	3.330	1.703	2.385
DL	0.856	2.110	0.777	1.688

(a)

(b)

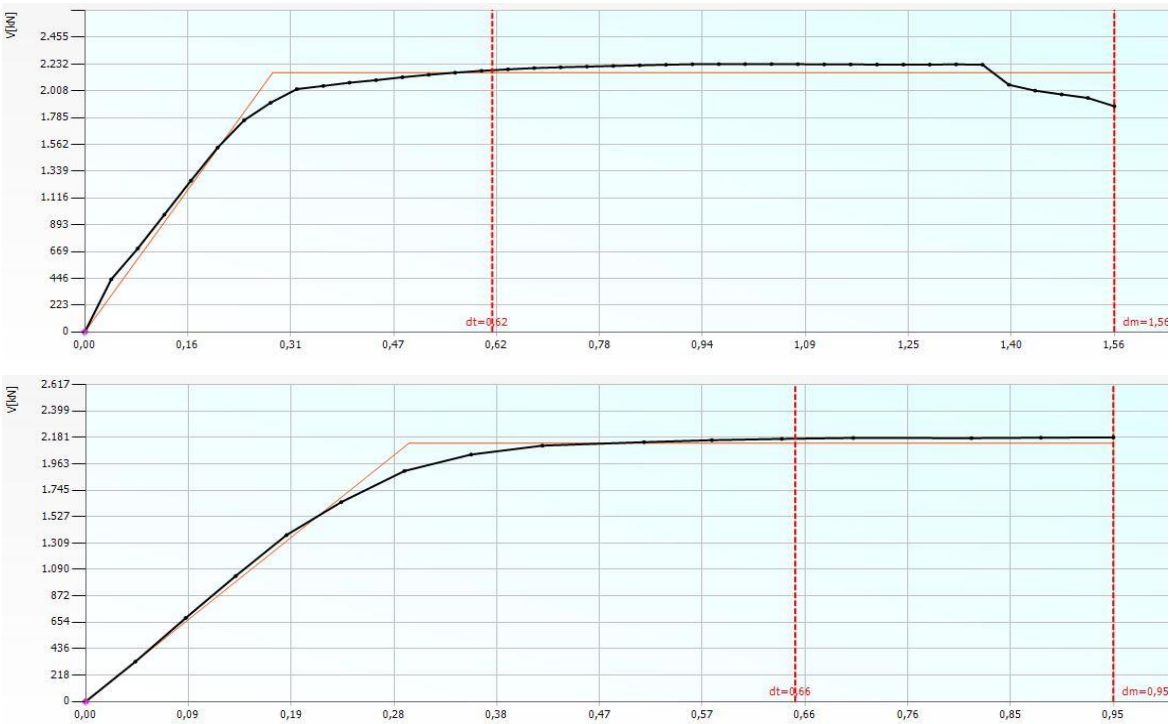

Fig. 19. Pushover curves of A Block_2-Story: a) *x*- direction; b) *y*- direction.

(a)

(b)

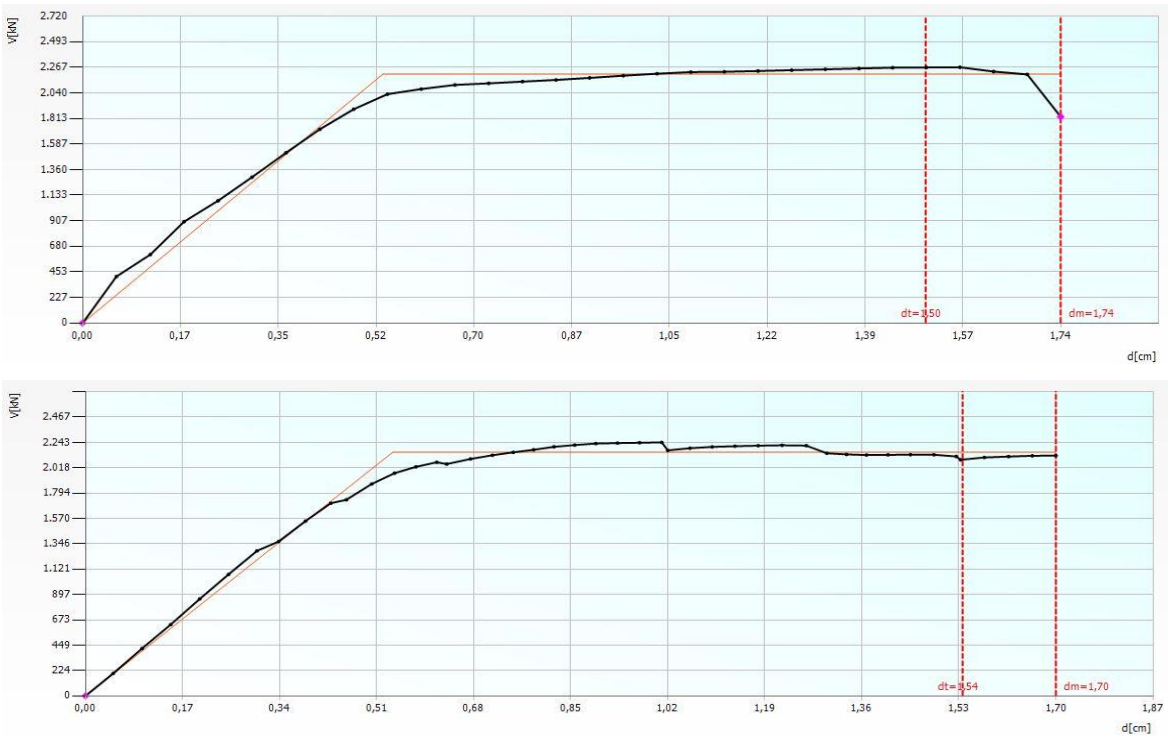

Fig. 20. Pushover curves of A Block_3-Story: a) *x*- direction; b) *y*- direction.

Table 5. PGA limit states for Block A.

Limit State	PGA (m/s²)			
	2-story		3-story	
	x-	*y*-	*x*-	*y*-
NC	2.713	1.866	1.767	1.629
SD	2.211	1.570	1.447	1.356
DL	1.072	1.055	0.849	0.927

5. Conclusions

The structures used as Emin Durbaku School blocks were examined on site. The masonry structures, which were built as pre-2000 schools, were originally designed as 2- floors and were subsequently increased to 3- floors. The current situation of the buildings was evaluated by considering the provisions of earthquake resistant design rules and Eurocode regulations (Eurocode 6 and 8) for masonry structures under seismic loads. The seismic capacities of the buildings were estimated by using a structural model which uses macro modelling approach for the load bearing masonry walls using TREMURI.

The type of soil that forms the foundation of the area is classified as "Dense gravel or medium dense sand and gravel" according to the laboratory test results that has an allowable load bearing capacity of 220 kPa (2.2 kg/cm^2). According to the EC 8, the soil class is considered in the seismic analysis as Type C. The study area is in one of the earthquake-prone zones of the country according to the Albanian probabilistic seismic hazard map.

The provisions of earthquake-resistant building design regulations on masonry structures and the suitability of the building are summarized in Table 2. Particularly in Block B, serious damage and non-conformities were found. Block A is generally more regular but due to the increase in the floor according to the seismic analysis results, the earthquake resistance capacity decreases up to 30%. The same applies to Block B. Both buildings suffered slight-moderate structural and non-structural damages due to the lack of sufficient stiffness during the November 26, 2019 Albania earthquake.

In conclusion, school buildings are buildings that need to be preserved in terms of their location, history and construction. School buildings to be used immediately after the earthquake should not be damaged. The buildings examined may be damaged due to the observed irregularities and inadequacies in a possible new earthquake. During the Durres earthquake of 6.4 magnitude on November 2019, serious damage was observed especially in Block B. However, this earthquake is smaller than design earthquake and it is classified as a medium intensity earthquake. Considering the actual status of these school buildings, urgent need needs to be put into action.

Data Availability

- Some or all data, models, or code that support the findings of this study are available from the corresponding author upon reasonable request.
- All data, models, and code generated or used during the study appear in the submitted article.

REFERENCES

Aliaj S, Kociu S, Muco B and Sulstarova E (2010). Seismicity, Seismotectonics and Seismic Hazard Assessment in Albania. The Academy of Sciences of Albania. ISBN: 978-99956-10-26. Albania.

Bilgin H (2015). Seismic performance evaluation of an existing school building in Turkey. *Challenge Journal of Structural Mechanics*. 1(4), 161-167.

Bilgin H, Frangu I (2017). Predicting the seismic performance of typical R/C healthcare facilities: emphasis on hospitals. *International Journal of Advanced Structural Engineering,* 9(3), 277-292.

Bilgin H, Huta E (2018). Earthquake performance assessment of low and mid-rise buildings: Emphasis on URM buildings in Albania. *Earthquakes and Structures*, 14(6), 599-614.

Bilgin H, Hysenlliu M (2020). Comparison of near and far-fault ground motion effects on low and mid-rise masonry buildings. *Journal of Building Engineering*, 30, 101248.

Chaulagain H, Rodrigues H, Spacone E, Varum H (2014). Design procedures of reinforced concrete framed buildings in Nepal and its impact on seismic safety. *Advances in Structural Engineering*, 17(10), 1419-1442.

Decanni L, D'Amore E, Goretti A, Langenbach R, Mollaioli F, Rasulo A (2004). Performance of masonry buildings during the 2002 Molise, Italy earthquake. *Earthquake Spectra*, S1, 191-220.

Estêvão J, Ferreira M, Morales-Esteban A, Martı´nez-A´ lvarez F, Fazendeiro Sa´ L, Requena-Garcı´a-Cruz MV (2018). Earthquake resilient schools in Algarve (Portugal) and Huelva (Spain). *16th European Conference on Earthquake Engineering,* Thessaloniki, Greece, 1–11.

Eurocode 6 (2005). Design of Masonry Structures - Part 1-1: General Rules for Buildings-Rules for Reinforced and Unreinforced Masonry. European Committee for Standardization, Brussels.

Eurocode-8 (2005) Design of structures for earthquake resistance. Part 3: Assessment and retrofitting of buildings. European Committee for Standardization, Brussels.

Irfanoglu A (2009). Performance of template school buildings during earthquakes in Turkey and Peru. *Journal of Performance of Construction Facilities*, 23, 5–14.

Katsuichiro G, Kiyota T, Pokhrel RM, Chiaro G, Katagiri T, Sharma K, Wilkinson S (2015). The 2015 Gorkha Nepal Earthquake: insights from earthquake damage survey. *Frontiers in Built Environment*, 1(8), 1-15.

KTP-9-78 (1978). Albanian Masonry Design Code. Tirana, Albania.

KTP-N2-89 (1989). Albanian Seismic Design Code. Tirana, Albania.

Lagomarsino S, Penna A, Galasco A, Cattari S (2013). TREMURI program: an equivalent frame model for the nonlinear seismic analysis of masonry buildings. *Engineering Structures,* 56, 1787-1799.

Lourenco P, Mendes N, Marques R (2009). Earthquake design and assessment of masonry structures: review and applications. *In book: Trends in Civil and Structural Engineering Computing, Chapter: 4.* Publisher: Saxe-Coburg Publications Editors: B.H.V. Topping, L.F. Costa Neves, R.C. Barros.

Magenes G, Penna A (2011). Seismic design and assessment of masonry buildings in Europe: recent research and code development issues. *9th Australasian Masonry Conference*, 583–603.

Mendes N, Lourenço PB (2010). Seismic assessment of masonry "Gaiolerio" buildings in Lisbon. *Journal of Earthquake Engineering*, 14(1), 80-101.

Mwafy A, Elkholy S (2016). Performance assessment and prioritization of mitigation approaches for pre-seismic code structures. *Advances in Structural Engineering*, 20(6), 917-939.

Nato Sfp – 983054 (2007-2010). Harmonization of Seismic Hazard Maps for The Western Balkan Countries (Bshap).

OECD Report (2004). Keeping schools safe in earthquakes. *Proceedings of the ad hoc experts' group meeting on earthquake safety in schools*, Organisation for Economic Co-operation and Development, Paris, 9-11 February.

TSDC (2018). Turkish Seismic Design Code. Ankara, Turkey.

Yılmaz S, Tama YS, Bilgin H (2013). Seismic performance evaluation of unreinforced masonry school buildings in Turkey. *Journal of Vibration and Control,* 19(16), 2421-2433.